Minh Anh Phan Nguyen

Creation and Manipulation of Quantum Emitters in Solid-State Materials

Thesis submitted in fulfilment of the requirements for the degree of Doctor of Philosophy

Faculty of Science
School of Mathematical and Physical Sciences
Primary Supervisor:
Prof. Igor Aharonovich
Co-supervisors:
Prof. Milos Toth
Dr. Sejeong Kim
Dr. Carlo Bradac
Dr. Mehran Kianinia

April 2021

Certificate of Original Authorship

I, Minh Anh Phan Nguyen, declare that this thesis, is submitted in fulfilment of the requirements for the award of Doctor of Philosophy, in the School of Mathematical and Physical Sciences at the University of Technology Sydney.

This thesis is wholly my own work unless otherwise referenced or acknowledged. In addition, I certify that all information sources and literature used are indiciated in the thesis.

This document has not been submitted for qualifications at any other academic institution.

This research is supported by the Astralian Government Research Training Program

Signature of Student:

Production Note:
Signature removed prior to publication.

Date: 31st of October 2020

Acknowledgements

I would firstly like to thank my primary supervisor Prof. Igor Aharonovich, for his sturdy and unwavering support during the length of my candidature. I've learnt many invaluable skills and experiences through your guidance and advice, and I am very fortunate and happy to call you my supervisor.

Additionally, to my brilliant co-supervisors, Prof. Milos Toth, Dr's Sejeong Kim, Mehran Kianinia, and Carlo Bradac, thank you all for your time and efforts throughout the years. Thanks also to Toan Trong Tran, Zaiquan Xu, and Sumin Choi for helping me find me feet in the group. I would not be the researcher I am today without your influence, and outstanding academic help.

Thank you to all the technical staff, Katie McBean, Geoff McCredie, and Mark Berkahn. The lab would be tatters were it not for your technical support and uncanny ability to just make things work.

To all my fellow colleagues within our lovely research group—Noah Mendelson, Johannes Froch, Blake Regan, Simon White, Chi Li, Connor Stewart, (Dr!) Hanh Ngoc My Duong, Yongliang Chen—I couldn't have asked for another group of people to share the lab space... and barbeque space with! There is never a dull moment hanging out with all of you. My cubicle space, Sharni Collins, Alisha Deo, Johnny Scott, and Matthew Cappadonna—spontaneity and snacks, always made for good times. To all my other fellow friends I've met around UTS—Level 5 and beyond (such as Jacqueline Loyola Echeverria)—thank you for all the pleasant memories. Your friendship made my time at UTS simply unforgettable. A special thanks specifically to Karen Duong, for being a great lunch buddy and routinely eating my watermelon candies. I wish you all the very best on your academic endeavours, we'll all make it eventually!

To my collaborators I've met abroad, Prof. Simeon Bogdanov and

Oksana Makarova, and Dr. Alexander Senichev. I thank you for your exceedingly kind hospitality during my short visit to Indiana! As well as all the collaborators who I've worked with on various publications; Niko Nikolay from Humboldt University of Berlin, and Hiroshi Abe from QST in Japan—thank you kindly for sharing in our awesome work.

I would like to express my gratitude towards UTS, for giving me the opportunity to study all throughout my tertiary education, from Bachelors all the way to Ph.D. My research as well as my conference travels were all supported by UTS. Additionally, this thesis was supported by an Australian Government Research Training Program. Finally, I would wholeheartedly like to thank my Family for their never-ending love and support during all the highs and lows during my candidature. This one is for you.

Contributing publications

Publications that contributed to this work are listed below. Equal-first authors are denoted by (†).

"Effects of microstructure and growth conditions on quantum emitters in gallium nitride", **M . Nguyen**, T. Zhu, M. Kianinia, F. Massabuau, I. Aharonovich, M. Toth, R. Oliver, C. Bradac. In: *APL Materials*, Vol. 7, 081106 (2019).

"Resonant excitation of quantum emitters in gallium nitride", M. Kianinia, C. Bradac, **M . Nguyen**†, T. Zhu†, M. Toth, R. Oliver, I. Aharonovich. In: *Optica Memorandum*, Vol. 5, Issue 8 (2018), pp. 932-933.

"Photodynamics and quantum efficiency of germanium vacancy color centres", **M . Nguyen**†, N. Nikolay†, C. Bradac, M. Kianinia, E. Ekimov, N. Mendelson, O. Benson, I. Aharonovich. In: *Advanced Photonics*, Vol. 1, Issue 6, 066002 (2019).

"Effects of high-energy electron irradiation on quantum emitters in hexagonal boron nitride", H.N.M. Duong†, **M . Nguyen**†, M. Kianinia, T. Oshima, H. Abe, K. Watanabe, T. Taniguchi, J. Edgar, I. Aharonovich, M. Toth. In: *ACS Applied Materials & Interfaces*, Vol. 10, Issue 29 (2018), pp. 24886-24891.

"Nanoassembly of quantum emitters in hexagonal boron nitride and gold nanopsheres", **M . Nguyen**†, S. Kim†, T.T. Tran, Z.Q. Xu, M. Kianinia, M. Toth, I. Aharonovich. In: Nanoscale, Vol. 10, Issue 5 (2018), pp. 2267-2274.

Publications not featured in this work containing research undertaken during the PhD program are listed below, with the contribution towards the work detailed.

"Revealing multiple classes of stable quantum emitters in hexagonal boron nitride with correlated optical and electron microscopy". F. Hayee, L. Yu, J.L. Zhang, C.J. Ciccarino, **M . Nguyen**, A.F. Marshall, I. Aharonovich, J. Vučković, P. Narang, T.F. Heinz, J.A. Dionne. In: *Nature Materials*, Vol. 19, Issue 5, (2020), pp. 534-539.

⇨ Performed fabrication and preparation of hBN material for the extensive characterisation performed with collaborators at Stanford University.

"Single photon emission from plasma treated 2D hexagonal boron nitride". Z.Q. Xu, C. Elbadawi, T.T Tran, M. Kianinia, X. Li, D. Liu, T.B. Hoffman, **M . Nguyen**, S. Kim, J.H. Edgar, X. Wu, L. Song, S. Ali, M. Ford, I. Aharonovich. In: *Nanoscale*, Vol. 10, Issue 17 (2018), pp. 7957-7965.

⇨ Performed material characterisation—specifically AFM—of hBN flakes used in the study.

"Facile assembly of hexagonal boron nitride nanoaprticles by cryogenic exfoliation". N.M.H. Duong, E. Glushkov, A. Chernev, V. Navikas, J. Comtet, **M . Nguyen**, M. Toth, A. Radenovic, T.T. Tran, I. Aharonovich. In: *Nanoletters*, Vol. 19, Issue 8, (2019), pp. 5417-5422.

⇨ Assisted in AFM characterisation of cryogenic exfoliated hBN flakes used in this study.

"Grain dependant growth of bright quantum emitters in hexagonal boron nitride". N. Mendelson, L. Morales, C. Li, R. Ritika, **M . Nguyen**, J. Loyola-Echeverria, S. Kim, S. Götzinger, M. Toth, I. Aharonovich. Just accepted in*: Advanced Optical Materials* (2020).

⇨ Performed wide-field imaging on hBN flakes grown on Ni substrate, with data used in publication.

"Observation of Fourier transform limited lines in hexagonal boron nitride". A. Dietrich, M. Bürk, E.E. Steiger, L. Antonuik, T.T. Tran, **M . Nguyen**, I. Aharonovich, F. Jelezko, A. Kubanek. In: *Physical Review B*, Vol. 98, Issue 8 (2018), pp. 2-6.

- ⇨ Synthesis of hBN material to be sent to collaborators at Ulm University to be used to collect data for this publication.

"All-optical control and super-resolution imaging of quantum emitters in layered materials". M. Kianina, C. Bradac, B. Sontheimer, F. Wang, T.T. Tran, **M . Nguyen**, S. Kim, Z.Q. Xu, D. Jin, A.W. Schell, C. Lobo, I. Aharonovich, M. Toth. In: *Nature Communications*, Vol. 9, Issue 1 (2018).

- ⇨ Provided assistance in construction of optical setup and performed optical measurements.

"Integrated on chip platform with quantum emitters in layered materials". S. Kim, H.N.M. Duong, **M . Nguyen**, T.J. Lu, M. Kianinia, N. Mendelson, A. Solntsev, C. Bradac, D. Englund, I. Aharonovich. In: *Advanced Optical Materials*. Vol. 7, Issue 23 (2019), pp. 1-6.

- ⇨ Assisted in perfoming optical measurements of hBN emitters on waveguides, along with AFM measurements of topography.

"Atomically thin boron nitride as an ideal spacer for metal-enhanced fluorescence". W. Gan, C. Tserkezis, Q. Cai, A. Falin, S. Mateti, **M . Nguyen**, I. Aharonovich, K. Watanabe, T. Tanaguchi, F. Huang, L. Song, L. Kong, Y. Chen, L.H. Li. In: *ACS Nano*, Vol. 13, Issue 10 (2019), pp. 12184-12191.

- ⇨ Assisted in optical measurements and characterisation of the hBN flakes with fluorescent molecules

Conference presentations

Oral Presentations

"Nanophotonic integration of hexagonal boron nitride"
Photonics West, 2D Photonic Materials and Devices II, San Francisco, USA (2019)

"Effects of microstructure and growth conditions on quantum emitters in gallium nitride"
ICONN, Nanomaterials, Brisbane, Australia (2020)

Poster presentations

"Nanoassembly of hexagonal boron nitride and gold nanospheres"
AIP Perth, Poster session, board 158, Perth, Australia (2018)

Table of contents

List of equations

List of figures

List of tables

Abbreviations

2D	Two-Dimensional
AFM	Atomic Force Microscope
APD	Avalanche Photodiode
BFP	Back-Focal Plane
CL	Cathodoluminescence
CVD	Chemical Vapour Deposition
CW	Continuous Wave
DFT	Density Function Theory
DW	Debye-Waller
ELOG	Epitaxially-Laterally Overgrown
EMCCD	Electron-Multiplied Charged Coupled Device
eV	Electron Volts
FDTD	Finite-Difference Time-Domain
FWHM	Full-Width Half-Maximum
FT	Fourier-Transform
GeV	Germanium Vacancy
GSD	Ground-State Depletion
HAADF	High-Angle Annular Dark-Field
hBN	Hexagonal Boron Nitride
HDD	High Density of Dislocations
HPHT	High-Pressure High-Temperature
HVPE	Hydride Vapour Phase Epitaxy
IPA	Isopropyl Alcohol
IRF	Instrument Response Function
LDD	Low Density of Dislocations
LDOS	Local Density of States

LSP	Localised Surface Plasmon
MBE	Molecular Beam Epitaxy
MOCVD	Metal-Organic Chemical Vapour Deposition
MOVPE	Metal-Organic Vapour Phase Epitaxy
NA	Numerical Aperture
ND	Nanodiamond
NV	Nitrogen Vacancy
N_VB_N	Anti-site Nitrogen Vacancy in hBN
PAMBE	Plasma-Assisted Molecular Beam Epitaxy
PSB	Phonon-Sideband
QE	Quantum Efficiency
SiC	Silicon Carbide
SMLM	Single-Molecule Localisation Microscopy
SNR	Signal-to-noise
SPE	Single-Photon Emitter
SPP	Surface Plasmon Polariton
SPS	Single-Photon Source
TCSPC	Time-Correlated Single Photon Counting
TD	Threading Dislocation
TEM	Transmission Electron Microscope
Ti:SAP	Titanium Sapphire
TMDC	Transition-Metal Dichalcogenides
UV	Ultra-violet
VLS	Vapour-Liquid-Solid
ZPL	Zero-Phonon Line

Abstract

Single-photon emitters are considered as a fundamental building block upon which many quantum-based applications are established. Of the many solid-state quantum emitters discovered, there exists three which garnered an increasing interest over the past few years; gallium nitride (GaN), germanium vacancy (GeV) colour centres in diamond, and quantum emitters in hexagonal boron nitride (hBN). Each of these solid-state emitter systems have unique advantages, making them intriguing candidates for quantum applications. However, there is still much to be understood regarding their optical properties and origin. Thus, the focus of this thesis is then established—to understand the origins of these solid-state sources through systematic studies of their growth and fabrication, followed by how they interact with the surrounding environment, and finally the modification of these interactions upon the addition of nanophotonic architectures.

Two separate studies were done on quantum emitters in GaN. First, the effects of microstructure and growth mechanics on the formation of emitters in GaN were investigated through multi-spectroscopic analysis in a systematic study of various material properties. No observable correlation was recorded, suggesting the origin of emitters was of an extrinsic nature, rather than intrinsic. The second study detailed the characterisation of the optical properties of GaN SPEs through resonant excitation, approaching Fourier-transform-limited linewidths of ~250 MHz—the narrowest reported for these emitters.

Next, a determination of the quantum efficiency (QE) of GeV colour centres in nanodiamond was performed by measuring and comparing radiative emission rates in a changing dielectric environment. Combined with Fourier-plane imaging of the resulting emission

patterns, a quantum efficiency of 22% was calculated from ensembles, several times higher than the SiV colour centre.

Finally, two separate studies on hBN SPEs were performed—the first study demonstrating the creation of emitters with high-energy electron irradiation. In this study, different hBN multilayer and monolayer flakes were irradiated with electrons in the megaelectronvolt regime, resulting in emitter creation within the flat regions of the hBN flakes, areas not seen in prior methods. The second study details the hybridisation of hBN emitters with plasmonic nanospheres, assembled via an atomic force microscope. An enhancement resulted in a maximum count rate of approximately 5.8 M counts/second, with the linear transition dipole exploited to maximise coupling to the nanospheres.

All of these studies serve to highlight the unique properties of their respective material systems, and further their development towards reliable integration with fundamental nanophotonic devices for applications in quantum information science.

Part I

Introduction

Chapter 1

Background and Context

1.1. Single-photon emitters for quantum applications

The move to using photons as carriers of information allows for extended capabilities, tied to the unique quantum nature of light which, when manipulated, can allow for quantum devices based on these photons to perform complex calculations at unparalleled speed, performing operations which classical computing devices are simply incapable of[1–4]. Additionally, unique applications such as ultra-secure quantum cryptography, can be realised owing to its quantum nature. From these properties, follow their utilisation as a fundamental unit of information—the Qubit. As an analogue to the classical bit, it is able to possess the quantum superposition of two states in a Boolean registry of $|0\rangle$ and $|1\rangle$ with any infinite combination of their vectorial components [5–7].

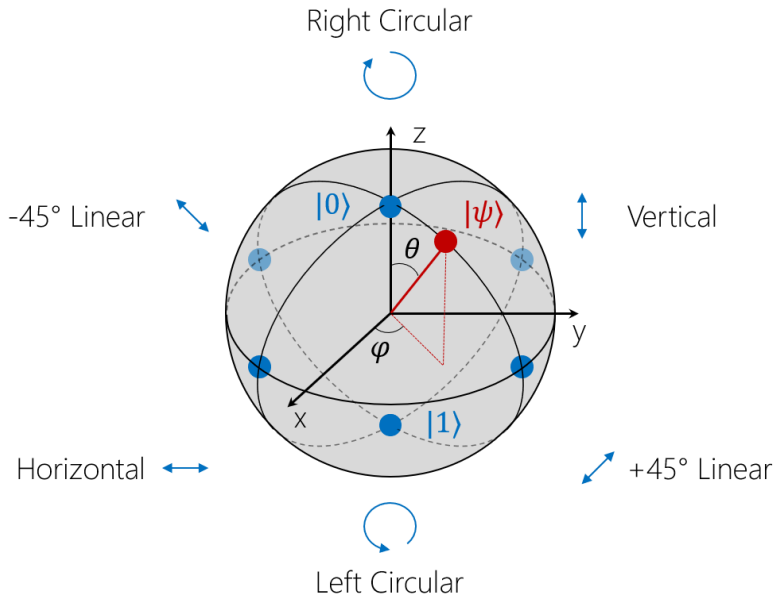

Figure 1.1. Fundamental operating principle of a qubit visualised through a combination of the Bloch and Poincare spheres.

Photons have been regarded as the perfect candidate for encoding this data, as their properties such as polarisation and phase can precisely superimposed. This concept is visualised in Figure 1.1, showing the way polarisation or phase can be assigned values for quantum computational operations, through a combination of the Bloch and Poincaré spheres—showing the geometrical representation of a two-level qubit and how it is translated to polarisation state, respectively[8].

What is then required is a method of producing streams of photons, at a frequency such that they can be manipulated at an individual level. Thus, single-photon sources (SPS) are at the forefront of research within the field of nanophotonics for a multitude of quantum computing schemes. Ultra-secure cryptography[9,10], quantum simulations[11], and precision metrology [12,13] are just a few possible implementations from which quantum emitters are foundational, following the new and upcoming paradigm shift towards nanoscale optics-based technology.

SPSs found specifically in the solid-state prove viable candidates when discussed in the context of quantum devices, combining the favourable optical properties of single atoms with the scalability and benefits of a solid-state system[14]. Such examples of currently studied solid-state systems include quantum dots (QDs)[15,16], colour centres in diamond[17–19], point defects in silicon carbide (SiC)[20,21], hexagonal boron nitride (hBN)[22,23], and gallium nitride (GaN)[24,25]. These sources additionally feature advantages over existing single-photon sources. For example, they are deterministic, meaning that they will emit light of their own only upon its direct excitation—an on-demand operation initiated by the user. This is contrary to heralded sources such as those based on spontaneous parametric down-conversion (SPDC) with their stochastic method of operation, and thus a comparatively lower efficiency[26]. Another notable property is that solid-state sources are already encapsulated within a solid material, making for integration with other nanophotonic architecture a comparatively far less complicated affair compared to trapped atoms or molecules[27,28]—with these sources requiring complex arrangements such as large cryogenic trapping setups in order to operate—making them impossible to be integrated on-chip. Despite these advantages, challenges still arise during two distinct phases towards the successful integration of a SPS for quantum applications; its creation and hybridisation.

Firstly, the creation of defect centres is largely non-trivial, with different materials requiring different methodologies – methodologies that are still misunderstood in materials such as hBN and GaN. Differing methods may result in different properties of SPSs such as photostability, brightness, and emission energy. The investigation into choosing the correct creation method to produce the most optimal characteristics can only be done through experimentation. In addition to producing usable SPSs, understanding the processes involved in defect creation allow the origins of the defect structure to be further

uncovered, a critical feature for their efficient operation, in-depth understanding, and the identification of suitable applications in each case.

The second challenge is then its hybridisation with additional nanophotonic/nanoelectronic architecture, which is a vital step required on the path to mature quantum devices. Integration allows for the manipulation and enhancement of coupled SPSs. Varying nanophotonic components afford control over different types of light-matter interactions such as waveguiding and tight-light confinement. A result of successful hybridisation can give rise to positive outcomes such as a reduced signal-to-noise ratio (SNR), and the creation of on-chip optical circuitry.

1.2. Aims and Motivations

This thesis focuses on quantum emitters in three different forms of solid-state materials; bulk, nano-, and two-dimensional (2D) crystals, specifically, the challenges and enigmas associated with their origins during synthesis and optical manipulation. GaN, GeV colour centres in diamond, and hBN are of current interest for quantum-based implementations as these systems are each considered novel and upcoming in their respective material form—that is, bulk, nano-, and 2D, respectively. Each of these three emitter systems have differing properties, which when exploited accordingly, highlight their potential depending on the application. However, with this newfound novelty, the need to uncover and further understand their underlying mechanisms and advance efforts towards their nanophotonic integration are of the utmost significance, should the intent be to utilise them for quantum-based applications—a need which this thesis aims to contribute to.

This thesis is split into two parts; Part I and Part II, spanning Chapters 1 through to 3 and 4 through to 8, respectively. The former aims to establish the theoretical groundwork associated within the field of quantum nanophotonics with single-photon emitters. The latter sections detail specific publications resulted from the Ph.D. candidature.

Chapter 2 presents an introductory outline of the concept of single-photons. The theoretical groundwork regarding the quantum definition of a photon is discussed, followed by the sources, which emit them at the single level. This chapter aims to define the fundamentals, which will be built upon in subsequent chapters.

Chapter 3 then continues upon the theory discussed in Chapter 2, directly translating that which was reviewed, into the experimental techniques and procedures performed. Optical microscopy, and its associated principal theory will be established, as well as the techniques of confocal microscopy and Fourier-plane imaging, following suit. Analytical techniques used to characterise single-photons are also explained—that is—time-correlated and time-tagged single-photon counting measurements, along with its necessary experimental apparatus.

Chapter 4 is the first of three experimental chapters in this thesis, presenting an overview of the work performed on gallium nitride (GaN) and its quantum emitters. The first part of this chapter focuses on understanding the origins of quantum emitters hosted within the material, probed *via* varying growth procedures. This project was performed in collaboration with Prof. Rachel Oliver and Dr. Tongtong Zhu, from the Department of Materials Science and Metallurgy, from the University of Cambridge. The second part of this chapter details the contributing work done on the resonant excitation of GaN quantum emitters, to further uncover its optical characteristics.

Chapter 5 entails an overview of the work done on group IV colour centres in diamond, specifically the germanium vacancy (GeV). Experiments were performed to probe its quantum efficiency, allowing for further understanding into its photophysical properties.

Chapter 6 contains the two separate works which revolve around quantum emitters in hexagonal boron nitride (hBN) and the nature behind their origins, as well as its potential for hybridisation and manipulation. The first part of this chapter concentrates on the creation of hBN defects using high-energy electron irradiation, and determining the various factors affecting its activation. The second part of the chapter then explores its hybridisation with plasmonic architectures, and the interactions involved between the two structures.

Chapter 7 provides a summary of contributions made to published works, many in collaboration with external research groups. These works were mainly performed on the study of hBN quantum emitters and are separated into subchapters based on their respective investigative goals. Specifically, inquiries into the origins of their defects, and their manipulation and hybridisation with additional nanophotonic structures.

Finally, a summary is provided in Chapter 8, providing a list of the achievements made in this thesis as well as promising future directions which arose as a consequence of this thesis.

Chapter 2

Single Photons

Having covered the potential of photons for use in quantum communications, this thesis then delves into the derivation, and core fundamental concepts behind the photon. Within this section, these concepts will be discussed within the context of the quantised electromagnetic field. Following this, the theory of photon statistics will also be covered, an important property of light fields, crucial to many measurements discussed throughout this thesis. In particular, an emphasis will be put on discussing these fundamental phenomena within the context of single-photon emission.

2.1. Introduction to the photon

The theory of the photon was quantised and eventually accepted through a culmination of derivations from Max Planck, Albert Einstein, and Gilbert N. Lewis, with the formula for blackbody radiation in 1900, the explanation of the photoelectric effect in 1905, and coinage of the term 'photon' as the smallest unit of radiant energy in 1926, respectively. Over the decades, the definition of the photon has changed slightly and is now understood today in modern physics as the smallest discrete amount of energy from a quantised electromagnetic field with an energy of E, defined by the equation:

$$\mathrm{E} = h\nu \qquad \text{Eq 2.1}$$

Where h is Planck's constant and ν is the photon's frequency[29]. In classical physics, the theory of light can be predominately explained in the framework of Maxwell's equations. However, upon discussion

of quantum phenomena such as photon antibunching and spontaneous emission, these equations can no longer sufficiently describe their behavior within a classical picture. As such, the quantisation of the electromagnetic field is necessary in order to provide a complete description of the photon, providing the mandatory groundwork for many other non-classical derivations.

2.1.1. Quantisation of the electromagnetic field

The quantisation of the electromagnetic field finds its origins with the classical description of a radiation field using Maxwell's equations. For simplicity, the derivation is considered in terms of a field confined to a one-dimensional cavity along the z-axis with perfectly conducting walls at $z = 0$ and $z = L$, vanishing at the boundaries, taking the form of a standing wave—a single-mode field[30].

The field is assumed to be polarised along the x-direction, giving $\boldsymbol{E}(r,t) = \boldsymbol{e}_x E_x(z,t)$, where $\boldsymbol{e}_x$ is a unit polarisation vector. The magnetic field in the cavity in the y-direction is expressed as $\boldsymbol{B}(r,t) = \boldsymbol{e}_y \boldsymbol{B}(z,t)$ [30–32]. Maxwell's equations can then be written as

$$\nabla \times \boldsymbol{H} = \frac{\partial \boldsymbol{B}}{\partial t} \qquad \text{Eq 2.2}$$

$$\nabla \cdot \boldsymbol{E} = \mu_0 \varepsilon_0 \frac{\partial \boldsymbol{E}}{\partial t} \qquad \text{Eq 2.3}$$

$$\nabla \cdot \boldsymbol{B} = 0 \qquad \text{Eq 2.4}$$

$$\nabla \cdot \boldsymbol{D} = 0 \qquad \text{Eq 2.5}$$

The single-mode field which satisfy Maxwell's equations and its boundary conditions can then be expressed as

$$\boldsymbol{E}_x(z,t) = \left(\frac{2\omega^2}{V\varepsilon_0}\right)^{1/2} q(t)\sin(kz) \qquad \text{Eq 2.6}$$

where ω is the frequency of the mode and k is the wave number related to the frequency according to $k = \omega/c$. Here, V is the effective volume of the cavity and $q(t)$ is the time-dependent factor with the dimension of length. The single-mode magnetic field similarly satisfying Maxwell's equations given the aforementioned boundary conditions are then

$$\boldsymbol{B}_y(z,t) = \left(\frac{\mu_0\varepsilon_0}{k}\right)\left(\frac{2\omega^2}{V\varepsilon_0}\right) p(t)\cos(kz) \qquad \text{Eq 2.7}$$

Here, $p(t) = \dot{q}(t)$, and represents the canonical momentum for a 'particle' of unit mass. Given the classical field energy, or Hamiltonian H, of the single-mode field is expressed as;

$$H = \frac{1}{2}\int dV\left[\varepsilon_0 \boldsymbol{E}^2(\boldsymbol{r},t) + \frac{1}{\mu_0}\boldsymbol{B}^2(\boldsymbol{r},t)\right] \qquad \text{Eq 2.8}$$
$$\frac{1}{2}\int dV\left[\varepsilon_0 \boldsymbol{E}_x^2(\boldsymbol{z},t) + \frac{1}{\mu_0}\boldsymbol{B}_y^2(z,t)\right]$$

and can then be rearranged in terms of Equations 2.5 and 2.6 such that

$$H = \frac{1}{2}(p^2 + \omega^2 q^2) \qquad \text{Eq 2.9}$$

It can then be seen that the single-mode field is formally equivalent to a harmonic oscillator of unit mass, where electric and magnetic fields play the roles of canonical position and momentum, with some scaling factors in addition[30–32]. Having identified the canonical operators q and p for the classical system, using the correspondence rule they are replaced with their quantum operator equivalents $\hat{q}$ and $\hat{p}$, such that these operators satisfy the canonical commutation relation;

$$[\hat{q},\hat{p}] = i\hbar \qquad \text{Eq 2.10}$$

This transforms the electric and magnetic fields of the single-mode field, respectively, to

$$\widehat{\boldsymbol{E}}_x(z,t) = \left(\frac{2\omega^2}{V\varepsilon_0}\right)^{1/2} \hat{q}(t)\sin(kz) \quad \text{Eq 2.11}$$

and

$$\widehat{\boldsymbol{E}}_x(z,t) = \left(\frac{\mu_0\varepsilon_0}{k}\right)\left(\frac{2\omega^2}{V\varepsilon_0}\right)\hat{p}(t)\cos(kz) \quad \text{Eq 2.12}$$

Respectively, the Hamiltonian becomes

$$\widehat{\boldsymbol{H}} = \frac{1}{2}(\hat{p}^2 + \omega^2\hat{q}^2) \quad \text{Eq 2.13}$$

As the canonical operators $\hat{p}$ and $\hat{q}$ are Hermitian, corresponding to observable quantities, introduced are then the non-Hermitian (and therefore non-observable) ladder operators ($\hat{a}$) and its Hermitian conjugate ($\hat{a}^\dagger$), in terms of position and momentum.

$$\hat{a} = \frac{1}{(2m\hbar\omega)^{1/2}}(\omega\hat{q} + i\hat{p}) \quad \text{Eq 2.14}$$

$$\hat{a}^\dagger = \frac{1}{(2m\hbar\omega)^{1/2}}(\omega\hat{q} - i\hat{p}) \quad \text{Eq 2.15}$$

These terms are also known as the annihilation ($\hat{a}$) and creation ($\hat{a}^\dagger$) operators and will be further expanded later in Chapter 2.1.2. The electric field and magnetic field operators are then transformed to;

$$\widehat{\boldsymbol{E}}_x(z,t) = \mathcal{E}_0\left(\hat{a} + \hat{a}^\dagger\right)\sin(kz) \quad \text{Eq 2.16}$$

$$\widehat{\boldsymbol{B}}_y(z,t) = \mathcal{B}_0\frac{1}{i}\left(\hat{a} + \hat{a}^\dagger\right)\cos(kz) \quad \text{Eq 2.17}$$

Where $\mathcal{E}_0 = (\hbar\omega/\varepsilon_0 V)^{1/2}$ and $\mathcal{B}_0 = (\mu_0/k)(\varepsilon_0\hbar\omega^3/V)^{1/2}$ represent the electric and magnetic fields, respectively, during the instance of a single photon. This term is used rather loosely as the average of these fields for a definite number of photons is zero, and is thus not entirely correct. Nevertheless, they provide a convenient measure of the fluctuations of the quantised field[11].

The ladder operators satisfy the commutation $[\hat{a}^{\dagger}\hat{a}] = a\hat{a}^{\dagger} - \hat{a}^{\dagger}\hat{a} = 1$, thus resulting in the quantum Hamiltonian taking the form

$$\widehat{\boldsymbol{H}} \quad = \quad \hbar\omega\left(\hat{a}^{\dagger}\hat{a} + \frac{1}{2}\right) \qquad \text{Eq 2.18}$$

It is clear based on this representation, that the Hamiltonian of the quantised fields is in the form of a quantum harmonic oscillator, allowing all its known results to apply within a quantum picture[30,33].

2.1.2. Photon number states

The concept of the number state representation allows us to quantify light fields by the number of energy quanta excited, expressed in terms of states labelled by n. These are also known as Fock states, and are usually expressed in Dirac notation as $|n\rangle$. Having defined the Hamiltonian of a quantised single-mode field, its solution is then expanded *via* Fock states and the ladder operators $(\hat{a})$ and $(\hat{a}^{\dagger})$.

As recalled from equation 2.13 and 2.14, the ladder operators $\hat{a}$ and $\hat{a}^{\dagger}$ were introduced as quantum mechanical operators. In the context of a quantum harmonic oscillator, the raising operator $(\hat{a}^{\dagger})$ and lowering operator $(\hat{a})$ can be interpreted as adding or subtracting a quanta of energy to the oscillator system; frequently termed the creation and annihilation operators repectively. Applying $\hat{a}^{\dagger}$ on an n-fold excited state $|n\rangle$ raises it to $n+1$ fold excited state $|n+1\rangle$,

$$\hat{a}^{\dagger}\,|n\rangle \quad = \quad (n+1)^{1/2}|n+1\rangle \qquad \text{Eq 2.19}$$

while applying $\hat{a}$ lowers the state to $|n-1\rangle$;

$$\hat{a}\,|n\rangle \quad = \quad n^{1/2}|n-1\rangle \qquad \text{Eq 2.20}$$

Additionally, the ground state $|0\rangle$ corresponds to the state in which no quanta are excited, implying that the number states can be built up from the ground state by repeated application of the creation operator:

$$|n\rangle = \frac{1}{(n!)^{1/2}}\left(\hat{a}^{\dagger}\right)^{n}|0\rangle \qquad \text{Eq 2.21}$$

As the energies of the harmonic oscillator are equidistant, the state $|n\rangle$ can also be interpreted as a single state with n photons of energy $\hbar\omega$. This is referred to as a photon number state, or Fock state. Such a state is comprised of the aforementioned creation and annihilation operators. Expanding on this, the number operator is introduced, which defines the total quanta of energy within the number state $|n\rangle$,

$$\hat{n} = a^{\dagger}a, \qquad \text{Eq 2.22}$$

from which it can be further deduced that

$$\hat{n}|n\rangle = n|n\rangle \qquad \text{Eq 2.23}$$

Fock states, in this respect, can be interpreted as the eigenstates of the number operator, which return a discrete number of photons n when acting on a state $|n\rangle$ within the corresponding mode.[33] The concept of the Fock state is a significant understanding, which greatly simplifies the derivations of complex quantum phenomena such as photon antibunching, discussed later in Chapter 2.2.2 and 3.2.3.

2.2. Photon statistics

Having described how light emitted from a source can be characterised in terms of individual quanta or photons, it is then understood that these quanta can be categorised temporally through the analysis of their arrival times at an arbitrary detector, along with their fluctuations through time. Generally considered, light sources can be classified into three primary distributions; chaotic or thermal light, coherent light, and antibunched light. In order to better understand the features of each source, it is helpful to compare the statistical properties of light emitted from different sources.

2.2.1. Statistical classification of light

Thermal Light

Conventional macroscopic lamps, such as incandescent bulbs, emit thermal or 'chaotic' light. Its electric field is a superposition of many incoherent waves, all of which are assumed to share the same formal time-dependence with a random phase delay. A thermal source is known to possess strong fluctuations of its electric field, where statistically the number of photons in a given mode follows a Bose-Einstein distribution of black-body radiation

$$P_n = \frac{(\bar{n})^n}{(1+\bar{n})^{1+n}} \qquad \text{Eq 2.24}$$

where $(\bar{n})$ is the average number of photons in the mode.

Coherent Light

The classical picture of laser light is defined as a wave with constant phase and frequency. Classically speaking, light emitted within this classification do not possess any fluctuations in its electric field. In the quantum representation of such a wave they are sometimes known as quasi-classical states when described in terms of the previously

discussed Fock states. The number of photons in a coherent state is a variable, which fluctuates according to a Poissonian distribution. The probability of finding n photons in the mode is given by

$$P_n = \frac{\bar{n}^n}{n!} e^{-\bar{n}} \quad \text{Eq 2.25}$$

Squeezed Light

A squeezed light source is one which delivers a regular stream of multiple photons at uniform time intervals, with fluctuations in the number of photons emitted by a squeezed source weaker than those of a coherent state, following as what is coined as a sub-Poissonian distribution.

$$P_n = \begin{cases} 0, & \text{for } n \neq \bar{n} \\ 1, & \text{for } n = n \end{cases} \quad \text{Eq 2.26}$$

Unlike thermal or coherent light, squeezed light does not follow any classical statistical distribution, and thus cannot be derived by any classical interpretation. Single photon sources produce squeezed light where each photon is emitted at intervals defined by the excited state lifetime of the source, in what is referred to as antibunched emission[33].

2.2.2. Second-order correlation function

The second-order correlation function describes the temporal fluctuations of intensity in an electric field as a function of time, and can provide a quantitative way of determining the class of emission measured. In the case of a photon stream, emitting a photon at a certain time $t + \tau$ (where t is the time of the previously emitted photon), the function is expressed as

$$g^{(2)}(\tau) = \frac{\langle \varepsilon^*(t)\varepsilon^*(t+\tau)\varepsilon(t+\tau)\varepsilon(t)\rangle}{\langle \varepsilon^*(t)\varepsilon(t)\rangle\langle \varepsilon^*(t+\tau)\varepsilon(t+\tau)\rangle} = \frac{\langle I(t)I(t+\tau)\rangle}{\langle I(t)\rangle\langle I(t+\tau)\rangle}$$

where $\varepsilon(t)$ and $I(t)$ are the time-averaged electric field and intensity of the light stream at time t. With the assumption that the source is emitting at a constant average intensity, the expression for $g^{(2)}(\tau)$ is then given as

$$g^{(2)}(\tau) = \frac{\langle I(t)I(t+\tau)\rangle}{\langle I(t)\rangle^2} \quad \text{Eq 2.27}$$

Within a quantum mechanical setting, it is useful to frame the aforementioned operations in terms of photon number states, and the corresponding creation and annihilation operators, where $\hat{n} = \hat{a}^\dagger\hat{a}$. This function can then be rewritten in terms of these quantum operators, yielding

$$\begin{aligned} g^{(2)}(\tau) &= \frac{\langle \hat{a}^\dagger(t)\hat{a}^\dagger(t+\tau)\hat{a}(t+\tau)\hat{a}(t)\rangle}{\langle \hat{a}^\dagger(t)\hat{a}(t)\rangle^2} \\ &= \frac{\langle \hat{n}(\hat{n}-1)\rangle}{\langle \hat{n}\rangle^2} \end{aligned} \quad \text{Eq 2.28}$$

This equation can then be evaluated for arbitrary inputs, where the input is the photon number state of a value n

$$g^{(2)}(\tau) = \frac{n(n-1)}{n^2} \quad \text{Eq 2.29}$$

The final equation takes Equation 2.28 and is evaluated for arbitrary inputs. Based on this equation, the same classifications mentioned earlier can be equated to values based on the second-order correlation function at a time difference of $\tau = 0$. The table below shows the possible solutions to the second-order correlation function $g^{(2)}(\tau)$ and their corresponding light source.

Light Source	Solution at zero-delay time
Chaotic/Thermal light	$g^{(2)}(0) > 1$
Coherent light	$g^{(2)}(0) = 1$
Squeezed light	$g^{(2)}(0) = 1 - \frac{1}{n}$

Table 2.1. Second-order correlation derivations for the three different classes of light

Practically, the $g^{(2)}(\tau)$ value of a light source can be interpreted as the probability to detect a second photon within the span of the given delay time. In the case of the aforementioned conditions, having a $g^{(2)}(\tau) > 1$ means an increased probability of detecting a photon directly after the first detection event been registered, which is referred to as bunching. $g^{(2)}(\tau) = 0$ means that the probability to detect a second photon is independent of the time difference to prior detection events. For $g^{(2)}(\tau) < 1$, the probability of detecting a second photon is even less than in the case of coherent light and is referred to as antibunching[33]. The methods by which these correlations are performed experimentally will be discussed further in Chapter 3.2.3.

2.3. Quantum emission from single-photon sources

Solid-state sources, lay the basis for various technologies such as light-emitting diodes, lasers, and telecommunications. Such solid-state sources are capable of producing non-classical, antibunched emission – a coherent stream of individual photons at temporally separated intervals, through the hosting of optically active defect centres. These

quantum emitters find themselves at the forefront of research and development into usable quantum-based devices and applications. Such applications require scalable platforms for the integration of SPSs—as such, solid-state materials provide an effective solution to the problem of integration and application combining the optical properties of atoms with the convenience and scalability of a solid-state host system. Subsequently, the last decade has seen numerous advances in understanding the photophysical properties of SPSs, their efficient and controlled creation, and their integration with nanophotonic constituents.

2.3.1. Photophysics of single-photon sources

Single-photon emitters (SPEs) hosted within solid-state materials predominantly consist of either an intrinsic defect or a foreign substitutional atom embedded within the crystalline matrix of a host material. Upon the rearrangement of the lattice to facilitate this change, what follows is also a modification of its electronic structure—an introduction of narrow energy levels within the bandgap of the host crystal. Upon excitation of the defect by sub-bandgap energy, the system can be promoted to the excited state where it will dwell for some length of time unique to that system. The electron will then undergo a relaxation from its excited state, emitting light during the process and producing a characteristic, sharp zero-phonon line (ZPL) energy, which may be broadened due to transitions to upper-electronic phonon ground states from an off-resonant excitation process. Often times, a phonon-side band (PSB) will also accompany the ZPL during emission, as exchanging of momentum occurs between the defect transitions and the lattice[34]. The entire transition process between the ground and excited state can be described using a Franck-Condon diagram, shown below in Figure 2.1.

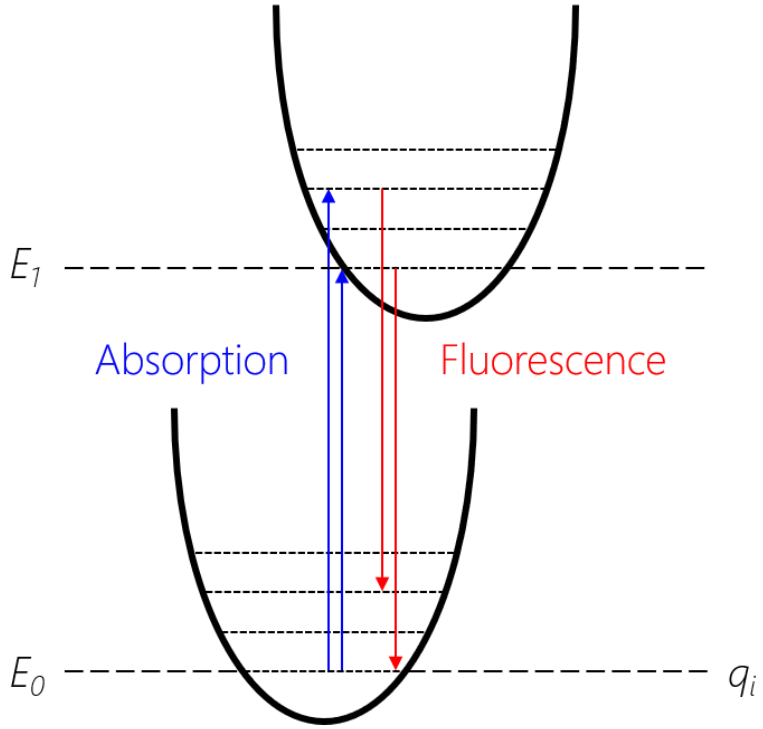

Figure 2.1. Franck-Condon diagram showing the transition process between ground and excited states. E_0 and E_1 are the ground and excited states respectively, and q_i is the normal mode of the lattice.

The energy diagram shows the electronic transition with phonon coupling along the configurational coordinate q_i—the normal mode of the lattice. The transition probability is determined by the overlap of the phonon wavefunctions of the energy levels[34]. The fluorescence emitted during this transition is the primary signal that is collected and manipulated. Most solid-state SPS will follow this general two-level system, however, it will be shown later that other energy levels can also be introduced depending on the defect being probed.

As mentioned, this thesis will have an emphasis on three specific material systems and their quantum emitters—GaN, GeV colour centres in diamond, and hBN. Each of these material systems are similar in that they can host optically active defect centres, displaying high single-photon purity. Additionally, there are also advantages bespoke to the specific material system as well. Table 2.2 below shows a brief summary of important properties from each material system,

along with other existing material systems and the optical properties of their emitter for comparison.

Emitter System	ZPL Range (nm)	Excited state lifetime (ns)	Average Count rate (counts/s)	Unique property
Defects in GaN	600–750 [25] 1085–1340 [35]	Vis: ~1.5–3 [36] Tel: ~0.7–0.8 [35]	4.27×10^5 [36]	Versatile growth
GeV in Diamond	GeV: ~604 [18]	Bulk: ~1.4–5.5 [18] ND: ~5–25 [37]	Bulk: 1.7×10^5 [18] ND: 7.14×10^5 [37]	Homogenous optical properties
Defects in Diamond	NV^-: 637 SiV: ~740 [38]	NV: ~12–22 SiV: ~1 [38]	NV: 1×10^6 SiV: 3×10^6 [38]	Spin initialisation
Defects in hBN	570–780 [39]	~3–6 [40]	$0.1–2.4 \times 10^6$ [39]	2D material, linear polarisation
Defects in Silicon Carbide	400–1800 [41]	~1–4 [42]	$\sim 2 \times 10^6$ [42]	Easily integrated
Quantum Dots	200–1600 [43]	Arsenide: ~1 [43] Nitride: ~0.3 [43]	Arsenide: N/A [43] Nitride: 1×10^7 [43]	Consistent physical properties
Rare Earth Ions in YAG	Atomic line [44]	~19 [45]	$\sim 6 \times 10^4$ [45]	High photon purity

Table 2.2. Brief summary of emitter systems. The systems in **bold** are covered in this thesis.

As they are hosted within solid-state materials, there exists the advantages of such as briefly explained in Chapter 1.2. However, there are also significant challenges to address, largely stemming from the solid-state host. Typically, the complex mesoscopic environment of solid-state mediums adds to the complexity to the system bath, through phenomena such as trapped charges introduced with extrinsic atomic impurities. These manifest in the form of dephasing resulting in linewidth broadening, and inhomogeneous variability between photons from emitter to emitter[14]. Ultimately, this gives rise to

degradation of photon indistinguishability—a necessary property required for applications of quantum cryptography. The following chapters will then go into details behind three previously mentioned single photon sources, detailing their characteristics as well as shortcomings.

2.3.2. Quantum emitters in Gallium Nitride

III-nitride materials have been widely used within the solid-state industry, its utilisation spanning across many technologies including lighting, high-frequency high-power electronics, and laser science.[24,46–48] Gallium Nitride (GaN) is one such nitride which possesses a number of favourable physical characteristics which warrant it advantageous for a variety of solid-state applications—biocompatability[49], non-linear optical susceptibility[50], and spontaneous piezoelectric polarisation[51,52] being examples of its unique properties. It stands as one of the most widely studied and established III-nitride materials, with extensive application in white and blue-light emitting diodes[53,54]. GaN can exist in either a hexagonal (wurtzite) or cubic (zinc-blende) structure[55]. The wurtzite form consists of alternating layers of close-packed (0001) Ga metal atoms and nitrogen atoms, in an AB stacking configuration [Figure 2.2 (a)]. The change in the sequence during growth can produce defects within the crystal, which are also known as stacking faults, a concept which will be explained later in this chapter.

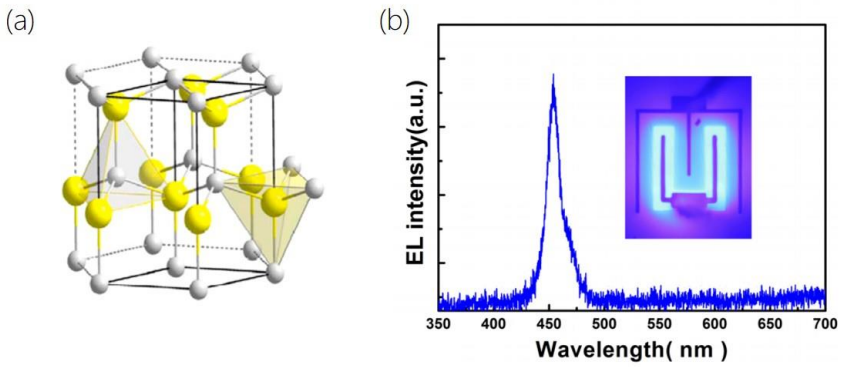

Figure 2.2 Introduction to GaN. (a) Schematic of a unit cell of Gallium Nitride. (b) Emission from a GaN SPE via electrical excitation. Reproduced from Ref.[53,54].

Synthesis of GaN

Due to its widespread research, it has appropriately seen many variations of documented synthesis procedures, making for a strongly established database of techniques synthesising various forms of GaN from nanorods and nanowires to more unconventional structures such as the amusingly-named chestnuts, and durians[53,56–58]. Growth procedures can be categorised into two types, catalyst-assisted and catalyst free growth. The former method typically occurs *via* transitions introducing reactants and products through a vapour-liquid-solid (VLS) process. It involves the introduction of vapour-phase reactants into a catalytic liquid metal to form a supersaturated solution, and then finally a crystalline deposit of GaN[59]. Metal-organic vapour-phase epitaxy (MOVPE) and metal-organic chemical vapour deposition (MOCVD) using metal catalysts have been reported as methods for the growth of nanowires and nanorods, respectively[60,61]. There are also many instances of the latter approach being used, with examples in Metal-organic vapour-phase epitaxy (MOVPE), hydride VPE (HVPE), and plasma-assisted molecular-beam epitaxy (PAMBE) being used for growth of similar structures[62–64].

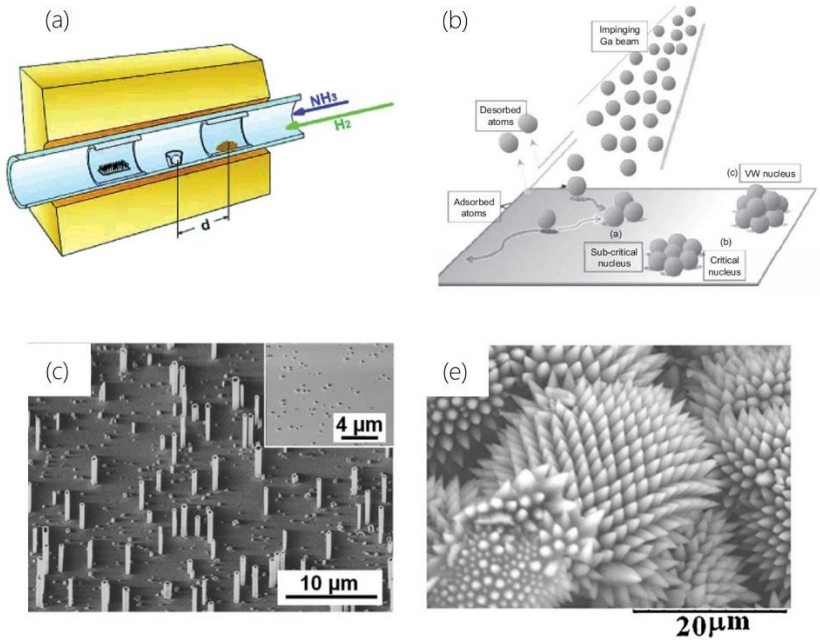

Figure 2.3. Various growth of GaN showing the forms possible. (a) Schematic diagram of an MOCVD chamber used for synthesis of GaN. (b) Schematic illustration showing the MBE process used for GaN growth. (c) Upright standing nanowires of GaN. (d) 'Durian-shaped' GaN structures, showing the more exotic forms possible. Reproduced from Ref.[57,62–64]

Epitaxial methods such as those mentioned, result in the deposition of GaN as formed between the reaction of a Ga precursor with ammonia on a foreign substrate such as sapphire, GaAs, and SiC—the main differences between them being the method by which the reactants are introduced[65–67]. In addition to the deposition of GaN onto the target substrate, the concept of doping can also be achieved through this method with additional foreign impurities—such as Mg for example—introduced in order to modify characteristics such as free carrier density, subsequently modifying conductivity[68,69]. Catalytic growth is evidenced to more efficiently promote NW growth, but is known to incorporate much more in the way of extrinsic contaminants as well as defects within its structure. Catalyst-free growth is designed to reduce these effects, showing to be the superior growth method for structures such as nanowires[70]. The synthesis of GaN itself is considered a desirable property, as the material is capable of being

grown onto any substrate of choice. Low-refractive index substrates—necessary for mature nanophotonics—make for ideal substrates in integrated quantum circuitry and are indeed viable growth substrates for GaN, unlike other wide bandgap crystals such as diamond, or SiC. However, it should be noted that GaN—along with all other III-V semiconductors—suffer from material defects as a consequence of its bottom-up growth procedures. Faults in the crystalline structure during the growth manifest due to the lattice mismatch between the growth substrate and the grown material. In the case of GaN, these threading dislocations are known to cause material degradation over time[58,71,72]. However, they have also been hypothesised to be the source of quantum emission from GaN[25], a phenomena which will be further explained in the following chapter as well as its dedicated study in Chapter 4.1.

Quantum characteristics from GaN emitters

Recently, GaN has been the subject of interest following the discovery of quantum emission hosted from defects within the lattice. GaN quantum emitters can be characterised by sharp, asymmetric ZPL lines spanning all throughout the visible region towards IR wavelengths. The ZPLs are shown to have differing energy and linewidths from emitter to emitter due to many possible variations at each defect—this will be further expanded upon in Chapter 4.1.6. The emission is both bright, and stable, with reports of emitters reaching count rates of 10^5 counts/s at saturation[25,35,36].

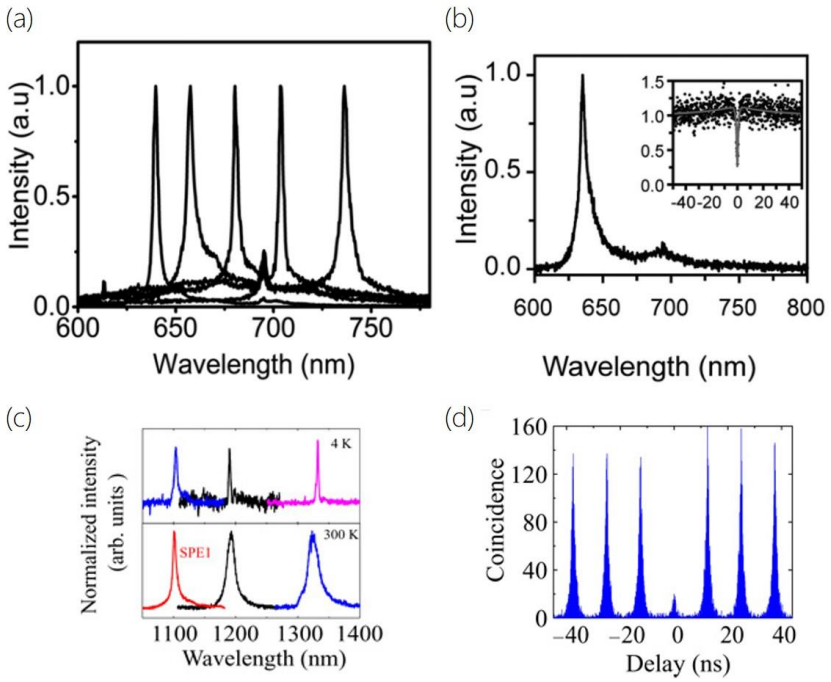

Figure 2.4. Optical characteristics of GaN revealing quantum behaviour. (a) A range of (5) ZPLs measured from GaN. (b) A single GaN quantum emitter showing a ZPL at ~640 nm. Inset shows the corresponding autocorrelation function, with $g^{(2)}(0) < 0.5$, indicating quantum emission. (c) Cryogenic measurements of GaN emitters performed at 4 K and 300 K from top and bottom plots, respectively. (d) Pulsed autocorrelation measurement showing quantum emission. (a) and (b) are reproduced from ref. and (c) and (d) are reproduced from Refs.[25,35]

As mentioned earlier, the source of this emission is still unknown, with hypotheses of its origin stemming from threading dislocations and stacking faults present in the crystal as a result of lattice direction mismatch between the GaN crystal and growth substrate[16,71]. Studies have proposed that characterised SPEs are localised close to extended defects formed around a cubic inclusion (Figure 2.5). These localised cubic inclusions are suggested to introduce a quantum well, for the conduction band electron due to the narrower bandgap of cubic GaN relative to wurtzite GaN. The spontaneously polarised wurtzite matrix surrounds the cubic inclusion producing an electronic state with a localised electric field [73,74]. Conversely, there have also been

studies which refute this argument—the details of which, as mentioned, to be discussed later in Chapter 4.

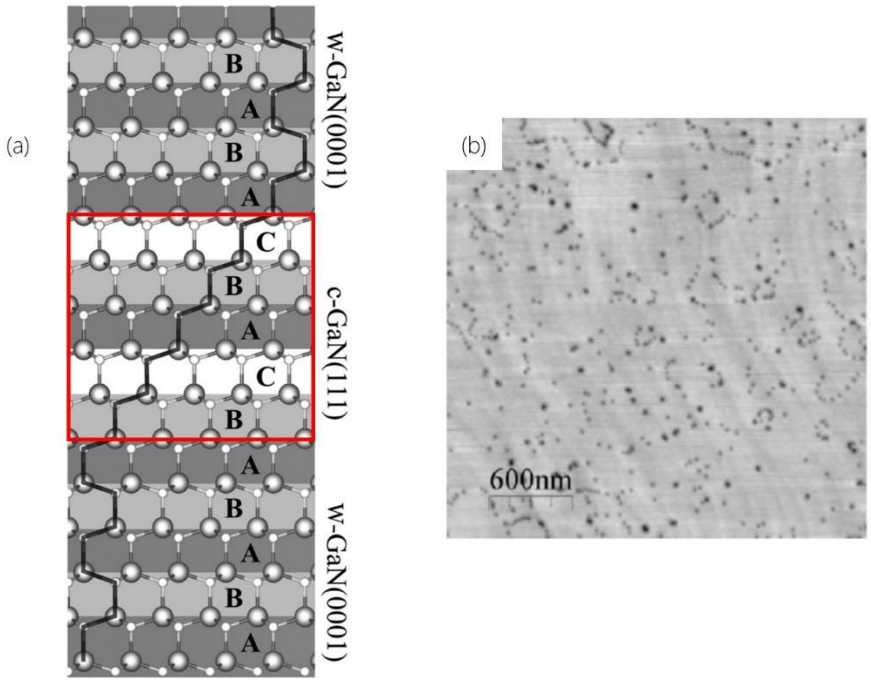

Figure 2.5. Stalking faults and dislocations in GaN. (a) Schematic diagram of a cubic inclusion found in GaN. The red box indicates the cubic phase occurring between wurtzite phases. (b) AFM image of the surface of a GaN sample, showing threading dislocations terminating at the surface. Reproduced from Ref.[25]

2.3.3. Germanium Vacancy Colour Centres in Diamond

Diamond is a wide bandgap semiconductor, widely known for its extremely durable physical properties; a high melting point, chemical inertness, mechanical strength (Young's Modulus), and biocompatibility being just a few examples of its beneficial qualities[75–77]. Its wide 6 eV bandgap also allows the crystal to play host to over 500 possible optical centres[78], with PL ranging from the deep ultra violet (UV) into the infrared regions—its emission source lying within the numerous crystallographic impurities and defects arranged within the lattice[79]. Group IV defects in diamond specifically, have emerged as strong candidates for use in future quantum information processing (QIP) architectures based on numerous studies into their properties

[80]. These colour centres can be characterised by their specific defect structure identified as group D_{3d} symmetry [Figure 2.6 (a)], which involves a group IV element (the substitutional atom, labelled 'M') positioned between its two nearest-neighbouring missing carbon atoms (the vacancy, labelled 'V') along the ⟨111⟩ direction in the diamond lattice[81].

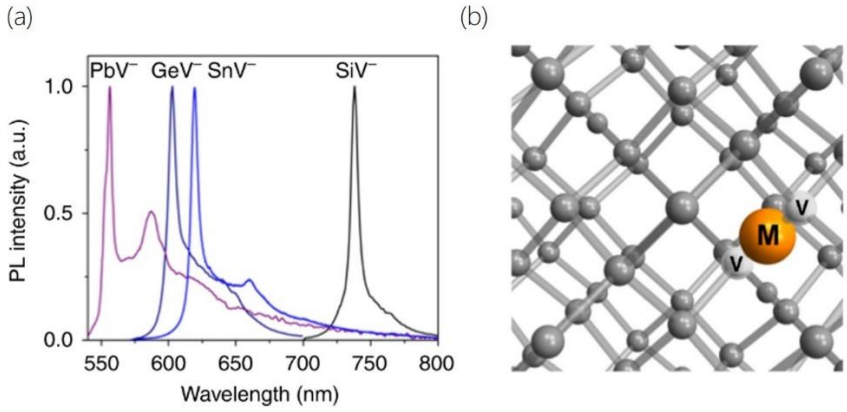

Figure 2.6. Group IV colour centres in diamond. (a) Characteristic ZPL from the four currently studied Group IV centres. From left to right: PbV, GeV, SnV, and SiV. (b) Schematic illustration of a Group IV vacancy. The orange ball labelled 'M' represents the metal atom, and the grey balls labelled 'V' represent the neighbouring vacancies. Reproduced from Ref.[80]

Silicon vacancy (SiV) centres in diamond were observed as the first instance of the Group IV colour centres showing the aforementioned D_{3d} symmetry configuration[82]. A past study of SiV defects grown via chemical vapour deposition (CVD), allowed for the isolation of the colour centre down to the single-defect level[83]. This allowed for further, more accurate studies into the photophysical properties, electronic structure, and spin and coherence values of the defect centre[19,84–86]. Generally, single SiV are shown to have stable, bright photoemission (exceeding 4 M counts/s at saturation), which was remarkably photostable and possessing a lifetime-broadened linewidth. This was understood to be due to its aforementioned inversion symmetry, which protects the optical transitions from local

electric field fluctutations[81]. Despite such advantages, the shortcomings of the SiV, namely its intrinsically low quantum efficiency and short spin coherence times, prompted studies into other Group IV defects to find suitable hosts with QIP applications in mind[85].

GeV synthesis and characterisation

In 2015, the Germanium-Vacancy (GeV) was identified with optical signatures similar to that of SiV[18]. GeV colour centres can be incorporated into various forms of diamond through many different bottom-up growth techniques. Well-known diamond synthesis techniques include microwave-plasma assisted CVD and high-pressure high-temperature (HPHT) synthesis, the former producing single-crystalline diamond films and the latter NDs[87,88]. Incorporation of GeV into this form of diamond can be achieved through the introduction of dopants, whether it be in gaseous form or via organic compounds containing Germanium[89].

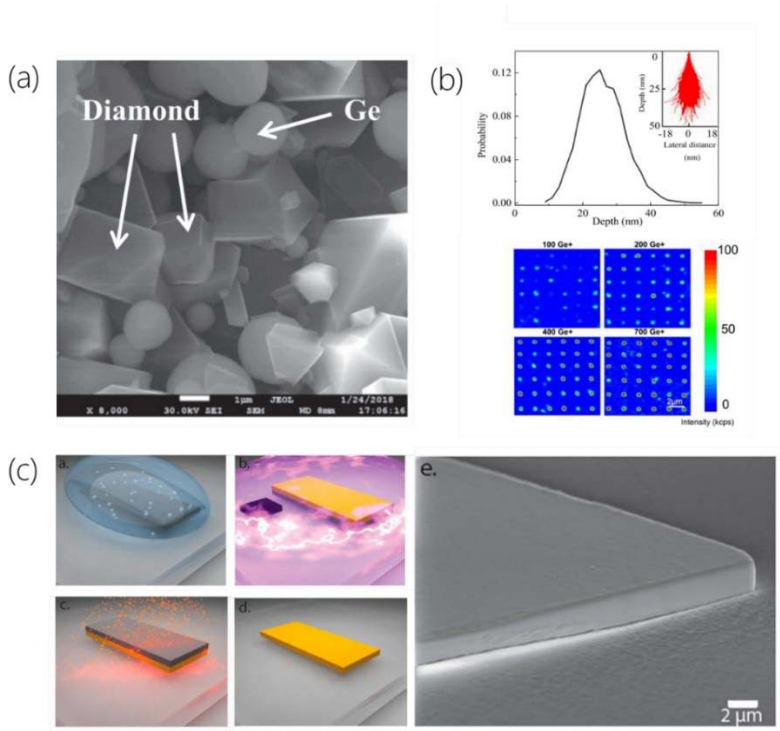

Figure 2.7. Various syntheses of GeV centres in diamond. (a) HPHT diamond synthesis. (b) Creation of GeV arrays via ion-implantation. (c) Schematic of the fabrication technique for the integration of GeV centres into a single-crystal diamond membrane. (d) SEM image of a thinned diamond membrane containing GeV. Reproduced from Ref.[87,90,91]

Additionally, having a non-silicon related colour centre also allows for higher incorporation control during doping, as silicon is known to be a common impurity during CVD diamond growth. GeV creation in existing bulk diamond by ion implantation has also been reported[91]. By using a focused ion beam (FIB), GeV ions were accelerated towards the surface of CVD-grown single crystal diamond at varying ion dosages, with increasing dosages resulting in a higher concentration of GeV centres [Figure 2.7 (b)].

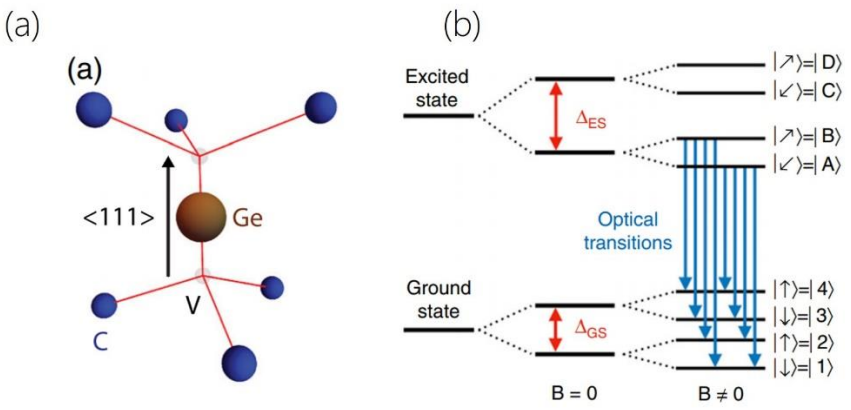

Figure 2.8. Structural and photophysical characteristics of the GeV defect. (a) Schematic illustration showing the inversion symmetry of the GeV. (b) Electronic structure of the GeV colour centre, showing doubly-degenerate ground and excited states and the possible optical transitions between them. Reproduced from Ref.[80,92]

Further refinement of the various synthesis techniques then eventually led to the creation of GeV centres at the single level, allowing a closer photophysical study of its quantum emitting properties. As mentioned earlier, the GeV defect structure is that of an inversion symmetry, a configuration referred to as D_{3d}, [Figure 2.8 (a)] where the Ge atom sits between two carbon vacancies within the ⟨111⟩ direction as the principle three-fold rotation axis (C3)[80,92].

Like SiV, the GeV ground-state is a spin-half system, where spin-orbit coupling splits the ground and excited states, forming a four-level system *via* double-orbital degeneracy [Figure 2.8 (b)]. Spin-orbit coupling and Jahn-Teller interactions lift the orbital degeneracy, which lead to splitting once again of the ground and excited states degenerate energy levels, to form a double spin degeneracy (S=1/2)[93,94]. Their eigenstates possess corresponding optical and phononic transitions, which are spin conserving and only couple to the relevant orbital degree of freedom, allowing for the possibility of all-optical coherent spin control schemes[92].

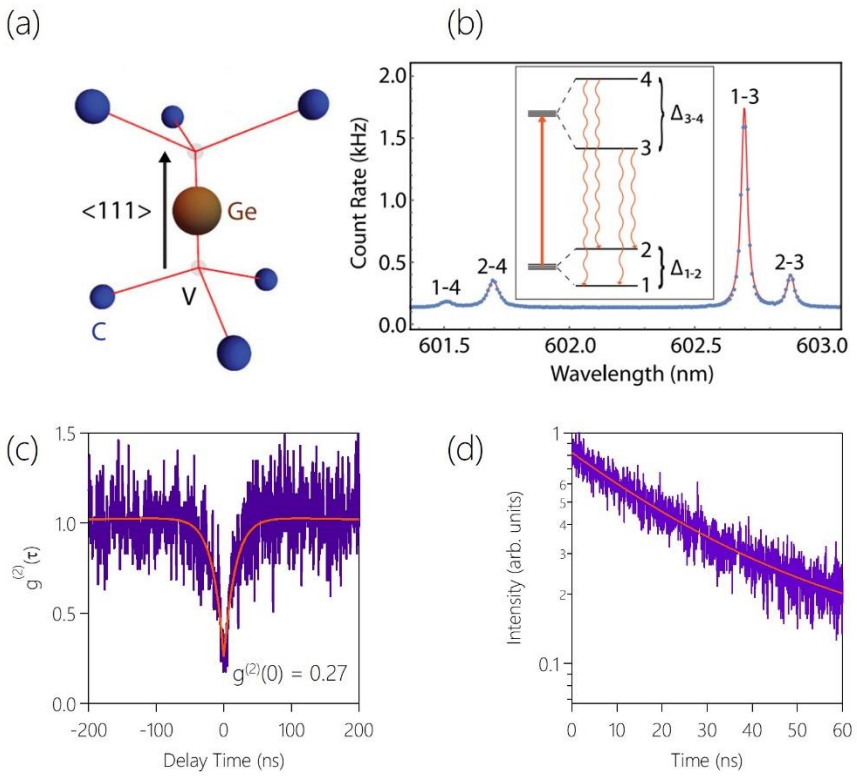

Figure 2.9. Optical characteristics of GeV single emitters. (a) An example of the ZPL measured at cryogenic temperatures, revealing the four different optical transitions. (b) Measured autocorrelation function showing quantum emission with a $g^{(2)}(0) = 0.27$. (c) Lifetime measurement of GeV colour centre in an ND showing an average lifetime of ~15 ns. Reproduced from Ref.[92]

Optically speaking, the splitting of the ZPL at approximately 602 nm can be observed at cryogenic temperatures, uncovering four lines—each associated with the four possible transitions [Figure 2.9 (a)]. Transition 1–3 is the dominating emission line, making up approximately 60% of the total GeV emission[89,92]. Quantum emission has been reported from GeV colour centres, and is noted to be stable, and bright (exceeding 100k counts at saturation). The average emission lifetime varies depending on the sample the defect was incorporated into. Bulk GeV colour centres are measured to have a lifetime of approximately 4–5 ns[91], while GeV centres in HPHT ND vary from diamond to diamond by a large margin of almost 20 ns, with lifetimes recorded anywhere between 6 to 26 ns[37]. This can be

attributed to factors such as ND size, changing the density of states surrounding the defect, as well as strain within the ND itself.

2.3.4. Quantum emitters in hexagonal boron nitride

hBN is a 2D van der Waals crystal with a wide bandgap of 6.03 eV. It possesses very durable physical properties—a high melting point and chemical stability. As such it has found many applications spanning industrial implementation as dry lubricants, binder and sealers, alongside commercial use in consumables such as cosmestics[95–97]. In addition to its favourable physical and chemical properties, it also exhibits novel optical properties, making suitable its use in a broad range of optical and electro-optical applications. Its layered structure allow it to be cleaved down to monolayers and exfoliated onto other existing 2D materials (such as TMDCs) to form heterostructures, acting as effective encapsulants and gate dielectrics[98].

hBN emitter synthesis and characterisation

Recently, it has found a rise in its emergence following the discovery as a host for SPSs by T.T. Tran et. al. in 2015[40]. In this study, emitters in hBN were 'activated' *via* thermal annealing at 850 °C in an Ar environment for 30 minutes, and was the first instance of the formation of the defect. Following this, further studies using plasma-annealing in gaseous environments[99], keV electron irradiation, pulsed laser ablation[100], and localised strain fields were found to activate single emitters[101]. Figure 2.10 below shows a summary of all the aforementioned studies.

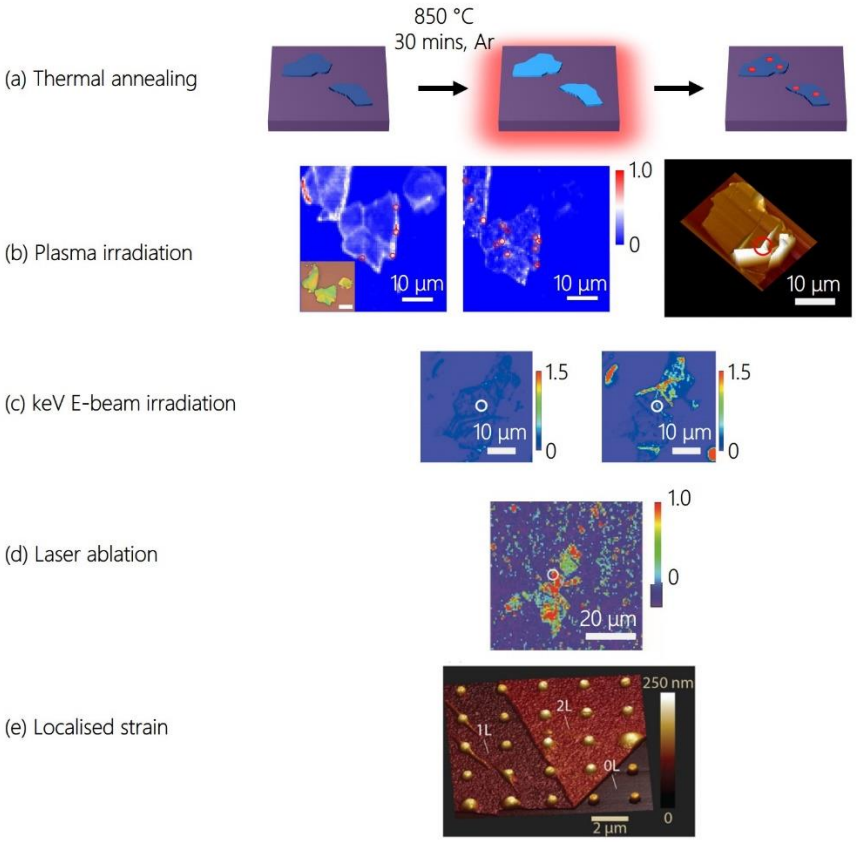

Figure 2.10. Summary of activation methods of quantum emitters in hBN. (a) Thermal annealing method, showing schematic of annealing process. (b) Plasma irradiation showing confocal scans (left and middle) of flakes after irradiation, and an AFM map showing their creation at the grain boundaries. The red circles indicate the spatial position of the emitters. (c) keV electron irradiation of flakes, showing confocal scans with the spatial position of an emitter (white circle) before (left) and after (middle) irradiation. (d) Laser ablation of a flake showing the resultant PL scan with many luminescent spots (e) Emitter activation using localised strain field, showing an AFM image of the flake over pillars. Reproduced from Ref.[99–101]

Upon excitation with a sub-bandgap source, emitters formed in hBN exhibit a sharp ZPL emission with a pronounced PSB doublet redshifted by approximately 160 meV from the ZPL (Inset Figure 2.10). Characterised hBN emitters do not have a fixed ZPL such as SiV or NV, but instead emit across the spectrum, from UV to IR[23,102–104]. Figure 2.11 below exhibit characteristic ZPL energies from hBN, from 532 nm CW excitation.

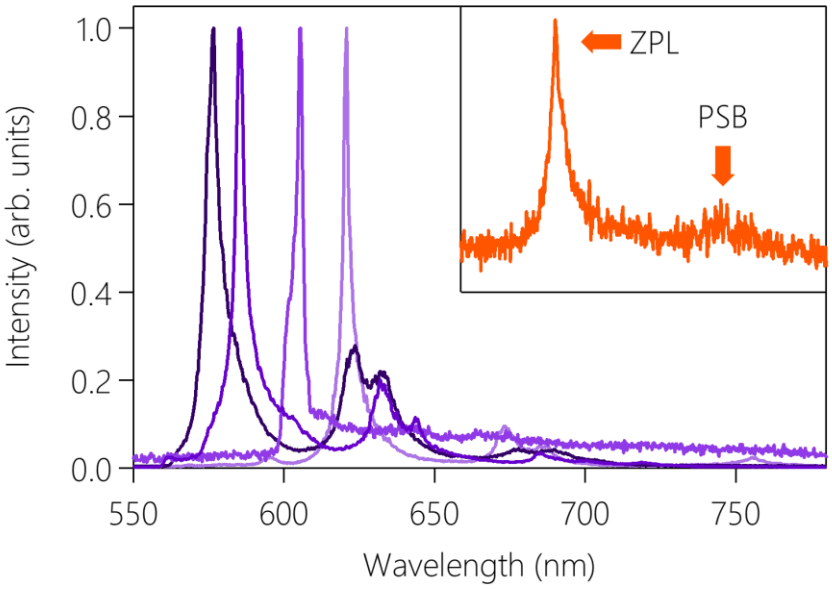

Figure 2.11. ZPL energies of characteristic hBN emitters. Inset illustrates the ZPL and PSB of the hBN emitter.

Figure 2.11 exhibits characteristic ZPL energies from hBN, from 532 nm CW excitation. Low energy phonon coupling from the crystal is the most likely cause of the asymmetry in the ZPL lineshape. There currently exists a surge in momentum surrounding the research into hBN emitters, despite the origins of the emitters still very much up to debate. Through first-principles and Direct Functional Theory (DFT) simulations performed, there have been theorised many potential atomic arrangements acting as the source for the hBN emission (Figure 2.12)[105].

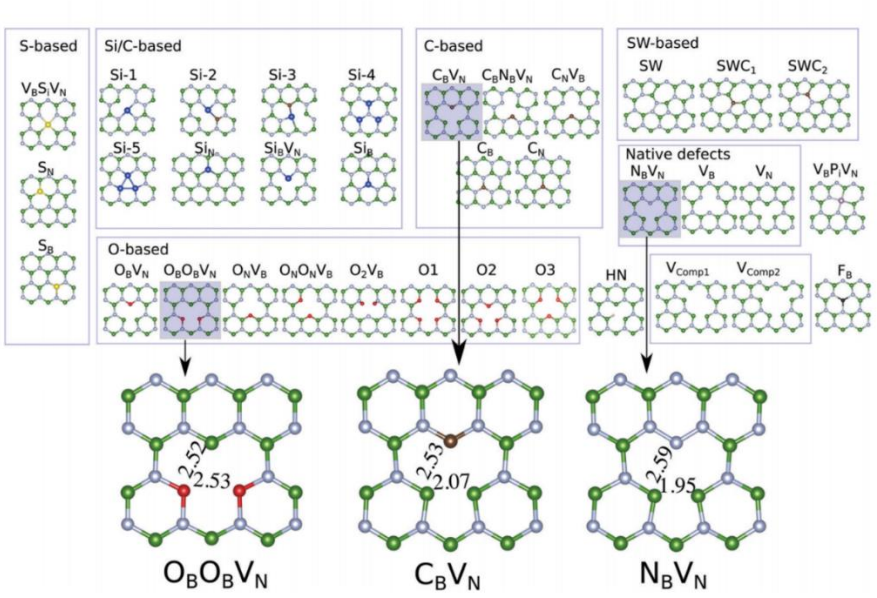

Figure 2.12. DFT calculations of potential defects responsible for the quantum emission measured in hBN. The three most likely candidates as hypothesised from this ref. are the $O_BO_BV_N$, C_BV_N, and N_BV_N. Reproduced from Ref.[105]

In the first demonstration of an SPS from hBN, a defect complex comprised of a nitrogen vacancy adjacent to an anti-site nitrogen (N_BV_N) was hypothesised as the likely defect, based on DFT simulations accounting for the observable emission energies[106]. However, later studies following this will bring forth other potential defect arrangements such as the emitters in carbon-incorporated hBN having been reported as the potential defect in a study by Mendelson et. al[107]. These samples were grown through metal-organic chemical vapour deposition (CVD) and molecular beam epitaxy (MBE) in an attempt to understand the role of carbon in the defect emission, with results of DFT calculations and probing of numerous defect transitions suggesting that the emission originates from the negatively charged V_BC_{N-} defect. A new class of emitters involving negatively charged Boron Vacancies (V_{B-}) have also been observed, showing defect emission and even spin-manipulation via ODMR measurements[108,109]. Additionally, coupling to the surrounding environment through processes such as host material strain can result in shifts of the ZPL

energies, subsequently resulting in the varying ZPL emission wavelengths[23,110,111].

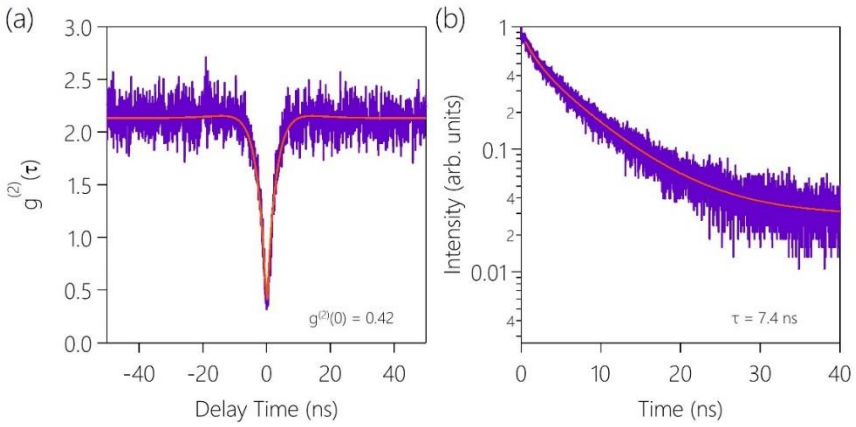

Figure 2.13. Optical properties of quantum emitters from hBN. (a) Autocorrelation measurement showing quantum nature of the defect. (b) Fluorescence lifetime of the hBN defect.

The quantum emission reported from defects in hBN, is the driving force behind the popularity of the material. Figure 2.13 (a) shows a second-order correlation measurement, used to probe the quantum nature of collected photoluminescence (PL). The measurement itself will be expanded upon in Chapter 3.2 and 3.3, however, in short, the histogram can be understood as the probability of detecting two photons simultaneously at both detectors, with an emissive source qualifying as a SPS so long as the minimum value of the histogram is below 0.5. The electronic structure of hBN emitters follow a three-level energy system, consisting of a ground state, excited state, and metastable state[40,112]. These emitters undergo radiative relaxation from the excited state within a few nanoseconds, an example of which in Figure 2.13 (b) showing a time-resolved PL measurement indicating a lifetime of 7.4 ns. As a result of the short lifetime, emitters in hBN exhibit high saturated emission count-rates easily averaging over 1M counts, regarded as one of the brightest quantum emitters to date. Its emission showing also to be photostable at both ambient and high temperatures, with studies showing the single-photon emission from

room temperature up to 800 K[113]. Despite, a ZPL red-shift as temperature increases, the emission itself is photostable, void of PL fluctuations from maximum to zero (known as blinking).

Generally, one can expect all hBN emitters to have two common properties, namely, high brightness, and fully-polarised emission regardless of emission energies. The latter of which has been revealed through measurements on the emitters, showing a single linear transition dipole moment, evident through measurements of collected PL as a function of linear polarisation angle (Figure 2.14)[40,114]. Due to the 2D nature of hBN, the defect dipole is expected to be aligned in-plane with the rest of the crystal, subsequently resulting in the collection of fully-polarised emission. Below shows several plots of intensity as a function of linear polarisation angle, collected for both absorption and emission.

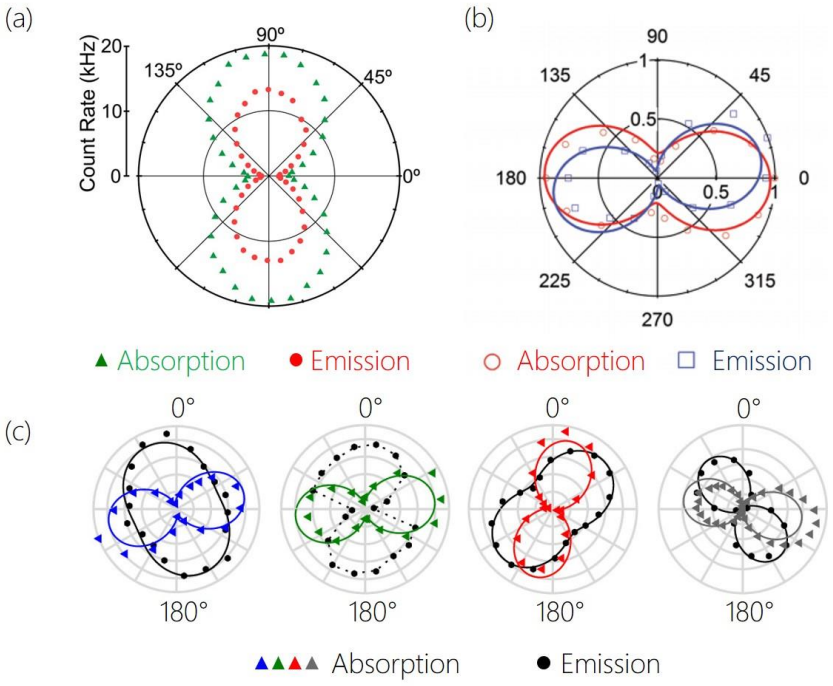

Figure 2.14. Linear polarisation of hBN emitters. (a) Linear polarisation of a hBN single-emitter, showing matching absorption and emission polarisation. (b) Another hBN single-emitter, but however showing slight mismatch between absorption and emission polarisation. (c) Four examples of the variation between mismatch,

and dipole orientation and their effect on emitter polarisability. Reproduced from Ref.[100,111,114]

When measured at an excitation energy close to the ZPL ($\Delta E < 200$ meV), the absorption and emission dipoles can be expected to align with each other, following the Huang-Rhys model where polarisation selection rules are identical for both processes. Contrarily, an excitation energy higher than that of the ZPL ($\Delta E > 200$ meV) will result in indirect absorption through intermediate states, resulting in non-radiative transitions occurring, exchanging momentum with the lattice and resultantly changing absorption and emission dipoles. The linear transition dipole found in hBN single emitters is yet another intriguing property possessed by the defect and can be exploited to great effect during integration with other components. The details of this will be expanded in Chapter 6.2

Chapter 3

Measuring single photons

The measurement of photons at the single level requires specialised techniques to help combat the low signal collected as well as the competing background luminescence, which is unfortunately never truly expelled. As all solid-state quantum systems are nanoscale optical systems, a method by which to selectively probe and collect its emission is required to characterise their properties. This chapter introduces the concept of optical microscopy, as well as more specialised techniques for the measurement of single photons in labs world-wide—that is; Fourier plane imaging, and time-correlated/time-tagged single photon counting.

3.1. Optical Microscopy

The optical microscope stands as the of the oldest designs of microscope, its origins founded by early lens makers and has been widely used across an expansive number of scientific disciplines dedicated to imaging small objects, since its inception in the 17th century. Within this section, a brief overview of the basic operations of optical microscopy are detailed, followed by introductions to additional imaging methods—confocal microscopy, and Fourier-plane imaging—invaluable techniques for the photoluminescence measurements of quantum sources.

3.1.1. The microscope objective

The microscope objective serves as the core component used in PL imaging of nanophotonic sources and is the first and most important

lens system within a microscopic setup. The objective is directly responsible for controlling the amount of light collected and quality of the image observed. Figure 3.1 shows a schematic of the basic working principle of an objective lens, helping to visualise how images are transformed within the objective to produce a final larger image.

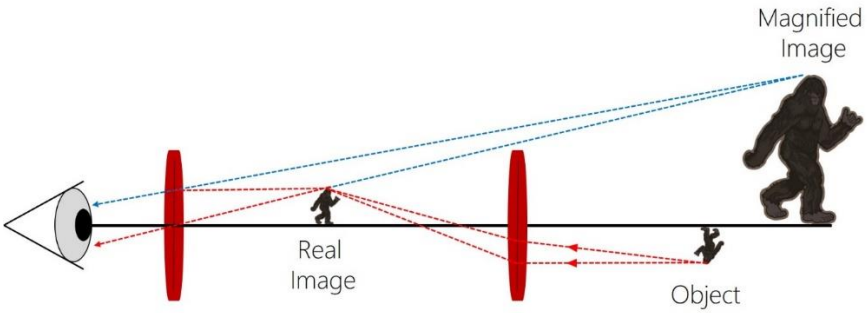

Figure 3.1. Simplified schematic diagram showing how light travels through an objective to produce a magnified image, with the assistance of a sasquatch.

Two primary components typically constitute a microscope objective; the objective lens itself which collects light and allows the projection of an infinity-corrected collimated beam, and the tube lens system which forms the intermediate image to be transformed[115,116]. The operation of the objective microscope is defined by a number of key properties, which must be taken into consideration for specific applications;

Numerical aperture

The numerical aperture of an optical system is a measure of the amount of possible incoming light which can be accepted. It is defined as the product of the refractive index of the medium ($n = 1$ for air) through which the input signal (n) is received and the sine of solid angle (θ), given by:

$$NA = nsin\theta \qquad \text{Eq 3.1}$$

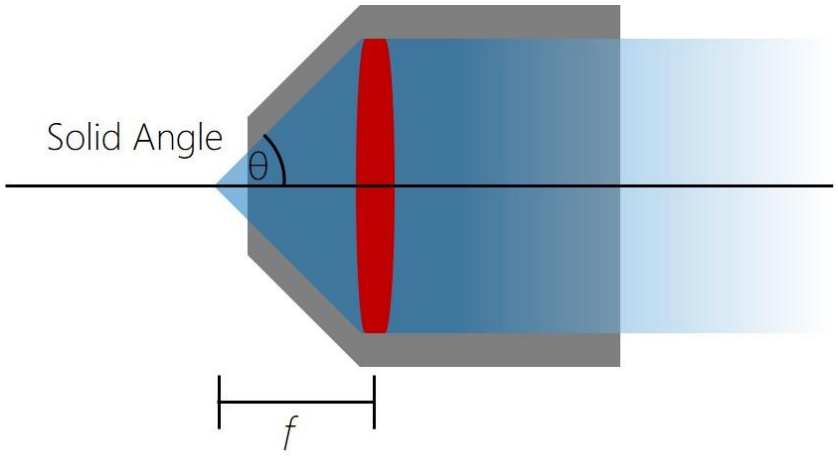

Figure 3.2. Schematic illustration of an objective showing the focal length f, and the solid-angle, ϑ.

An increase in the solid angle, results in an increase in the amount of photons collected. Air objectives can have NAs ranging from 0.2 up to the maximum of approximately 0.95. Liquid and oil-immersion types can further increase this, reaching up to 1.4 NA[115,116].

Magnification

Magnification (M) in an optical microscope is dependent on the focal length of the tube lens (f_{tube}), and the focal length of the objective (f_{obj}) and is given by the relation:

$$M = \frac{f_{obj}}{f_{tube}} \qquad \text{Eq 3.2}$$

While increasing the magnification of an objective lens will allow one to observe finer details from a sample, there reaches a threshold where features themselves will not resolve further as they become limited by the diffraction limit[115,116].

Resolution

Resolution (R) is the ability of the microscope to resolve features and is defined as the shortest distance between two points of an image that can be distinguished by the optical system. Three separate mathematical concepts are considered in the context of resolution;

Abbe's diffraction limit, the point spread function (PSF), and the Rayleigh Criterion. At an optimally focused point of light determined by a circular aperture in a perfectly aligned system, a diffraction consisting of Gaussian spot will form with concentric circles in surrounding. This is known as an 'Airy disk', defined mathematically by the PSF. In the case of two distinct features (i.e. two Airy disks), the Rayleigh Criterion would be met if the two Airy Disks do not overlap and are easily distinguishable. Resolution is also wavelength and NA dependent, with resolution increasing while imaging with shorter wavelengths and higher NA components, as stated with the Abbe's theory on diffraction. Combing these properties, the resolution of an optical system can be calculated using the formula;

$$R = \frac{0.61\lambda}{NA} \qquad \text{Eq 3.3}$$

In this case, the value 0.61 is a constant based on derivations from Rayleigh's work on Bessel functions[115,116].

3.1.2. Confocal Microscopy

Resolution in PL imaging can be marginally increased via the technique of confocal microscopy, which operates on the principle of increasing contrast between the fluorescent features imaged and the unavoidable, surrounding background luminescence. Figure 3.3 shows a schematic of a typical confocal microscope, with several key components labelled.

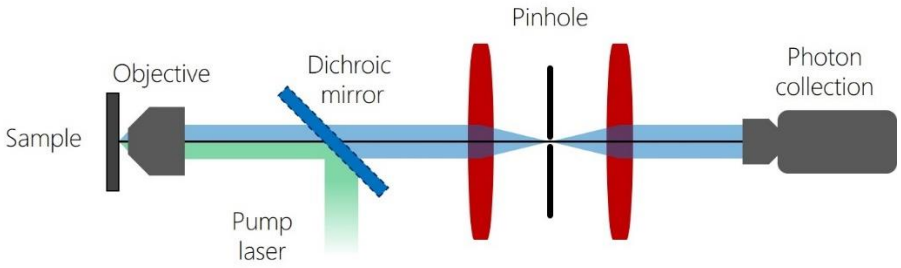

Figure 3.3. Schematic diagram of a typical confocal microscope with the key components labelled.

The pinhole is the key component constituting a confocal microscope, responsible for the reduction in fluorescence background and increasing image resolution. It does so by only allowing a small plane of focus to pass through to the photon detectors, while rejecting all other light rays focused at other planes. Optical fibres used to collect and direct emission towards the detectors may also serve as a confocal pinhole in some setups. Additionally all background light rays which do not pass through the pinhole are subsequently also rejected. Optimal background reduction and resolution is achieved through the correct choice of pinhole size, D, determined by the equation;

$$D = \frac{\lambda f}{r} \qquad \text{Eq 3.4}$$

where λ, f, and r are the excitation wavelength, focal length, and beam radius, respectively. To complete the confocal microscope, a scanning system used to raster an image is usually also implemented, of either sample-scanning or laser-scanning configurations[117,118].

3.1.3. Fourier plane imaging

Fourier plane or back-focal plane (BFP) imaging is another imaging technique commonly used in the measurement of single molecules, which provides an alternative set of data that conventional PL image-plane microscopy cannot produce. Imaging at the Fourier plane of an optical system reveals emission wavevector information, which is

useful when understanding light-matter interactions and how certain nanophotonic components can modify emission directionality.

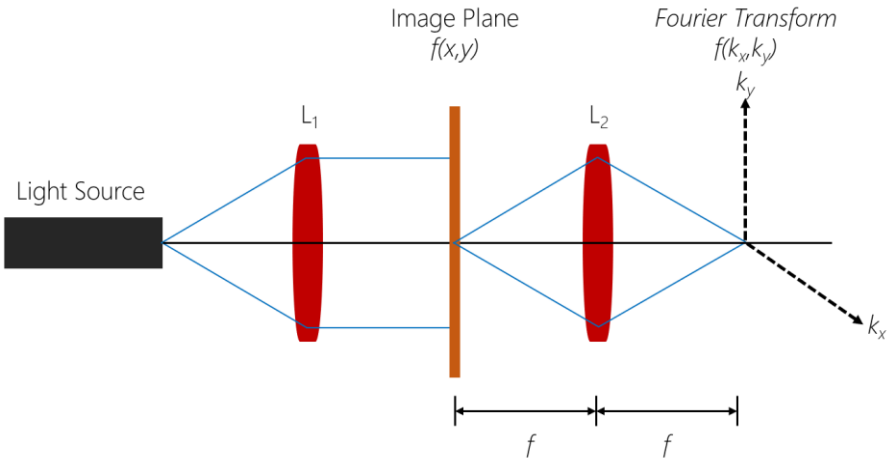

Figure 3.4. Schematic illustration of a Fourier transform using a lens system. An object illuminated by a collimated light source will undergo a Fourier transform as the image travels through a lens. The resultant intensity distribution will appear at the back-focal plane.

Figure 3.4 shows a conceptual schematic of a Fourier transform using a lens. An object illuminated by a collimated wave will be projected onto the image plane $f(x, y)$ using a lens (L1). A second lens (L2) will then perform a Fourier transform of the image, at a plane which is transverse to the rear focal point of the system—the BFP. At this point, all propagated light waves entering the system will intersect and contain scalar field information of phase and amplitude, manifesting as an intensity distribution—directly related to the Fourier transform of the object plane, given as

$$E(x, y : z) \quad = \quad \iint_{-\infty}^{\infty} \hat{E}(k_x, k_y; z) e^{i[k_x x + k_y]} dk_x dk_y \qquad \text{Eq 3.5}$$

During the transform, each point on the object plane before the lens (x, y) is mapped into its reciprocal (k_x, k_y) in momentum space on the back focal plane[116,119]. From the distribution in k-space, one can

visualise the vectors of the light waves as they travel through space and the resultant far-field emission patterns produced from the source.

Experimentally, the back-focal plane of an optical microscope setup differs from objective to objective, but is commonly positioned within the housing and is not accessible—typically requiring relay optics to 'transport' the image to a suitable and more easily viewable point in the system. $4f$ lens arrangements are most common in performing this, however, other relay lens systems involving a single lens are also possible as shown below in Figure 3.5[119].

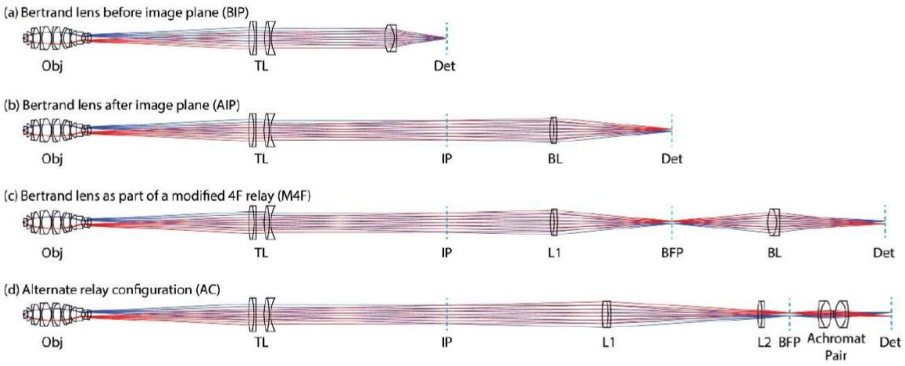

Figure 3.5. Examples of various setups used for back-focal plane imaging. From top to bottom; Betrand lens before image plane, Bertrand lens after image plane, Modified 4F relay, alternate relay configurations. Legends; TL: tube lens, IP: image plane, BFP: back-focal plane, Obj: Objective. Reproduced from Ref.[119]

Characterisation of single-defects using BFP

BFP imaging proves an invaluable tool in the characterisation of single-defects and can reveal much about physical and electronic structure. Dipole arrangement, 3D orientation, and intensity can all be determined through the far-field emission pattern, although many factors influence the observed intensity distribution, including; objective solid angle, and refractive index of the medium through which it is measured. Figure 3.6. shows simulated examples of the varied aforementioned factors.

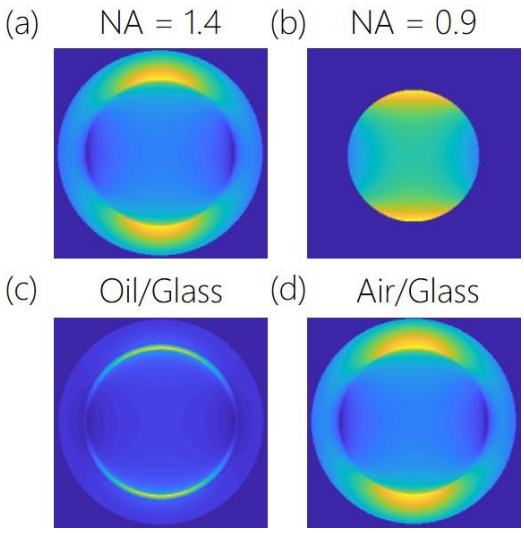

Figure 3.6. Simulated images of a single-defect in BFP, showing the effects of changing conditions. (a) and (b) highlight the changes in NA, while (c) and (d) show the change in refractive index as light travels through their respective mediums.

In the case of single defects, the orientation of the dipole in 3D can be easily resolved considering its radiation pattern. Figure 3.7 (a) shows an emitter with a linear-transition dipole moment. It is expected to produce a taurus-like emission pattern orthogonal to its transition dipole.

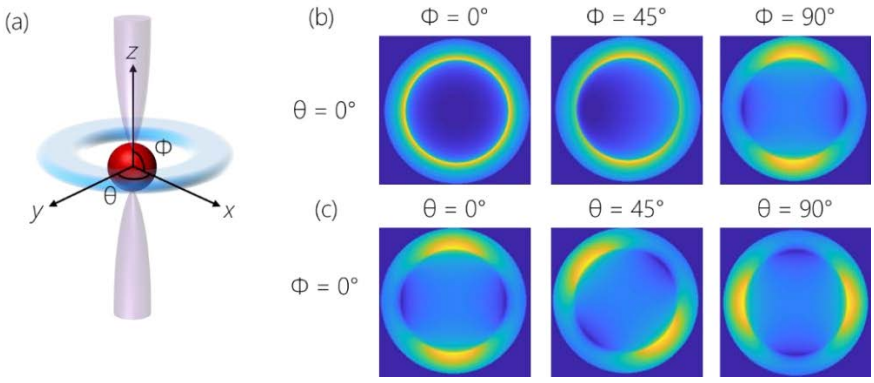

Figure 3.7. BFP from a single dipole. (a) Schematic illustration of a single-dipole emission pattern. The pink lobes represent the electron wavefunction, while the blue ring indicates its emission pattern. (b) Far-field intensity distribution as a function of azimuthal dipole angle. (c) Far-field intensity distribution as a function of radial dipole angle.

Figure 3.7 shows simulated far-field radiation patterns of a single-dipole with varying radial (ϑ) and azimuthal (Φ) angles. The intensity distributions produced in BFP can be fitted to corresponding ϑ and Φ angles, allowing the determination of the dipole orientation in 3D—a technique used commonly in practice for the measurement of single dipoles as well as coupled systems[37,75,76,79,81].

3.2. Single-photon collection and analysis

In addition to the techniques mentioned above, there exist specialised methods used when probing and characterising the quantum characteristics of light sources. From the theoretical foundations in Chapter 2, the experimental component will then be explained and discussed within this section.

3.2.1. The Hanbury-Brown and Twiss interferometer

Originally created to measure the distance between celestial objects, the Hanbury-Brown and Twiss (HBT) interferometer has been adapted for correlative measurements and is a staple of all quantum PL measurements—one of the main measurements responsible for identifying and characterising quantum emission. Figure 3.8 shows a typical schematic of a HBT interferometer, commonly seen integrated into the collection pathway of a confocal setup.

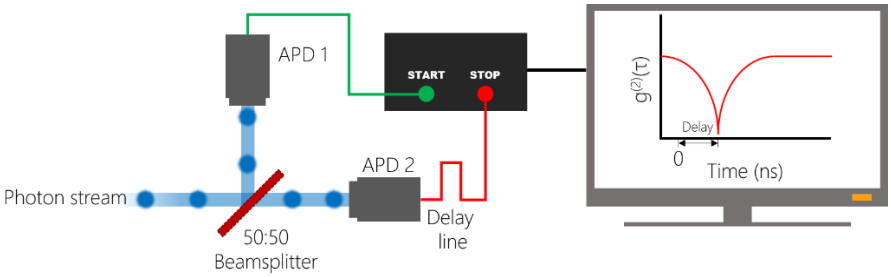

Figure 3.8. Basic schematic and working principle of a HBT interferometer. A 50:50 beam splitter sends the collected emission towards two APDs, where they are correlated as a function of time differences between detection at one end and the other. The

resultant histogram which follows can be fitted with the autocorrelation function, where quantum emission can then be determined.

Modern day avalanche photodiodes (APDs) are capable of very high SNR and are sensitive enough to detect single photons, and are the primary detection device used in all single-photon counting measurements[120]. However, there is a minimum time interval that exists between consecutive counts in order for the detector to record the signals as two separate events—known as dead-time. Thus, the HBT interferometer collects the photon stream and sends it towards a 50:50 beam-splitter whereby it is split equally into two APDs. The inputs of the two APDs will initiate an electronic pulse to a correlator card which records the pulses in two separate channels, the 'start' and 'stop' channels. The former will initiate a high-resolution timer, while the latter will stop said timing and from this, overcomes the dead-time of a single detector[33,121,122]. The product is a histogram of times between start and stop signals from which, the $g^{(2)}(\tau)$ autocorrelation function of the emission can be extracted, based on the concepts expanded upon in Chapter 2.2.2.

3.2.2. Time-correlated single-photon counting

The measurement of the temporal properties of single photons can be performed using time-correlated single-photon counting (TCSPC), or its most commonly referred 'lifetime' measurements. By utilising single-photon detectors and the ultra-fast electronics given by the correlator card, one is capable of measuring the arrival times of photons down towards picosecond time scales[121]. Lifetime measurements require the excitation of the quantum emitter with a pulsed excitation source, followed by measuring the arrival of the subsequently emitted photons relative to the initiation of the excitation pulse. Single-photon sources specifically require specific pulse settings—the total time of a single pulse must be less than the

average lifetime of the SPS, while the interval between pulses must be greater than that average lifetime. What results is a cumulative measurement of total arrival times, showing a distribution of events which can be fitted to various exponential functions, depending on the system measured.

3.2.3. Time-tagged single-photon counting

Time-tagged single-photon counting allows for the determination of quantum emission, through the implementation of the theory grounded from Chapter 2.2.2—now experimentally referred to as the $g^{(2)}(\tau)$ autocorrelation function. Recounting the solutions for the second-order correlation measurement, a single-photon emitter can be determined with the expression $g^{(2)}(\tau) = 1 - \frac{1}{n}$, describing the probability of detecting two photons at a specific delay time τ. Based on this equation it is widely accepted that a single-photon source can be defined by the autocorrelation function at zero-delay time less than 0.5 ($g^{(2)}(\tau) < 0.5$), with a perfect source without any background luminescence equaling zero. This manifests as a characteristic dip when fitting the $g^{(2)}(\tau)$ autocorrelation function to the second-order correlation histogram. Quantum emitters radiating through a two-level system will experience photon antibunching, however it is also possible to experience photon bunching at longer time scales, manifesting as values of $g^{(2)}(\tau) > 1$ at non-zero delay times at high pump powers[33,123]. An example of this is shown in Figure 3.9 (a), showing the $g^{(2)}(0)$ measurement of an NV^- colour centre exhibiting photon bunching.

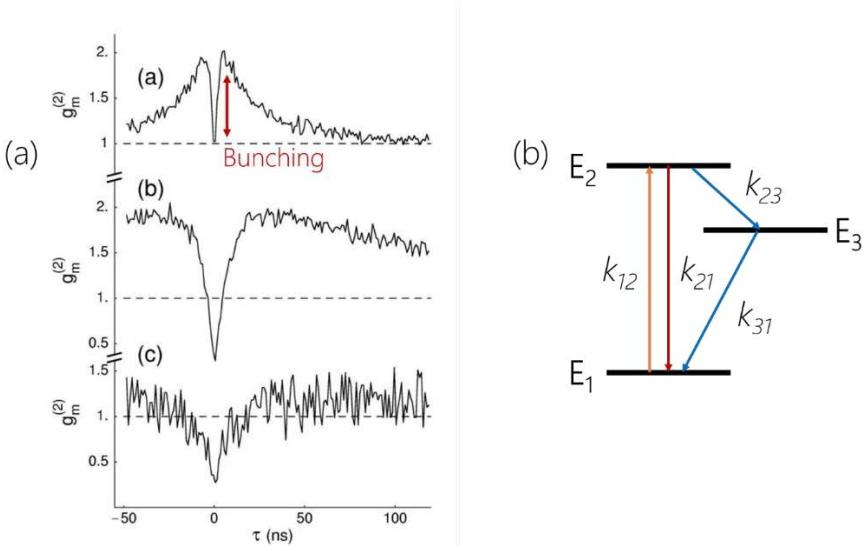

Figure 3.9. $g^{(2)}(\tau)$ measurements on NV- colour centres. (a) Three separate autocorrelation measurements performed as a function of excitation power, showing bunching at higher powers. (b) Three-level energy model, explaining how transitions to a longer-lived metastable state causes bunching mechanisms. Reproduced from Ref.[124]

This can be explained by introducing a third, longer-lived energy level, often referred to as the metastable state. The basic schematic of a three-level energy diagram is shown in Figure 3.9 (b). Here, E_1, E_2, and E_3 represent the ground, excited, and metastable states respectively, while the k-constants represent the transition rates between its corresponding labelled energy levels. The evolution of population dynamics is therefore given by[125]:

$$\frac{d}{dt}\begin{pmatrix} n_1 \\ n_2 \\ n_3 \end{pmatrix} = \begin{pmatrix} k_{12} & k_{21} & 0 \\ k_{12} & -k_{21}-k_{23} & k_{32} \\ 0 & k_{23} & -k_{32} \end{pmatrix} \cdot \begin{pmatrix} n_1 \\ n_2 \\ n_3 \end{pmatrix} \qquad \text{Eq 3.6}$$

with the initial conditions $n_1 = 0$, $n_2 = n_3 = 0$ at $t = 0$, indicating that the photon has just been emitted and the system is thus prepared in its ground state. For systems of this nature, the spontaneous emission probability of a photon is proportional to $n_2(t)$, which can be expressed in terms of the second-order autocorrelation function through normalisation of $n_2(t)$ to $n_2(t \to \infty)$. By disregarding the non-radiative transitions from the metastable to ground state (k_{31}), the

autocorrelation function in a three-level system can then be expressed analytically as:

$$g^{(2)}(\tau) = 1 + c_2 e^{-\left(\frac{\tau}{\tau_2}\right)} + c_3 e^{-\left(\frac{\tau}{\tau_3}\right)} \quad \text{Eq 3.7}$$

where the decay times and their coefficients are given by:

$$\tau_{2,3} = 2/A \pm \sqrt{A^2 - 4B} \quad \text{Eq 3.8}$$

$$c_2 = \frac{(1 - \tau_2 k_{23})}{k_{32}(\tau_2 - \tau_3)} \quad \text{Eq 3.9}$$

$$c_3 = -1 - c_2 \quad \text{Eq 3.10}$$

with

$$A = k_{12} + k_{21} + k_{32} + k_{23} \quad \text{Eq 3.11}$$

$$B = k_{12}k_{23} + k_{12}k_{32} + k_{21}k_{32} \quad \text{Eq 3.12}$$

Through these terms, the steady-state population of the excited state, level 2 is then expressed by

$$Q_2(t \to \infty) = k_{23}k_{12}/B \quad \text{Eq 3.13}$$

indicating saturation behaviour as a function of the pump rate k_{12}.

Part II

Creation and Manipulation of Quantum Emitters

Chapter 4

Quantum emitters in Gallium Nitride

Single-photon emitters in GaN are gaining interest as attractive quantum systems due to well-established techniques for growth and nanofabrication of the host material, and remarkable chemical stability and optoelectronic properties as mentioned earlier in Chapter 2. Here, two separate studies were undertaken to further understand the nature of the quantum emitters hosted in GaN. The former, to uncover the origins and nature of quantum emitters during their creation, and the latter as a study into its fundamental optical properties and their feasibility as sources for quantum applications.
In Chapter 4.1., a systematic analysis of single-photon emitters across various samples produced under different growth conditions was performed. Explored, are the effects which intrinsic structural defects (dislocations and stacking faults), doping, and crystal orientation in GaN have on the formation of quantum emitters. The relationship between the position of the emitters and the location of threading dislocations is characterised via spectroscopy through PL measurements, atomic force microscopy (AFM), and cathodoluminescence (CL). It was found that quantum emitters do not correlate with stacking faults or dislocations; instead, they are more likely to originate from point defects or impurities whose density is modulated by the local extended defect density.

Chapter 4.2. details the investigation into the photophysical properties of GaN with the demonstration of resonant excitation of its quantum emitters. The emitters are shown as stable under non-resonant excitation and exhibit nearly Fourier-transform-limited lines of ~250

MHz under coherent excitation, the narrowest reported to date for GaN.

4.1. Effects of microstructure and growth on quantum emitters in gallium nitride

4.1.1. Introduction

As discussed earlier in Chapter 1, non-classical SPEs are one of the most fundamental components of quantum-based technologies—quantum computation, simulations, metrology, and communications being examples of such. Having stable, scalable, emitters with favourable optical properties are necessities for these applications, and is thus the reason why GaN has attracted much attention as a potential candidate as mentioned in Chapter 2.3.2. GaN offers the unique opportunity—which is the focus of this study—to explore and understand the nature of the quantum emitters located within its crystalline matrix, while potentially allowing for the design of strategies for controlling and ultimately engineering their properties[126]. This aspect is key, as controlling the quality—e.g., the accurate positioning of the emitters, the indistinguishability of the generated photons, as well as the ability to efficiently extract them from the crystalline matrix—is one of the major challenges many of the identified solid-state SPEs are still facing due to the complexity of the mesoscopic environment of the host material.

Growth of GaN on non-native (other than GaN) substrates also means that the large lattice as well as thermal expansion mismatch between the substrate and GaN can result in the formation of extended defects [e.g., threading dislocations (TDs)] and stacking faults, with the dominant defect depending on the growth orientation. In addition, foreign atoms can be readily introduced in the GaN matrix during

synthesis.[127,128] Although GaN devices seem to be remarkably robust to extended defects compared to many other semiconductors, TDs do result in a deterioration of the optical and electronic performance observed in GaN devices[58,72]—e.g., through carrier scattering and nonradiative recombination processes.

However, it is still unknown whether they play any role in the formation of quantum emitters. It has previously been hypothesised that the formation of GaN quantum emitters is associated with extended structural defects created during GaN epitaxy. To test this hypothesis and explore the nature of the quantum emitters, a systematic study of a number of GaN samples differing from one another in their density of TDs, the presence or absence of stacking faults, their doping, growth orientation, and geometry was performed. A detailed optical and spatial analysis of the quantum emitters found in each sample was provided. Following this, a detailed investigation into the spatial correlation between the emitters found by PL and the position of the TDs in the GaN lattice identified by CL and atomic-force microscopy (AFM) was then performed.

4.1.2. Growth of GaN samples

Eight different GaN samples were analysed, labelled A–H, each one synthesised under specific growth conditions. The goal was to explore—and potentially tailor—the effects different parameters would have on the formation of quantum emitters in GaN. Each one of the eight samples was thus synthesised to control for a set of specific characteristics:

- Density of dislocations
- Doping of the matrix with extrinsic impurities expected to create deep-level states
- Growth substrate

- Orientation of the grown GaN material itself and hence the nature of the dominant extended defect

The samples were grown using metal-organic vapour phase epitaxy (MOVPE) on two different substrates, sapphire and silicon[129,130]. The growth of crystalline material *via* metal-organic vapour phase epitaxy involves the reaction between two gaseous precursors, brought into a chamber with a non-reactive carrier gas. Surface reactions from the precursor species results in the incorporation of elements into a new epitaxial layer of crystalline material, while byproducts of the growth reaction are ejected back into space[131]. A schematic of the basic principle behind the growth is shown in Figure 4.1.

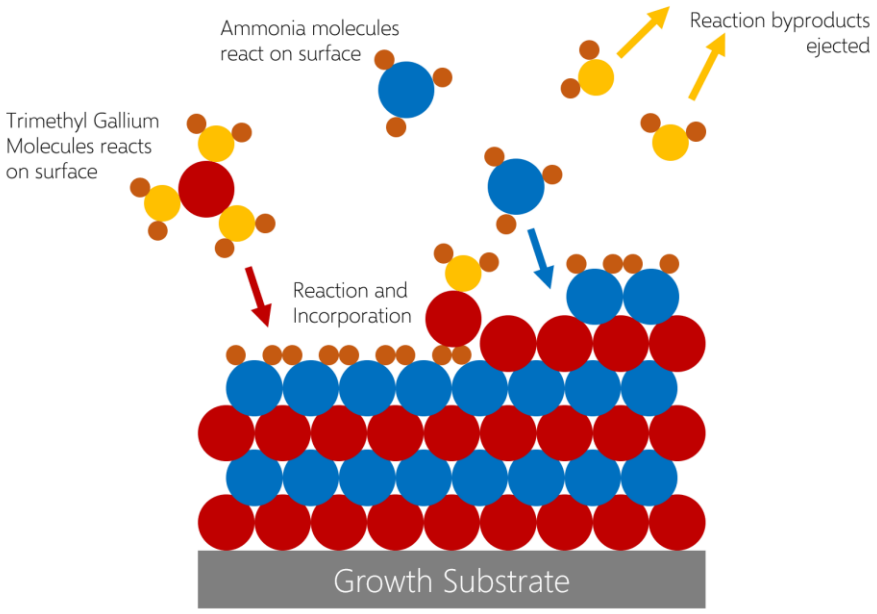

Figure 4.1. Schematic illustration of the MOVPE process used to synthesise GaN.

For GaN growth in these instances, trimethylgallium (TMGa) and ammonia (NH_4) were the precursors used. Parameters such as pressure, III-V ratio, and reaction temperature were modified for each growth, with the intention to explore the effects of certain properties on the formation of emitters—the details of them are as follows.

Density of dislocations:

Samples A, B, and C

These samples are c-plane (0001) GaN, which were deliberately grown under different conditions to have a substantial difference in the density of TDs in the GaN epitaxial layer: Sample A to have a high dislocation density of ~5 × 10^9 cm^{-2} (HDD) and Sample B a low dislocation density of ~3 × 10^8 cm^{-2} (LDD). An even lower density of TDs (~3 × 10^7 cm^{-2} in this case) can be achieved using epitaxial lateral overgrowth (ELOG), Sample C. The intent for these samples is to establish whether the number and position of crystallographic extended defects correlate with the number and position of deep defect states in the material, which has been the object of thorough, yet non-definitive, research[132]. It was noted that these samples are not expected to contain any significant density of extended stacking faults, although nm-scale stacking faults may occur when mixed dislocations dissociate. This comment is based on transmission electron microscopy studies of samples grown under similar conditions across a period of more than 10 years. Stacking faults are only typically seen in these c-plane materials either very occasionally in the region immediately adjacent to the GaN/sapphire interface, or when the growth is disrupted by a regrowth interface or heterostructure[133]. Neither of the latter two points is relevant to these samples.

Doping of the matrix via extrinsic impurities:

Samples D and E

These samples were grown with the intent to study the effects of extrinsic doping during growth, i.e., whether impurities—which in wide-bandgap materials can result in the formation of deep-level states in the bandgap—would create optically active colour centres within the GaN host matrix[14,134]. Samples D and E were synthesised to intentionally contain a high concentration of Carbon (C-doped) at 1.5

× 10^{19} cm^{-3} and Iron impurities (Fe-doped) at 1 × 10^{18} cm^{-3}, respectively.

Emitter formation with respect to the substrate:

Sample F

This sample was synthesised to investigate the formation of emitters in relation to the substrate on which the GaN structure was grown on. In this respect, GaN is a favourable choice as the wide availability of different methods of GaN growth allows for its synthesis on a variety of different substrates. Specifically, Sample F consists of n-doped, c-plane GaN grown on silicon. This resulted in an estimated threading dislocation density of 2 × 10^{9} cm^{-2}.

Orientation of grown GaN:

Samples G and H

Samples G and H were synthesised to explore the effect of crystal orientation on the potential creation of optically active defects. Sample G is nonpolar (11-20) GaN, while Sample H is semipolar (11-22) GaN. Heteroepitaxial nonpolar and semipolar GaN are known to contain large densities of partial dislocations and stacking faults but stacking faults may be considered the dominant extended defect. Sample G has an estimated TD density[135] of 3 × 10^{10} cm^{-2} and a basal plane stacking fault density of 3 × 10^{5} cm^{-1} , while Sample H has an estimated TD density[135] of 4 × 10^{9} cm^{-2} and a basal plane stacking fault density of 2 × 10^{5} cm^{-1}. Hence, these samples can be used to probe if stacking faults are playing any role in the formation of SPEs in GaN. Moreover, the unintentional impurity incorporation rate in semipolar material is faster than in the nonpolar one so that the doping in the nonpolar and semipolar sample will also differ, with a much higher density of oxygen impurities in the semipolar sample[136].

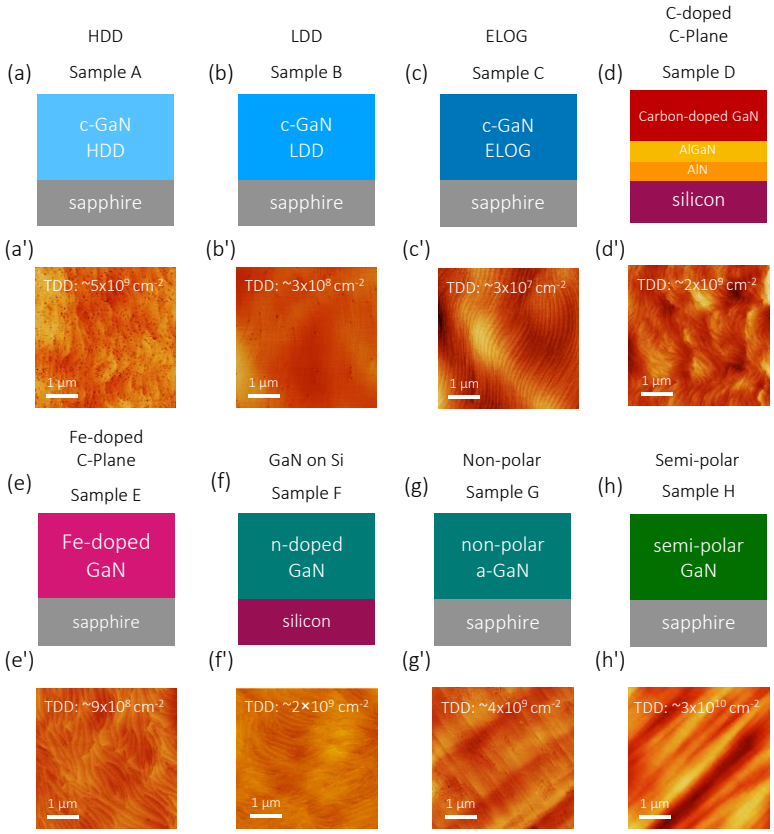

Figure 4.2. Schematic and topographical characterisation of all GaN samples investigated. [(a)–(h)] Schematics of c-plane HDD GaN (a), c-plane LDD GaN (b), c-plane ELOG GaN (c), C-doped GaN (d), Fe-doped GaN (e), n-doped GaN grown on silicon (f), nonpolar GaN (g), and semipolar GaN (h). [(a′)–(h′)] Topographical AFM scans for each corresponding sample. The threading dislocation density (TDD) is noted for each topographical scan. Reproduced from Ref.[126]

4.1.3. Optical Characterisation

In order to probe quantum emission from SPEs in GaN at room temperature, PL measurements were performed on all of the eight samples. The samples were characterised in a lab-built confocal microscope (details can be found in the Appendix). Briefly, the specimens were excited with a 532 nm continuous wave laser through a 0.9 NA air objective. The emitted light was collected back through the same objective, spectrally filtered and sent either to a spectrometer or to two avalanche photodiodes (APDs) arranged in a Hanbury Brown and Twiss (HBT) interferometer configuration for single-

photon detection. The PL spectroscopy measurements carried out on the eight samples are summarised in Figure 4.3.

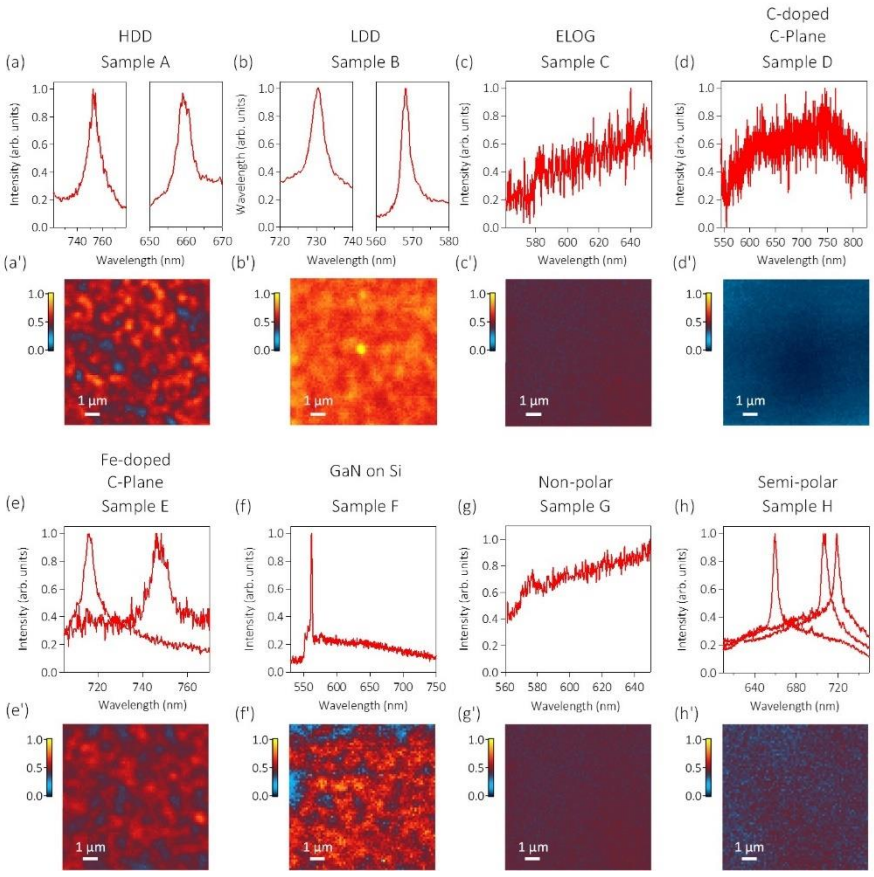

Figure 4.3. PL analysis of the emitters found in the GaN samples. [(a)–(h)] Representative PL spectra of various spots taken from each sample. Sample A, B, E, and H show distinct peaks associated with the PL of single emitters, while samples C, D, F, and G display a rather broad PL signal (the sharp peak in F is the Raman peak from the silicon substrate). [(a′)–(h′)] Corresponding 10 × 10 μm^2 confocal scans where the spectroscopy measurements were conducted. Specifically: HDD GaN [(a) and (a′)], LDD GaN [(b) and (b′)], ELOG GaN [(c) and (c′)], C-doped GaN [(d) and (d′)], Fe-doped GaN [(e) and (e′)], GaN on Si [(f) and (f′)], nonpolar GaN [(g) and (g′)] and semipolar GaN [(h) and (h′)]. All spectra were acquired upon excitation via a 532 nm CW laser. Reproduced from Ref.[126]

All samples grown on sapphire substrates displayed an intense background PL emission peak at 695 nm—which is known to be due to chromium impurities in sapphire[137]. Samples A, B, E, and H showed strong PL emission at other wavelengths. Figures 4.3 (a), (b), (e), and (h) show the spectra collected from each sample—the analysed areas

are displayed in the corresponding confocal scans [Figures 4.3 (a′), (b′), (e′), and (h′)]. Note that due to the high background signal, the emitters could not be clearly identified in the PL confocal scan; spectroscopy measurements were thus relied on to isolate the individual emitters. Samples A (HDD) and B (LDD) showed a high density of emitters with zero phonon line (ZPL) wavelengths ranging from 570 nm to 750 nm. Sample E (Fe-doped) showed distinct PL emission peaks at ~710 nm and ~750 nm, but the density of emitters was qualitatively lower than that observed in Samples A and B. In samples C, D, F, and G no emitters but only broad PL emission [Figures 4.3 (c), (d), (f), and (g)] was observed [note: the sharp peak in Figures. 4.3 (f) is the Raman peak from the silicon substrate].

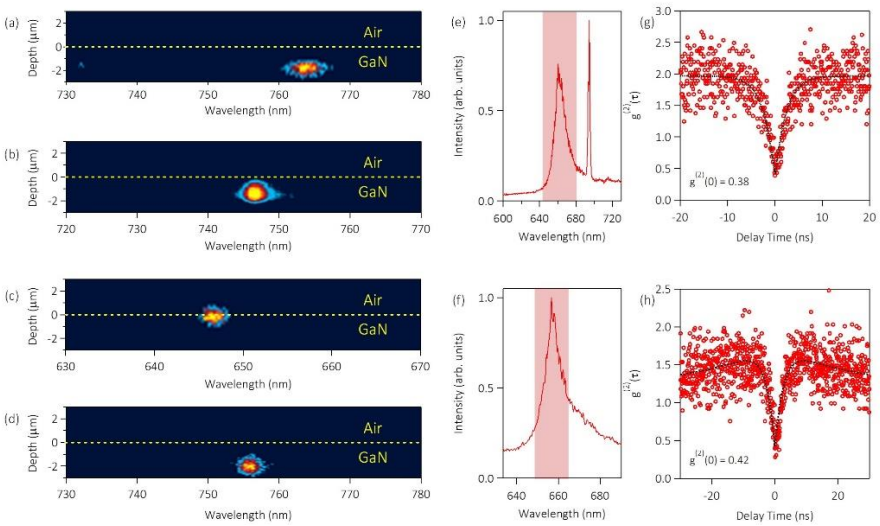

Figure 4.4. Optical analysis of emitters in GaN. [(a)–(d)] Depth-resolved PL measurements of emitters in HDD (a), LDD (b), Fe-doped (c), and (d) semipolar GaN. The yellow line indicates the boundary between the GaN surface and air. All depth scans were probed with 532 nm CW excitation. [(e) and (f)] Spectrum of representative emitters in LDD GaN chosen for autocorrelation measurements. The red box indicates the bandwidth of the collected signal after filters were used to eliminate background emission. [(g) and (h)] Corresponding second-order autocorrelation measurements $g^{(2)}(\tau)$ of the emitters in (e) and (f) showing their quantum nature [i.e., $g^{(2)}(0) \leq 0.5$]. Spectroscopy and autocorrelation measurements were performed with 532 nm CW excitation. Reproduced from Ref.[126]

To gather more information about the origin of the PL signal from the various samples, a more detailed analysis was conducted. For the HDD Sample A, LDD Sample B, Fe-doped Sample E, and semipolar Sample H the depth along the z-axis (orthogonal to the surface) at which the emitters were located in the GaN crystal were measured. This was achieved by collecting consecutive spectra of each emitter at multiple z-positions by varying the sample-to-objective distance in the confocal microscope. The plots from reference emitters in LDD, HDD, Fe-doped, and semipolar samples are shown in Figures 4.4 (a)–(d). Interestingly, it was observed that the emission in the HDD, LDD, and Fe-doped samples did not originate from emitters at the surface of the GaN crystal but rather from centres located deeper in the material, ∼1–2 µm beneath the surface. Studied were also the photon statistics of the PL emission with a HBT interferometer to investigate the presence of single-photon sources. For the emitters in Sample A (HDD), values were measured for the second-order autocorrelation function $g^{(2)}(\tau = 0) < 1$ (not background-corrected), yet not < 0.5—considered indicative of single-photon emission. This suggests that in this sample the centres are clustered groups of at least a few emitters per confocal spot area (linear size ∼500 nm). Single-photon emitters were instead found in Sample B (LDD). Figures 4.4 (e) and 4.4 (f) show typical PL spectra from isolated emitters in the LDD GaN sample. As state above, the peak at 695 nm [Figure 4.4 (e)] originates from chromium impurities in the sapphire and has been excluded from the autocorrelation measurement by applying a filter in the collection path—the spectral window analysed is shaded in red in Figure 4.4 (e) and 4.4 (f). The relevant second-order autocorrelation measurements are displayed in Figure 4.4 (g) and 3 (h) which shows values for $g^{(2)}(0)$ of 0.38 and 0.42, respectively (values are not background-corrected)—indicative of the quantum nature of the emitters.

4.1.4. Correlation between quantum emitter formation and material defectivity

The comparison between the spatial positions of the quantum emitters and threading dislocations were then drawn. Whilst the HDD and LDD samples (Samples A and B, respectively) were grown under the same conditions, indicating the nature of the emitters is likely the same, it is worth noting that the two samples involved different early stages of the growth, which results in different impurity incorporation into the region adjacent to the GaN/sapphire interface. However, the depth of the emitters identified from the confocal PL measurements does not correspond to this near-interface region and at the relevant depth both samples have similarly low oxygen concentrations of 3×10^{16} cm^{-3}. The two samples mainly differ in the density of the TDs—these being higher in the HDD sample than in the LDD one—which seems to correlate with the corresponding density of emitters—again higher in the HDD sample than in the LDD one. To quantify this precisely, the confocal scans (5×5 μm^2 area) of the two samples were analysed and the total number of emitters were compared directly [Figures 4.5 (a′) and (b′)]. In the HDD Sample A, 53 spots were identified containing emitters vs the 17 of the LDD Sample B—the results of this comparison shown below in Figure 4.5.

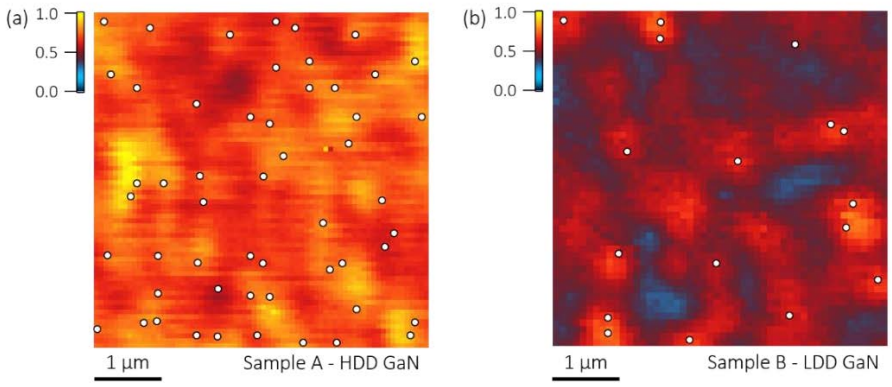

Figure 4.5. Confocal PL maps showing the difference in emitter density between (a) HDD and (b) LDD GaN. Spatial positions of emitters are indicated with white circles.

These amount to values for the planar density of emitters $\geq 2.1 \times 10^8$ emitters/cm^2 and $\geq 0.7 \times 10^8$ emitters/cm^2 for samples A and B, respectively. Simultaneously, the dislocation densities estimated from the growth process for the HDD and LDD GaN samples were $\sim 5 \times 10^9$ and $\sim 3 \times 10^8$ dislocations/cm^2, respectively. Analysis of these results suggests that a higher density of TDs corresponds to a higher density of emitters, with the caveats that the overall density of emitters is significantly lower (~4–25×) than that of the TDs, and that the TDs-to-emitters correlation is nontrivial—in the analysis a ~17× increase in TDs between Sample B and A corresponds to only a ~3× increase in emitter density. Note that for Sample A, due to the inability to identify single emitters clustered within the resolution limit of the confocal spot, the total number of emitters is underestimated—in fact, each bright spot in the confocal scan contains a few emitters, as indicated by the value of the second-order autocorrelation measurement: $0.5 < g^{(2)}(0) < 1$. Undoped LDD samples typically contain about 50% edge and 50% mixed TDs (of which 50% of the mixed dislocations are undissociated and 50% are dissociated). Given that there was no observable correlation between emitters and the presence of stacking faults (see Figure 4.6)[138], it is unlikely that mixed type dissociated dislocations relate to emitters.

Hence, the density of emitters may correlate more closely with the density of mixed type undissociated dislocations. It was noted that for the ELOG sample, which shows no emitters, the dislocation density varies periodically in bands across the surface and might thus be expected to exhibit corresponding bands of emitters, but this effect is absent. Overall, the data suggests a link between dislocations and emitters—yet not a simple one-to-one correlation. It should be highlighted here that these data provide no evidence for the previously hypothesised link between emitters and stacking faults[25] since there is no evidence for the presence of extended stacking faults in these samples and the samples with a significant stacking fault density show few or no emitters. On the other hand, no emitters were found in Sample F that was grown on silicon, despite a similar dislocation density to Sample B. This again suggests the relationship between the emitters and TD density is nontrivial and on a practical level suggests that sapphire may be the better substrate to use when trying to engineer emitters.

4.1.5. Spatial correlation of emitters and threading dislocations

To further analyse the relationship between dislocations and emitters, a multi-microscopy approach was employed to link the specific structural defects and optical signatures of those quantum emitters in GaN and carried out correlated characterisation of the GaN samples via CL and AFM and combined them with the photoluminescence PL data. The idea was to pinpoint the potential role of TDs on the formation of luminescent quantum emitters—i.e., establishing whether there is a direct spatial correlation between the positions of the emitters, characterised by PL, and the position of any TDs, measured by AFM and CL. Figure 4.6 summarises the result for Sample B (LDD), chosen for reference. In the figure, the same region is analysed

with the different techniques. Figure 4.6 (a) is an AFM scan of the area: crystallographic defects terminating at the surface (blue circles) are visible as pits with a diameter of < 10 nm. In this scan, mixed TDs are visible, but the smaller pits related to edge TDs are not resolved. Figure 4.6 (b) is the corresponding CL image: the dark spots arise due to nonradiative recombination at the dislocations' sites[139] and relate to both mixed and edge TDs. Hence, where the CL image black spots and AFM blue dots both show a feature in Figure 4.6 (c), it is likely to be a mixed dislocation, whereas when the CL image shows a feature which is not present in the AFM one, it is likely to be an edge dislocation. The density of TDs measured via CL is $\sim 4 \times 10^8$ cm^{-2} and is consistent with the value of $\sim 3 \times 10^8$ cm−2 estimated from the growth process. In Figure 4.6 (b), the overlaid red dots indicate the positions of the emitters measured separately in PL. Figure 4.6 (c) is an overlay of all these measurements and highlights a few interesting aspects.

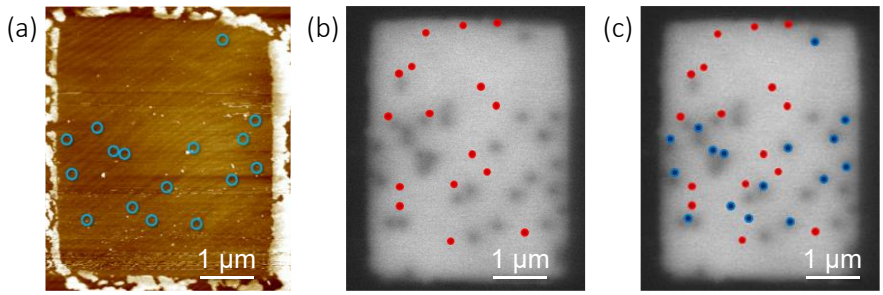

Figure 4.6. AFM, panchromatic CL, and PL measurements of LDD Sample B correlating the position of threading dislocations with the optical properties of GaN emitters. (a) AFM image of the characterised grid showing the positions (blue circles) of the dislocations as they terminate at the surface. Inset shows a magnified region in the grid specifically identifying a characteristic threading dislocation as imaged by AFM. (b) CL image of the same area. The (red dots) indicate the position of single photon emitters (SPEs) as characterised separately by confocal microscopy under 532 nm CW laser excitation (confocal scan not shown). The TDs appear as (black spots) in the CL image. (c) Overlay of images (a) and (b) showing the correlation between surface features spatially characterised in AFM (blue dots) and CL (black spots), and emitters characterised in PL (red dots). Reproduced from Ref.[126]

There were observed to be no obvious correlation between the position of the emitters detected in PL [red dots in Figure 4.6 (c)] and the dislocations measured by AFM and CL [blue dots and black spots in Figure 4.6 (c), respectively]. Thus, the possibility that TDs result in discrete states in the bandgap which localise the electron-hole pair can be excluded. If they did, in Figure 4.6 (c), every blue dot (AFM) would align with a black spot (CL) and a red dot (PL). Hence, one must consider why the TD density might correlate with the emitter density, without a direct spatial correlation between the two. One possibility is that the subsurface TD structure is not reflected in the CL and AFM measurements; thus, transmission electron microscopy (TEM) was used to investigate the structure of the TDs at the depth from which the emitters have been identified to originate in the confocal PL studies (1–2 μm below the top surface).

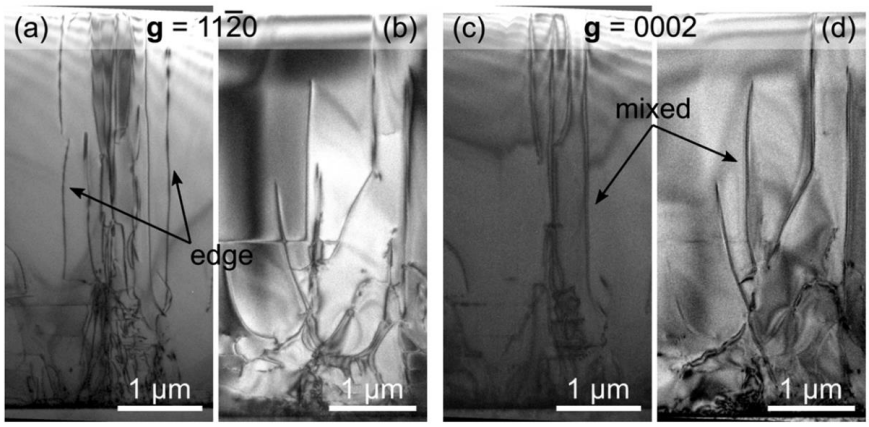

Figure 4.7. TEM analysis. Cross-sectional TEM images of Sample B (LDD), observed along the $1\bar{1}00$ zone-axis and diffraction conditions $\boldsymbol{g} = 11\bar{2}0$ [(a) and (b)] and $\boldsymbol{g} = 0002$ [(c) and (d)]. Edge-type dislocations are visible under $\boldsymbol{g} = 11\bar{2}0$ but not when $\boldsymbol{g} = 0002$. Inversely, screw-type dislocations are visible under $\boldsymbol{g} = 0002$ but not when $\boldsymbol{g} = 11\bar{2}0$—none could be seen in this image. Mixed-type dislocations can be seen under both conditions. Note that for all images, the GaN/sapphire interface is located very close to the bottom of the image and original GaN surface is located close to the top of the image. Reproduced from Ref.[126]

Figure 4.7 shows the results of such TEM analysis for two different regions of the LDD sample, with Figure 4.7 (a) and (b) ($\boldsymbol{g} = 11\bar{2}0$)

showing both edge and mixed dislocations, and Figure 4.7 (c) and (d) (g = 0002) showing only mixed dislocations (note that screw-type dislocations would be visible under g = 0002, if any). In all cases, the TDs run roughly vertically and are observed at a depth of 1–2 μm below the surface; very little bending is seen so that the CL and AFM images may be expected to be representative of the dislocation positions at this depth. At greater depths (3–5 μm below the surface, close to the GaN/sapphire interface) significant dislocation bending is observed, which relates to the 3D growth step used to reduce the dislocation density. However, the available data provide no evidence that these dislocations—which lie within the c-plane of GaN, and do not thread—contribute to the formation of quantum emitters.

4.1.6. Potential mechanisms behind emitter formation

As noted above, whilst the most obvious difference between the LDD and HDD GaN is the dislocation density, the 3D growth mode used to generate LDD GaN does result in unintentional incorporation of oxygen in the near interface region. Whilst the average thickness of this unintentionally doped layer is only about 1 μm, this unintentional doping might extend further into the film, in places. For the HDD GaN, where no 3D growth step is used, the unintentional doping throughout the film is low. For the ELOG sample, inclined facets which encourage the incorporation of unintentional dopants can persist for several microns, resulting in a layer of unintentionally n-doped material of significant thickness. Hence, samples with a higher incorporation of unintentional dopants, i.e., samples with a higher density of shallow donors, tend to have a lower density of point defects that can potentially act as quantum emitters. (The one exception to this is the semipolar sample, in which some emitters are seen despite a high density of unintentional doping. However, this sample is altogether atypical since the emitters are observed at the surface in

this case—while the subsurface for all the other samples—and these emitters may thus have a distinctly different origin).

Given the lack of correlation between the actual dislocation position and the emitters, but the fact that there is a correlation between the emitters and the dislocation density, one must then consider whether extrinsic impurities or point defects might be the source of the emission and then ask how the density of such impurities away from the dislocations might be affected by the dislocation density. The following considerations hint at a potential interpretation. Local variations in dislocation density affect the strain state of the film, altering bulk and/or surface diffusion coefficients. Changes to the bulk diffusion coefficient could affect the diffusion of impurities from the sapphire into the GaN film, whilst changes to the surface or bulk diffusion coefficients may affect independently the density of non-impurity point defects. Processes occurring at surfaces will also be affected by changes to the surface morphology and it was noted that HDD GaN films are rougher, with more distorted step edges than LDD or ELOG films, potentially providing more sticking sites for impurity atoms and hence altering the incorporation rate of sparse impurities from the gas phase. (The low density of emitters indicates that such impurities must exist at such a low concentration that they could not be detected by secondary ion mass spectrometry or other typical compositional analysis techniques). Additionally, it was remarked that the structure of the emitters formed by the extrinsic defects could be complex—e.g., involving atoms and vacancies—and such that the point defects could annihilate and/or not be optically active at the boundary regions formed by dislocations or the surface. All these considerations are consistent with the observation that the emitters seem to form separately from the dislocations and away from the surface.

4.1.7. Conclusions

To summarise, a systematic study was carried out on a number of GaN samples with different characteristics tailored through different synthesis conditions. The goal was to study the effect of certain specific parameters—density of the dislocations, doping with foreign atoms, structure, and orientation of the grown GaN material—on the formation of single quantum emitters. No correlation was found between stacking faults and emitters; instead, what was found was a rough— although not one-to-one—correlation between the number of emitters and the density of dislocations. However, the emitter locations and the dislocation sites are spatially distinct. Hence, it was suggested that emitters relate to an as-yet-unidentified impurity or point defect in GaN whose density is affected by the extended defect density. Future engineering of single photon sources based on GaN will thus require engineering of both the impurity and extended defect density of these materials. Nevertheless, the application of expensive bulk substrates, which tend to have low extended defect densities and a high density of unintentional n-dopants is likely to be unnecessary. Instead, efforts to engineer these devices can focus on widely available GaN epitaxial layers on sapphire. This study contributes to the growing knowledge base behind the origins of these emitters and sets forward additional studies.

4.2. Resonant excitation of quantum emitters in gallium nitride

4.2.1. Introduction

Advanced quantum nanophotonics technologies rely on the ability to resonantly excite quantum emitters to achieve Fourier transform (FT)-limited linewidths[4,16,21]. Despite progress in room temperature characterisation of defects in GaN, coherent (or resonant) excitation properties of the emitters in GaN have not been reported to date. Coherent excitation provides essential information about the emission linewidths and photophysical properties of the emitters. It is the most crucial step toward the generation of indistinguishable photons, entanglement, and realisation of coherent control of the emitters' quantum states. Here the optical properties of quantum emitters in GaN were studied at cryogenic temperatures under both coherent and incoherent excitation. The emissions have a full width at half-maximum (FWHM) of ~1.08 THz (~2 nm) under non-resonant excitation and exhibit stable emission. Resonant excitation yields nearly FT-limited lines with a FWHM of ~250 MHz.

4.2.2. Cryogenic optical characterisation of the GaN emitter

During experiments, a 4.2 μm thick low-defect-density layer of hetero-epitaxial GaN grown with no intentional doping by MOVPE on a c-plane sapphire substrate was used, synthesised using the same methods explained in Chapter 4.1. Here, the focus of characterisation was on the emitters in the visible spectral range. The experimental optical setup was similar to that shown in Chapter 4.1., with the exception of a different excitation source being a 707 nm titanium sapphire (Ti:SAP) laser, and a cryogenic chamber used to house the sample for low-temperature measurements. In the detection path, the

laser was rejected with a 715 nm long-pass filter and emissions in the spectral range of 720–900 nm was collected. All measurements during this work were performed at 10K.

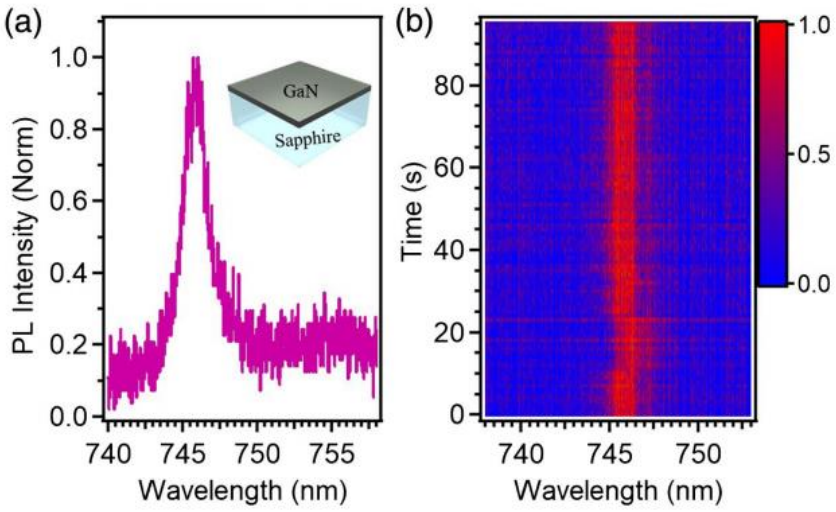

Figure 4.8. PL of emitters under non-resonant excitation. (a) A high-resolution spectrum of an emitter excited using a 300 μW, 707 nm laser. The inset shows the structure of the GaN sample: 4.2 μm of c-plane GaN grown on a sapphire substrate. (b) Successive PL spectra of the same emitter collected every second, demonstrating stable emission with negligible spectral diffusion. Reproduced from Ref.[106]

A high-resolution PL spectrum of an emitter in GaN is shown in Figure 4.8 (a). It exhibits a sharp zero phonon line (ZPL) at 746 nm with a FWHM of 2 nm. To check the emitter's stability under the same excitation conditions, successive PL spectra were measured over 90 s using a 1 s acquisition time. As shown in Figure 4.8 (b), spectral diffusion is very subtle, and the PL is stable within the time resolution of the measurement. This is highly advantageous for scalable applications of quantum emitters, where photostability is considered a prime factor for practical devices.

4.2.3. Resonant excitation of GaN emitters

Next, the coherent excitation of the emitter was performed to gain insights into the natural linewidth and broadening mechanisms of the

ZPL. Resonant photoluminescence excitation (PLE) is an optical scanning technique which involves the excitation of a luminescent defect with a sweeping range of excitation wavelengths and measuring the resultant PL. The PL itself is only produced from above-bandgap excitation, and thus can give insights of its optical mechanisms through its absorption.

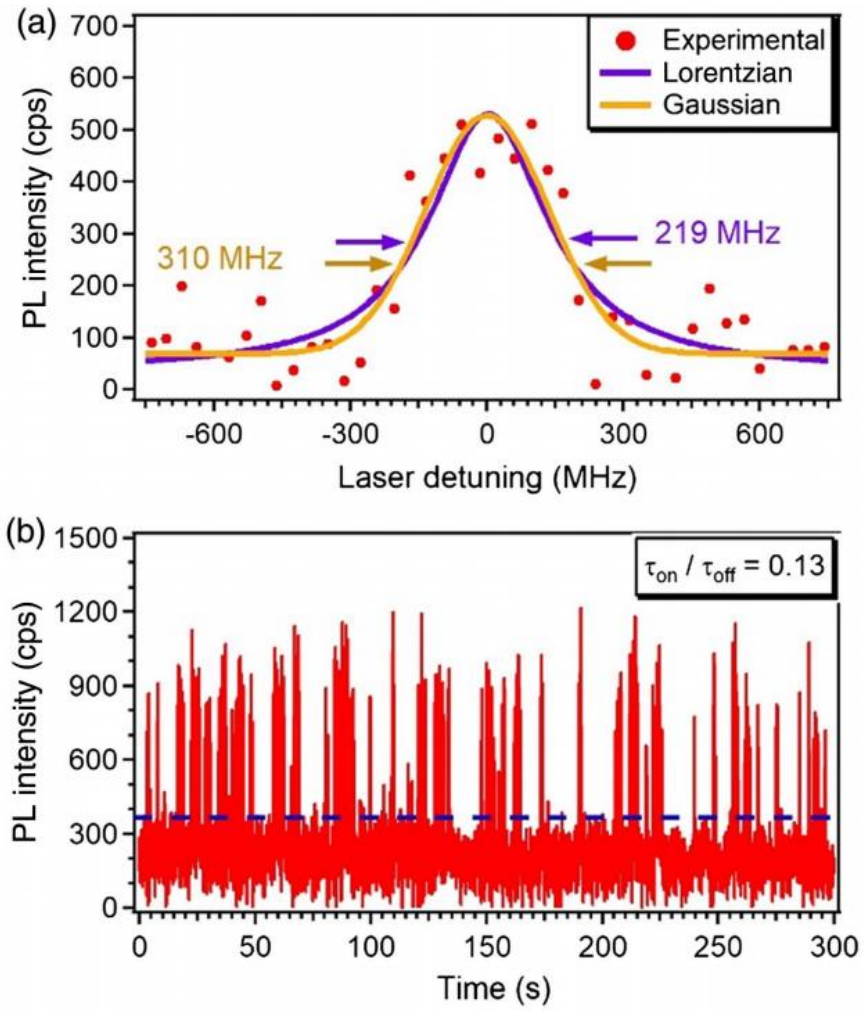

Figure 4.9. PL under coherent excitation. (a) Resonant PL excitation measurement of the emitter in Figure 4.8. The experimental data have been fitted with Gaussian (orange) and Lorentzian (violet) functions with FWHMs of 310 and 219 MHz, respectively. (b) PL emission of the emitter under fixed coherent excitation. The dashed line is the threshold used for calculating the on–off ratio of 0.13. Reproduced from Ref.[106]

The average lifetime of emitters in GaN has been reported to be 2.5 ns[21], yielding an FT-limited linewidth of ~65 MHz. For this particular emitter, a measured lifetime of ~1.1 ns was recorded, which corresponds to ~150 MHz. The same continuous-wave Ti:SAP laser (50 kHz linewidth; MSquared) was swept over 5 GHz using a step size of 20 MHz to coherently excite the emitter shown in Figure 4.8. The excitation laser was filtered with a 750 nm long-pass filter and the PL emission in the phonon sideband was collected. A resonant excitation spectrum recorded at 5 μW is shown in Figure 4.9 (a). Experimental data (red dots) were fitted with both Lorentzian (violet) and Gaussian (orange) functions with linewidths of 219 and 310 MHz, respectively. The Gaussian function yields the better fit, with χ^2 of 230, versus 305 for the Lorentzian fit. This indicates that broadening of the ZPL is likely caused by spectral diffusion rather than homogeneous broadening mechanisms such as interaction with lattice phonons[140]. Note that the room temperature spectrum is broadened due to thermally activated phonons.

The effect of spectral diffusion on emission under coherent excitation is shown in Figure 4.9 (b). For this measurement, the laser was tuned to the optical transition energy of the emitter, and the PL was acquired for 10 min. Note that in Figure 4.9 (b), the PL intensity trace is shown for 5 min to clearly illustrate the intermittency of the emission. The spectral diffusion was quantified by analysing the time-resolved PL intensity under resonant excitation. The blue dashed line shows the threshold of 400 counts/s used to define on and off times under resonant excitation. Over 10 min, the emitter was excited coherently for ~80 s (τ_{on}), and the rest of the time the emitter was off resonance due to spectral diffusion. The τ_{on}/τ_{off} ratio of 0.13 shows that the emitter is on resonance 13% of the time. Note that there was no observable power dependence of the spectral diffusion, with blinking dynamics recorded using a much lower excitation power of ~500 nW.

The spectral diffusion may occur due to charge fluctuations induced by the laser field, and can be mitigated dynamically using Stark shift tuning[141]. However, even under these conditions, given the high brightness and the high Debye–Waller factor of these emitters, one would expect more than 1×10^5 photons/s on resonance from the ZPL, which is suitable for practical devices.

4.2.4. Conclusions

In conclusion, GaN single-emitters were excited coherently and shown its potential as novel quantum systems. Near FT-limited linewidths of ~250 MHz were observed, and spectral diffusion was quantified. The results show its susceptibility to manipulation and pave the way for integrated quantum photonic circuitry based on GaN and provide important information on emerging quantum emitters in this material.

Chapter 5

Quantum emitters in diamond colour centres

Colour centres in diamond—especially group IV defects—have been advanced as a viable solid-state platform for quantum photonics and information technologies. In this chapter, the photodynamics and characteristics of germanium-vacancy (GeV) colour centres hosted in high-pressure high-temperature (HPHT) diamond nanocrystals are investigated. Through BFP imaging, the far-field radiation pattern of the investigated emitters are analysed and a cross-dipole emission strongly aligned along one axis, derived. This information in combination with lifetime measurements, allowed for the extraction of the decay rate statistics of the GeV emitters and their quantum efficiency, estimated to be $\sim(22 \pm 2)\%$. Understanding the quantum efficiency of a quantum source is a crucial figure of merit which determines its responsivity as an on-demand source of single photons. In this particular study, the results offer further insight into the photodynamic properties of the GeV centre and confirm its suitability as a desirable system for quantum technologies.

5.1. Photodynamics and quantum efficiency of germanium vacancy colour centres in diamond

5.1.1. Introduction

Discussed in Chapter 2, was the suitability of diamond colour centres, specifically group IV colour centres, as hardware for many solid-state-based quantum applications—including quantum networks, QIP, and sensing. Their structural, and resultantly optical characteristics, are responsible for the intrigue into their integration, again as discussed earlier in Chapter 2—that is, split-vacancy configuration and thus electric-field strain insensitivity.

In this work, the characterisation of GeV centre photodynamics hosted in high-pressure high-temperature (HPHT) NDs both in ensemble and single-emitter measurements were carried out. Performed, were PL and lifetime spectroscopy analyses and Fourier-plane imaging to determine the far-field radiation pattern of the emitters. These techniques were then combined to produce an approximated estimate of the quantum efficiency (QE) of an ensemble of GeV emitters. This was achieved by mapping the emitters' radiative component (k_r) of their total decay rate ($k_r + k_{nr}$) onto changes in the emitters' PL lifetime as their surrounding dielectric environment is controlled[142,143].

5.1.2. Materials and Methods

The NDs containing GeV centres were fabricated via HPHT at the Institute for High Pressure Physics, Russian Academy of Sciences, Moscow[87]. The process involved the use of naphthalene ($C_{10}H_8$) mixed with germanium, under 8 to 9 GPa of pressure and at temperatures

$>$ 1600 K, and resulted in high-quality ND crystals (size ~60 nm), containing Ge-related colour centres, including germanium-vacancy (GeV) centres.

For characterisation, NDs were dispersed on a transparent glass coverslip (22 mm × 22 mm, thickness 0.13 to 0.16 mm; Ted Pella), which had been laser scribed with a 5 × 5 unit grid consisting of 50 µm × 50 µm squares to facilitate the identification and localisation of target emitters. Optical characterisation was performed using a lab-built confocal microscope, with confocality achieved via a $4f$ lens system and a pinhole (50 µm) positioned within the collection path. Excitation of the emitters and collection of their PL signal was carried out with a 1.4 NA oil-immersion objective. Spectroscopy, lifetime, and second-order autocorrelation measurements were carried out with a spectrometer and two avalanche photodiodes (Acton SpectraPro, equipped with a PIXIS 256 camera; Princeton Instruments) and two avalanche photo diodes (Count T; Laser components) connected to a correlator (TimeTagger 20; Swabian). A 532 nm CW laser (SPL-532, Shanghai Dream Lasers Technology) was used as the primary excitation source for all optical experiments, and a 512 nm pulsed laser (PiL051-FS, Advanced Laser Diode Systems GmbH) employed for the lifetime measurements. Samples were probed in CW at an intensity measured at the back aperture of the objective of 500 µW while pulsed excitation was performed under an average power of 20 µW, with a repetition rate of 20 MHz. Fourier plane imaging was performed through an additional optical pathway utilising a $4f$ lens configuration and 0.5× magnification at the electron-multiplying CCD (EMCCD) camera (Oxford Instruments iXon Ultra 888). The size of the individual diamond nanoparticles was determined via AFM.

To fit the BFP images, first an analytical calculation was performed on the sum of two BFP intensity distributions originating from crossed linear dipoles positioned above a glass cover slide using the equations from Ref. [86]. The residues to the experimental data were minimised using the sequential least-squares programming algorithm with four free parameters: the in-plane angle (Φ) and out-of-plane (θ) of one dipole, the rotation angle of the perpendicularly oriented dipole, and the relative amplitude of the two dipoles.

5.1.3. Optical characterisation of GeV colour centres

Characterisation was performed on NDs containing either ensembles or single GeV centres. Figure 5.1 (a) is the AFM image of the investigated NDs, which are (65.0 ± 4.4) nm in diameter, and Figure 5.1 (b) shows their PL spectrum [in this case from nanodiamond 3, as labeled in Figure 5.1 (a)]. The sharp peak at ~602 nm corresponds to the ZPL emission wavelength of the GeV centre. The inset Figure 5.1 (b) displays the second-order autocorrelation measurement, $g^{(2)}(\tau)$, which was used to identify single emitters, $g^{(2)}(0) < 0.5$. For this particular emitter, the $g^{(2)}(0)$ value was measured to be (0.37 ± 0.02), evaluated with a timing jitter of 500 ps.

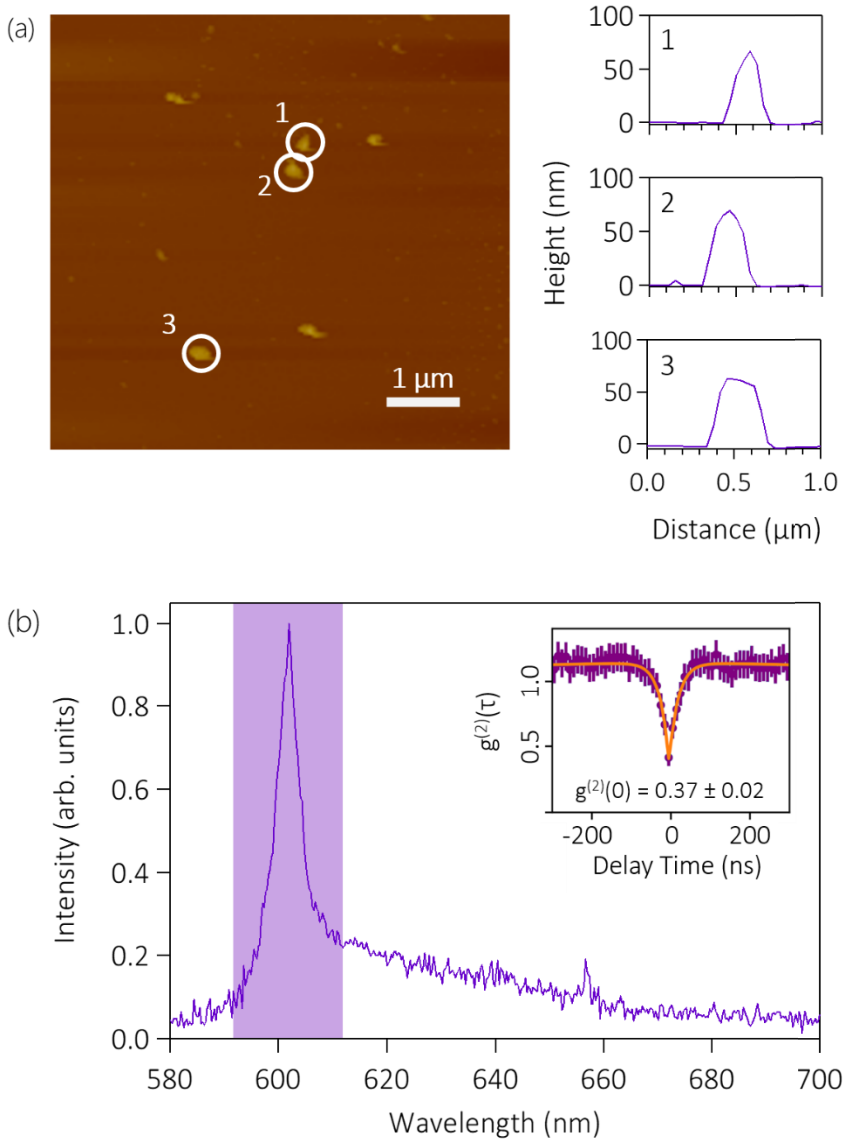

Figure 5.1. Characterisation of nanodiamonds containing single GeV defects. (a) AFM scans of three separate nanodiamonds, identified by white circles. The correspondingly numbered plots to the right show line scans from AFM, confirming their average height of approx. 65 nm. (b) Characteristic optical spectra of a single GeV defect found in nanodiamond 3 as shown in (a). Inset shows its $g^{(2)}(\tau)$ autocorrelation function, showing $g^{(2)}(\tau) = 0.37$—indicating single-photon emission. Reproduced from Ref.[37]

Analysis was then performed on the emission properties of the fluorescent NDs hosting single GeV emitters. The photoemission from individual centres is stable and reaches saturation intensities of ~10^5 to 10^6 counts/s. The single emitter in Figure 5.1 (b) is representative

of the surveyed emitters. It displays a saturation intensity $I_\infty = 7.14 \times 10^5$ counts/s—determined as $I_\infty = (I_\infty P)/(P_{Sat} + P)$ with P_{Sat} being the excitation power at saturation.

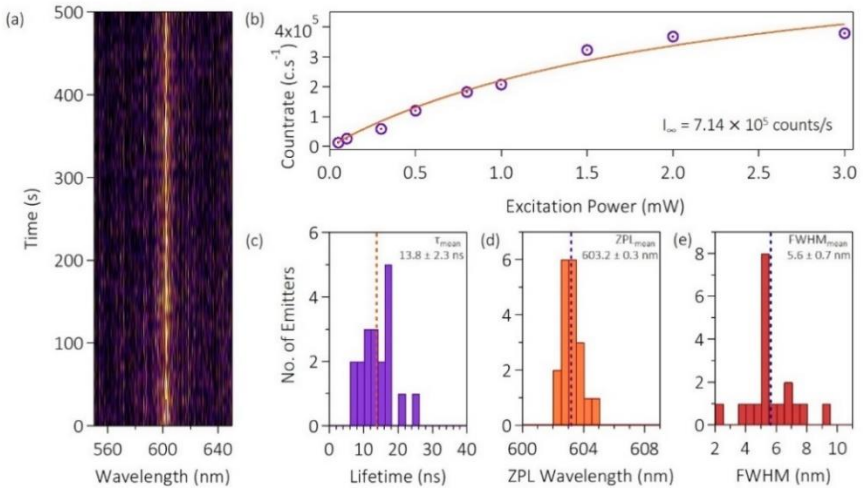

Figure 5.2. Summary of the optical properties of characteristic NDs containing GeV centres. (a) Kinetic spectra measurement of a single GeV emitter, showing photostable emission at 604 nm (FWHM ~ 4.27 nm) for 500 s at 10-s integration time intervals. (b) Saturation measurement of the emitter. The extracted saturation intensity is $I_\infty = 7.14 \times 10^5$counts/s. Histograms of the (c) emitter lifetime, (d) emitter ZPL position, and (e) FWHMs of the fitted ZPLs. The dotted lines represent the average values of their respective dataset. Each histogram represents a sample size of 18 individual emitters. Reproduced from Ref.[37]

Figure 5.2 (c) summarises the distribution of lifetimes measured for 18 individual NDs containing GeV centres; Figures 5.2 (d) and (e) show the distribution of their ZPL emission wavelength and full width at half maximum (FWHM). The measured lifetimes varies substantially among centres spanning over the range ~6 to 25 ns [Figure 5.2 (c)], with an average value of (13.8 ± 2.3) ns and consistent with previous reports[144]. The lifetime of the GeV defect in bulk diamond has been measured to be ~1.4 to 5.5 ns[18,91]. Considerably long lifetimes in NDs are expected for some colour centres, e.g. the NV centre[145]. The NV possesses a non-inversion symmetry and thus fluctuating electromagnetic fields (e.g., due to traps on the diamond

surface) may influence its lifetime significantly. On the other hand, the SiV defect in NDs exhibits very similar values of measured lifetime (~1 to 2 ns), even in NDs just a few nm in size. The fact that the GeV centre shows more variability in lifetime values than the SiV—despite sharing the same crystallographic symmetry—has been suggested to derive from its higher QE. A higher QE would make the GeV more sensitive to changes in the local photon density of states, resulting in the lifetime varying more widely from ND to ND.

5.1.4. Back-focal plane imaging of single GeV centres

A detailed analysis of the radiation pattern of GeV emitters was performed, with a Fourier imaging setup shown below in Figure 5.3. Specifically, a 4*f* optical relay system to image the BFP of the objective onto an EMCCD camera.

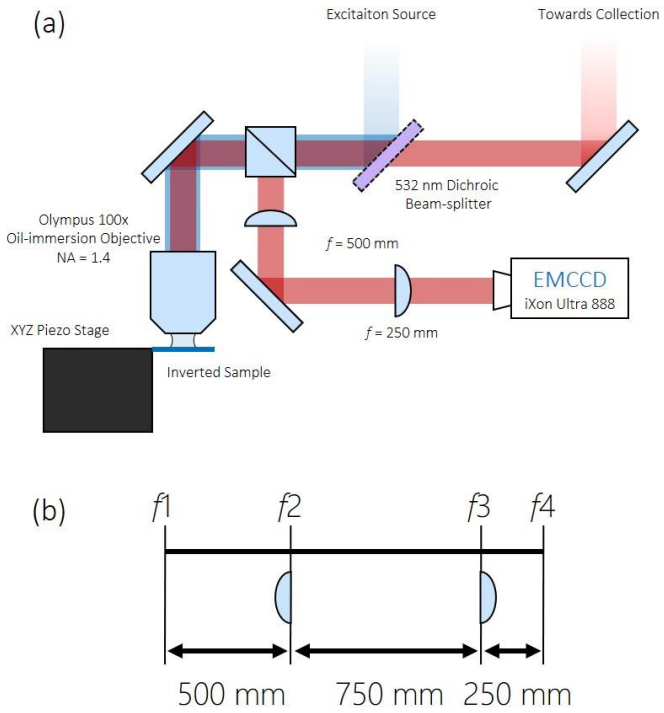

Figure 5.3. Schematic diagrams for BFP imaging. (a) Schematic of optical pathway within the confocal microscope responsible for BFP imaging. (b) Schematic illustration showing the 4*f* setup used and the lengths between each *f*.

The corresponding light intensity distribution is representative of the far-field radiation pattern of the emitter and can thus be used to map the in-plane angle (Φ) and the out-of-plane angle (θ) of the emitting dipoles in the sample plane. For each GeV colour centre, a crossed-dipole far-field radiation pattern is expected, where the dipole moment aligned along the symmetry axis of the defect is dominating[86]. This, however, has never been shown experimentally thus far. Figure 5.4 shows the experimental [Figure 5.4 (a)] and calculated [Figure 5.4 (b)] BFP radiation pattern for three typical NDs containing each a single GeV centre. The theoretical fit to the experimental BFP images highlights that the intensity distributions are consistent with the expected crossed-dipole emission, dominated by a single dipole moment. The calculated, best-fit-to-the-data values for the angles Φ and θ of the crossed dipoles embedded in the NDs are randomly distributed with respect to the glass surface, it is expected that both Φ and θ will vary from crystal to crystal. Note that before each measurement, the single photon nature of the GeV centre was confirmed using second-order autocorrelation measurements.

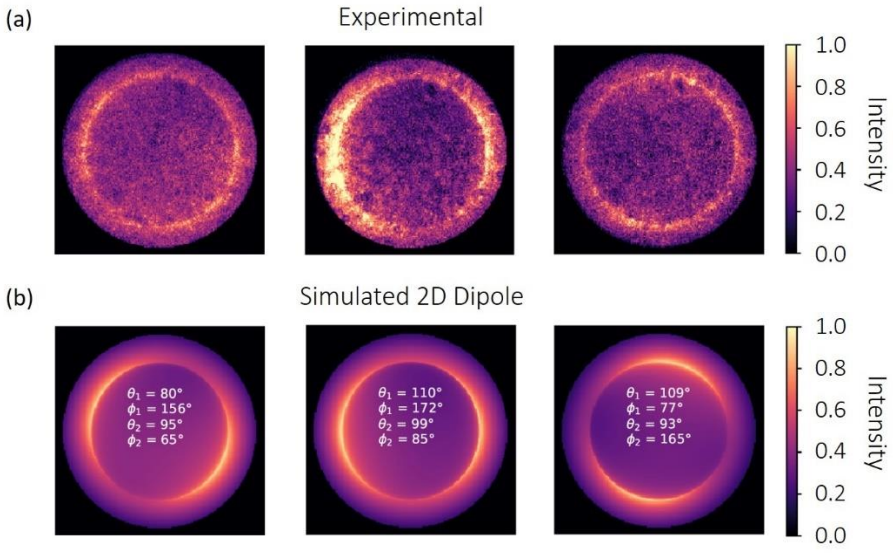

Figure 5.4. BFP analysis of three individual GeV single-photon emitters. (a) BFP images measured experimentally for each

individual emitter. (b) Corresponding simulated 2-D dipole fits. The fitted in-plane (Φ) and out-of-plane (θ) angles of the crossed dipole (subscripts 1 and 2) for each GeV centre are indicated explicitly. Reproduced from Ref.[37]

5.1.5. Calculation of quantum efficiency

Theoretically, quantum efficiency can be calculated through a set of equations which describe the total radiated power from a dipole emitting in front of a plane interface. The total radiated power P radiated by the dipole is defined as the time-average of the normal component of the energy flow density through a surface enclosing the source and can be given as $P(z_0)/P_\infty$, where $P(z_0)$ and P is the total radiated power within the first medium and second medium, respectively. The expression for the total radiated power can be broken into two separate components;

$$[P(z_0)/P_\infty]_\perp = 1 \pm 3\frac{n-1}{n+1}[(\bar{z}_0)^{-3} sin\bar{z}_0 - (\bar{z}_0)^{-2} cos\bar{z}_0 \quad \text{Eq 5.1}$$

$$[P(z_0)/P_\infty]_\parallel = \frac{1}{2}\{1 + [L(z_0)/L_\infty]_\perp\} \mp 3\frac{n-1}{n+1}[(\bar{z}_0)^{-3} sin\bar{z}_0 \quad \text{Eq 5.2}$$

Where the $\perp$ and $\parallel$ symbols represent the emission perpendicular and parallel to the interface, respectively, z_0 denotes the distance from the interface for which $\bar{z}_0 = 4\pi z_0/\lambda_1$ for power radiated by dipoles close to the surface ($z_0 \ll 1$). The upper and lower signs are valid for the electric and magnetic dipoles, respectively. From Equations 5.1 and 5.2, the total radiated power can then be expressed by

$$[P(z_0)/P_\infty] = \cos^2\theta\,[P(z_0)/P_\infty]_\perp + \sin^2\theta\,[P(z_0)/P_\infty]_\parallel \quad \text{Eq 5.3}$$

The total flux radiated can then be expressed in terms of spontaneous emission rates, and is thus given by

$$[\tau(z_0)/\tau_\infty] \quad = \quad [P(z_0)/P_\infty]^{-1} \qquad \text{Eq 5.4}$$

where τ is the lifetime of the emitting dipole.

5.1.6. Quantum efficiency of GeV colour centres

From the information taken from BFP imaging, the QE of the GeV centres were then calculated. On average, the GeV centre is brighter than the SiV, as was reported by numerous groups[85,91,92]. However, the value of the QE was never determined experimentally. The method to determine the QE relies on modifying, in a controlled manner, the electromagnetic interaction between the emitters and the surrounding dielectric environment. In general, the total decay rate (τ) of an emitter is given by the sum of its radiative (k_r) and nonradiative (k_{nr}) components, with the ratio k_r/k determining the emitter's QE. Of these decay rates, only the radiative one (k_r) depends on the local density of states (LDOS). Therefore the design of the experiment can be done such that the LDOS can be deterministically altered and the value of k_r can be extracted from the corresponding change in excited state lifetime, $\tau = 1/k$. Specifically, for an emitter in an unbounded dielectric medium of refractive index n, the transition probability k_r is governed by Fermi's golden rule $k_r \propto nk_r^0$, where k_r^0 is the decay rate in vacuum—so long as the emitter is at a distance $d > \lambda$ from any dielectric medium of refractive index n, the transition probability k_r can be determined from (and strongly depends on) the distance d, the dipole orientation (polar angle θ with respect to the normal to the interface), and the refractive indexes at the interface. Conversely, the nonradiative decay rate k_{nr} is assumed constant, regardless of d. This means that the PL lifetimes measured for the same emitter located close to ($d < \lambda$) or far from ($d \gg \lambda$) a dielectric interface should vary due solely to a

difference in the rate k_r. This ultimately allows for the determination of k_r, k_{nr}, and the emitter QE from simple lifetime measurements.

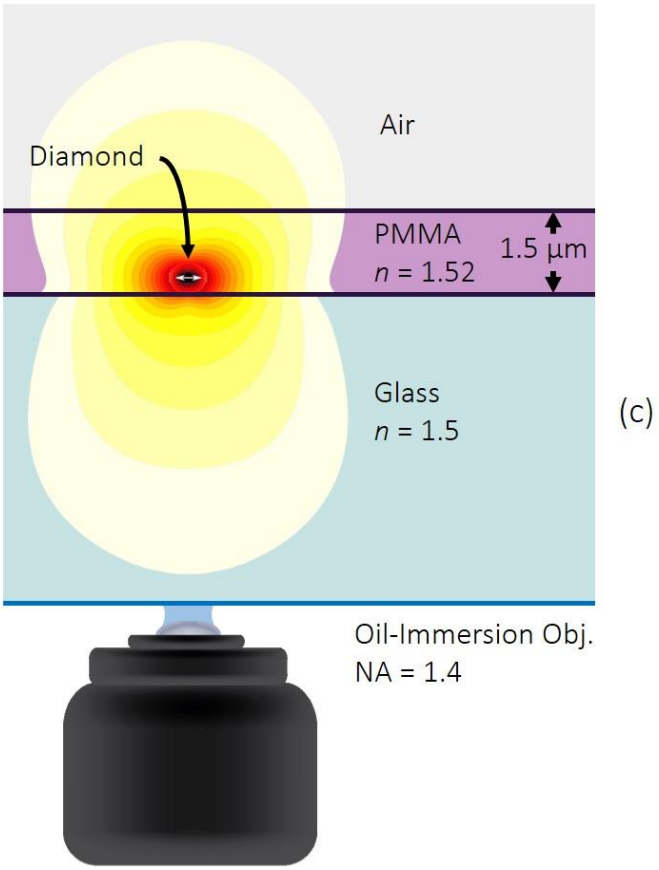

Figure 5.5. Schematic illustration of the sample and setup arrangement for the measurement of QE: in the first step of the experiment (cf. text in Chapter 5.1.2.) the NDs lie on a transparent coverslip in air; in the second step of the experiment they are covered with a 1.5-µm thick layer of PMMA acting as an unbound dielectric medium. Reproduced from Ref.[37]

Figure 5.5 shows the schematic arrangement of the performed QE measurement. For the first step of the experiment, a suspension of NDs (average size s = 65 nm) in ethanol-water solution. The suspension was dispersed on a marked glass coverslip and the lifetime of the GeV(s) in individual NDs were then measured. Figure 5.6 (a) shows the characterisation of one such ND containing an ensemble of GeV: the initial measured excited state lifetime is $\tau_1 = k_1^{-1} = (8.3 \pm 0.4)$ ns (purple trace).

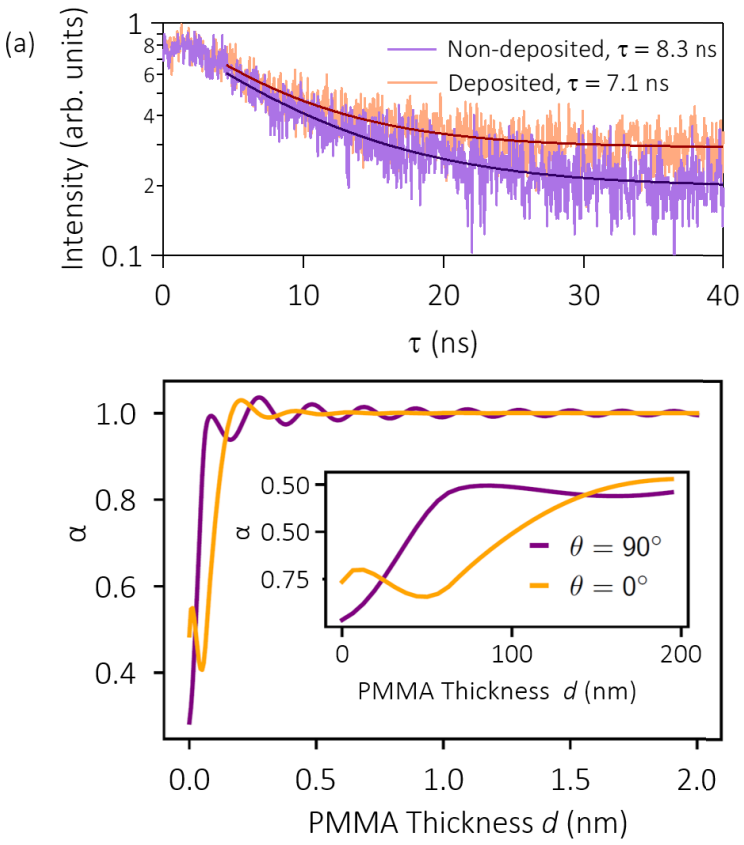

Figure 5.6. Measured QE of GeV ensembles. Top: Filtered spontaneous emission lifetime measurements before (purple trace) and after (orange trace) deposition of ~1.5 μm of PMMA. Bottom: Simulated values for the ratio between radiative rates as a function of PMMA thickness for parallel (orange trace) and perpendicular (purple trace) dipole orientations. Inset figure shows the simulated values for the range 0 to 200 nm. Reproduced from Ref.[37]

For the second step of the experiment, a thick (~1.5 μm) layer of polymethyl methacrylate (PMMA) was used as a dielectric material to surround the NDs. Since the glass and the PMMA have a similar refractive index (n_{pmma} = 1.49 and n_{glass} = 1.52), after the PMMA deposition, the NDs can be considered embedded in a homogenous medium with a refractive index $n \sim 1.5$ μm. The PMMA on top serves the purpose of 'removing' the glass-air interface, such that the NDs are effectively considered embedded in an unbounded medium with refractive index, $n = 1.5$ μm. The lifetime measurements were repeated on the same NDs surveyed in the first step, which were identified by

means of the reference laser-scribed grid on the glass substrate. Following the PMMA deposition, the measured excited state lifetime is $\tau_1 = (8.3 \pm 0.4)$ ns as measured at the previous step due to the change in the average radiative decay rate of the emitters. Defined, was the quantity $\beta = k_2^{-1}/k_1^{-1} = \tau_2/\tau_1 = (0.85 \pm 0.06)$ ns as the ratio between the overall decay rates after and before the PMMA deposition. It was noted that the measurement of the lifetime was carried out on an ensemble rather than on a single GeV centre.

Unfortunately, this hypothesis could not be directly tested, considering the following points affecting the outcome of the measurement;

(i) Diamond colour centres are not stable within ~2 nm from the surface[146]

(ii) Only colour centres ~2.5 nm from the surface might be subject to modifications occurring at the interface[147]

(iii) Assuming a uniform distribution of GeV centres in a nanodiamond that, in this case, has an average radius of 32.5 nm, geometrical considerations would determine that only ~4% of the colour centres in a nanoparticle might be affected by any physicochemical change occurring locally at the ND-PMMA interface

(iv) Only ~25% would be subject to interaction with the surface. It follows that about ~1% of the colour centres in the ensemble in each ND would experience an actual change in their nonradiative decay rate k_{nr} (and hence measured lifetime). Even ignoring the 4% error after (i)-(iii) is within the resolution of the lifetime measurement (~5%)

Nevertheless, the QE of the GeV colour centre was then calculated using JCMwave (a full vectorial maxwell solver) to calculate the ratio $\alpha = k_{r1}/k_{r2}$. This solver allows for the calculation of the power P radiated by a dipole, which is proportional to the radiative decay rate: $k_r \propto p$, and thus gives $\alpha = p_1/p_2$ Figure 5.6 shows the calculated α as the thickness of the PMMA layer varies in the range 0–1.5 μm. Note that α is determined both for the in-plane ($\theta = 90\,°$, denoted as $\alpha_{\parallel}$) and the out-of-plane ($\phi = 0\,°$, denoted as $\alpha_{\perp}$) dipole orientation. This is necessary as the lifetime measurements are carried out on ensembles of GeVs and there was thus a need to account for the random orientation of each emitter within the nanodiamond. Weighted factors were used for the out-of-plane and in-plane components, 1/3 and 2/3 respectively, and determined the isotropic value $\alpha_{iso} = 1/3\alpha_{\perp} + 2/3\alpha_{\parallel} = 0.35$. By combining the values for the ratio β and α an estimate for the quantum efficiency can be obtained[142,143].

$$\begin{aligned} QE &= k_r/k \\ &= (1-\beta)/(1-\alpha_{iso}) \\ &= 0.22 \pm 0.02 \end{aligned} \qquad \text{Eq 5.5}$$

This value for QE is approximated, as the measurement could be optimised further. Firstly, in the simulation the refractive index of diamond, $n_{\text{diam}} = 2.4$, which is higher than that of PMMA and glass ($n_{\text{glass}} \sim n_{\text{PMMA}} \sim 1.5$), is not taken into account. A complete analysis would have to consider a total of three interfaces: diamond-air, PMMA-air, and diamond-PMMA—potentially affecting the total radiative decay rate of the GeV centres. This problem could be alleviated by using, instead of glass and PMMA, a dielectric material (e.g. TiO_2) with a refractive index closer to that of diamond ($n_{TiO2} = 2.4$)—provided that the material does not mask the PL signal from the GeV emitters.

Additionally, probing a single photon emitter rather than ensembles is desirable as it would remove the approximation associated with averaging over an ensemble of emitters. This however requires the photon extraction efficiency from a single GeV centre to be high enough to be detected, practically, even after the deposition of a thick layer of dielectric material. Techniques such as bullseye cavities could in principle be employed[148]. Alternatively, it should be possible to do shallow implantation of GeVs into bulk diamond, and then consequently overgrow a thick diamond layer to meet the requirement for two different dielectric environments[149].

5.1.7. Conclusions

To conclude, the properties of the GeV centre in HPHT nanodiamonds was characterised, both in ensemble and single-emitter measurements. It was found that both the position and linewidth of the GeV ZPL emission are stable due to symmetry protection of the GeV molecular configuration. The results are compatible with previous reports of SiV and GeV centres in nanodiamonds. However, a relatively large spread of measured lifetimes (~6–25 ns) was found. This was attributed to the variability of sample-dependent differences likely related to the variance in the local photonic density of states. Back-focal plane imaging of single GeV centres was performed followed by the combining of experimental and theoretical data, allowing the reconstruction of the orientation of each centre, specifically the in-plane and out-of-plane angles of the emitting dipole(s) in the sample plane. Finally, an approximated method was discussed to measure the quantum efficiency of an ensemble of GeV centres based on simple photoluminescence lifetime measurements. It was determined that the value of the QE of the GeV to be $(22 \pm 2)\%$. It was noted that this value is an approximation and ways to obtain a more precise estimate are discussed.

Chapter 6

Quantum emitters in hexagonal boron nitride

Colour centres in hBN have been the subject of much attention, intrigue, and intense scrutiny following their newfound potential as sources for quantum applications. Favourable optical and physical properties are the reasons for its growing popularity as discussed in Chapter 2.3.2. However, studies into the true origins of its emitters are still largely ongoing. This chapter entails the work of two separate studies; the first with the aim of gaining insight into the origins of the emitters, and the second an example of its integration with additional nanophotonic constituents to manipulate its optical properties.

Chapter 6.1 explores the high-energy (~MeV) electron irradiation as a means to generate stable SPEs in hBN. Four types of hBN flakes were investigated—namely, high-purity multilayers, isotopically pure hBN, carbon-rich hBN multilayered and monolayered hBN. It was then found that electron irradiation increases emitter concentrations dramatically in all samples. Furthermore, the engineered emitters are located throughout hBN flakes (not only at flake edges or grain boundaries) and do not require activation by high-temperature annealing of the host material after electron exposure. The results provide important insights into controlled formation of hBN SPEs and may aid in identification of their crystallographic origin.

Chapter 6.2 presents the assembly of quantum nanophotonic systems with plasmonic resonators and is important for the fundamental studies of single photon sources as well as for on-chip information processing. The controllable nanoassembly of gold nanospheres with ultra-bright, narrow-band quantum emitters in 2D layered hBN are demonstrated. An AFM tip was utilised to precisely position gold nanospheres to within close proximity of the quantum emitters and the resulting emission enhancement and fluorescence lifetime reduction was observed. The extreme emitter photostability permits analysis at high excitation powers, and delineation of absorption and emission enhancement caused by the plasmonic resonators. A fluorescence enhancement of over 300% is achieved experimentally for quantum emitters in hBN, with a radiative quantum efficiency of up to 40% and a saturated count rate in excess of 5×10^6 counts/s. The results are promising for the future employment of quantum emitters in hBN for integrated nanophotonic devices and plasmonic based nanosensors.

6.1. Effects of high-energy electron irradiation on quantum emitters in hexagonal-boron nitride

6.1.1. Introduction

SPEs in hBN have so far been observed in a range of materials, including bulk crystals[150,151], mechanically exfoliated multilayers, liquid-exfoliated flakes[152,153], nanotubes, and other nanostructures[99,154]. As mentioned earlier in Chapter 2.3.4, hBN samples often require high-temperature post-growth annealing for stable emitters to be observed, and it is not clear whether the

annealing treatments create emitters or activate pre-existing defects. Recent efforts showed that plasma treatment, ion implantation, or strain can potentially be used to create/activate emitters[152,155,156]. However, emitters in hBN possess a broad range of photophysical properties, and the atomic structure of the defects is a matter of debate[105,157]. In addition, emitters in large-area mechanically exfoliated flakes are often located at grain boundaries or interfaces, and emitters in large-area monolayers are sparse[152,153,155].

In this work, the effects of high-energy (2 MeV) electron irradiation on a range of hBN samples was investigated (summarised in Table 6.1)[158–160]. The electron exposure generates SPEs, via either the generation of new defects or optical activation of existing defects, and the generated emitters were characterised using photoluminescence (PL), time-resolved measurements, and photon correlation analysis. The results suggest that the electron irradiation process can be used to engineer optically active defects without the need for high-temperature annealing and that the emitters can be located within the hBN flakes rather than just flake edges or grain boundaries. Finally it was shown that, upon MeV electron irradiation, single emitters can be created in large-area hBN monolayers—a task that has previously been elusive. The results provide important insights into controlled generation of SPEs in hBN and will aid future studies of the atomic structure of the defects.

6.1.2. Experimental Section

hBN sample preparation

Four different types of samples were prepared, and their methods are correspondingly listed as follows:

- Multilayer hBN flakes from high-purity hBN (purchased from HQ Graphene)

- Multilayer flakes from carbon-enriched hBN
- Multilayer flakes made from isotopically enriched boron-10 (99.2% ^{10}B)
- hBN monolayers (purchased from Graphene Supermarket) that were grown by chemical vapor deposition (CVD).

High-purity flakes purchased from HQ graphene were synthesised by reacting fused boric acid with urea to form $B_2O_3{\cdot}xNH_3$ and then heated further in ammonia to 900 °C. The product was further heated in a nitrogen atmosphere at 1500 °C, allowing it to crystallise on a substrate surface. The isotopically enriched ^{10}B flakes were grown with a high-purity Ni−Cr metal mix with enriched ^{10}B powder in an alumina boat at 1550 °C for 24 hours under an atmosphere of forming gas and nitrogen in a 1:4 ratio. It was subsequently cooled at a rate of 1 °C/h until 1500 °C, whereby it was quenched to room temperature. This sample is referred to as ^{10}B in during this chapter. The multilayer samples were mechanically exfoliated with scotch tape onto silicon substrates and baked at 450 °C in air to remove residual adhesives and other unwanted carbonaceous material. Monolayer hBN grown on Cu foil by CVD was cut into small squares and transferred onto Si substrates. The foils were then coated with poly(methyl methacrylate) (PMMA) to provide a platform to facilitate adhesion of the sample. The PMMA film containing the monolayer was then undercut by chemical etching of the Cu substrate with iron nitrate, leaving the polymer layer floating above. The film was transferred to a silicon substrate and heated to 120 °C for 20 min to promote adhesion, before being washed with acetone to dissociate the polymer.

MeV electron irradiation

Electron irradiation was performed with a Cockcroft-Walton 2 MV 60 kW electron accelerator at the National Institutes for Quantum and

Radiological Science and Technology, in Japan. The general operation of Cockcroft-Walton accelerators utilise electric fields for the acceleration of charged particles. A high-voltage source is used to create an electric-field gap, from which charged particles are accelerated through and towards the sample. A schematic of the electron accelerator used is shown below in Figure 6.1 (a).

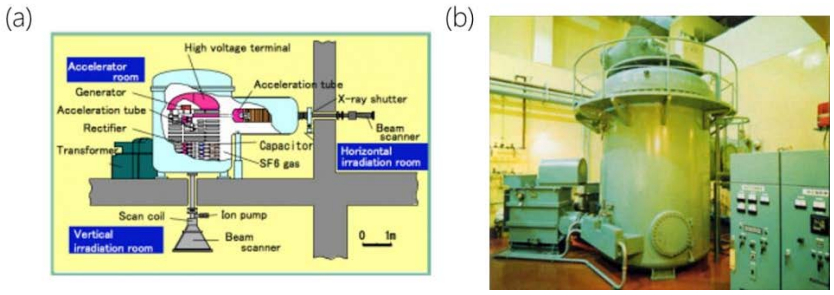

Figure 6.1. Schematic diagram of the Cockcroft-Walton electron accelerator used for the MeV irradiation. (b) External image of the accelerator. Reproduced from Ref.[161]

The samples were wrapped in Al foil and placed on a water-cooled Cu plate for the irradiation process (no temperature variation was observed). The cooling ensured that the sample temperature was kept fixed at approximately room temperature (~25 °C) during electron processing. Irradiation was performed at atmospheric conditions. The as-prepared samples were irradiated at 2 MeV with a fluence of $1 \times 10^{15}/\text{cm}^2$ for all hBN samples.

Optical characterisation

The irradiated samples were characterised using a home-built confocal PL setup with a 532 nm excitation laser. Details of the apparatus have been provided in the Appendix (Figure A.1). The autocorrelation measurements were not background-corrected. Cryogenic measurements were performed at 10 K using a Janis ST500 cryostat system integrated with a high numerical aperture objective and three-axis piezo sample positioning system.

6.1.3. Optical characterisation of hBN emitters

Figure 6.2 details PL characterisation of emitters in a high-purity, single-crystal, multilayer flake of hBN after MeV electron irradiation with and without annealing. Figure 6.2 (a) shows a confocal PL scan of a flake after electron irradiation. This flake did not contain any single luminescent centres before electron exposure. After electron irradiation, there was a high density of single luminescent emitters within the flake. A representative spectrum is shown in Figure 6.2 (b), with a ZPL ~590 nm and PSB, red-shifted by ~54 nm.

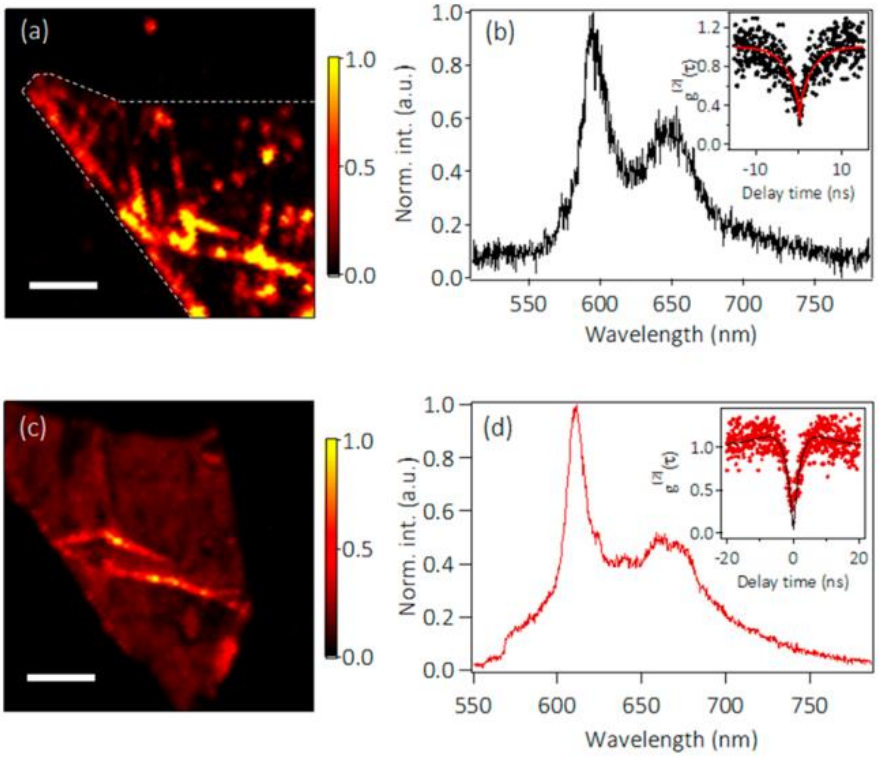

Figure 6.2. Effects of electron irradiation and on high-purity, single crystal, multilayer flakes of hBN. (a) Confocal PL map of an irradiated flake. (b) Typical PL spectrum of an emitter formed in irradiated flakes. (inset) The corresponding second-order autocorrelation function. (c) PL map of a different region of the flake obtained after high-temperature annealing. (d) Typical PL spectrum of an emitter obtained after electron irradiation and thermal annealing. (inset) The second-order autocorrelation function. Both spectra were collected at 0.3 mW for 10 s at room temperature. All scale bars are 5 μm. Reproduced from Ref.[162]

The quantum nature of the emission is confirmed by measuring the second-order autocorrelation function, $g^{(2)}(\tau)$, as shown in the inset. The dip at zero delay time, $g^{(2)}(\tau) \approx 0.26$, is indicative of a single-photon emitter. Figure 6.2 (c) shows a confocal PL scan of a different region of the same irradiated flake after an additional annealing step performed at 750 °C under 1 torr of argon for 30 min. Figure 6.2 (d) shows a representative spectrum of an emitter obtained after annealing (performed after electron irradiation). The quantum nature of the defect is once again confirmed by the $g^{(2)}(\tau)$ function [Figure 6.2 (d) inset]. Overall, the electron irradiation process created a distribution of ZPL energies, with preferential creation of luminescent defects emitting at ~600 nm when excited with a 532 nm laser. There are no substantial, systematic differences between the properties of emitters created by electron irradiation only, annealing only, or a combination of irradiation and annealing. The annealing treatment can both create and destroy emitters, as has been reported previously.

6.1.4. Spatial characterisation of hBN MeV emitters

Currently, attempts to deterministically engineer single emitters in hBN have resulted with emitters located predominantly at edges and grain boundaries[153,155,156]. In contrast, the MeV electron irradiation can produce emitters both at edges/boundaries and in the central, flat areas of flakes. This spatial characterisation of emitters is detailed in Figure 6.3. Figure 6.3 (a) shows an optical image of a large multilayered hBN flake that was subject to MeV electron irradiation. The thickness of the flake is 28.4 ± 0.4 nm as confirmed by an atomic force microscope (AFM; see inset). Confocal PL maps of the same flake reveal emitters localised within the flake [white circles in Figure 6.3 (b)]. No grain boundaries or edges are visible near the emitters. The morphology of the flake is further confirmed by a high-resolution AFM scan, as shown in Figure 6.3 (c). Figure 6.3 (d) shows a

representative spectrum from one of the formed emitters, labelled "1" on the confocal map. The inset is a corresponding second-order autocorrelation function, confirming the quantum nature of the emitter ($g^{(2)}(\tau) = 0.12$). It was noted that a subsequent annealing treatment destroyed all of the emitters shown in Figure 6.3 and generated new emitters located at flake edges and grain boundaries.

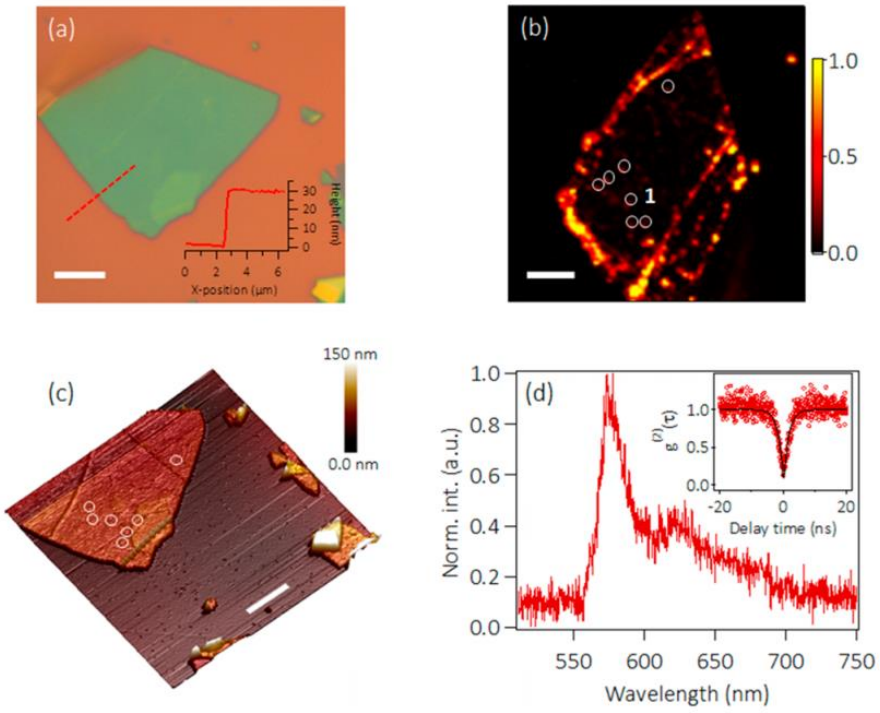

Figure 6.3. Spatial characterisation of emitters in electron-irradiated, high-purity multilayer flakes of single-crystal hBN. (a) Optical microscope image of a flake. (inset) An AFM line scan showing that the average thickness is ~30 nm. (b) Confocal PL scan showing emitters created by electron irradiation. The emitter positions are shown by white circles on the confocal map. Note, this is the same hBN flake as in (a). (c) AFM image of the same flake showing the positions of the emitters in (b) (white circles). Note that all emitters shown here are on the flat region of the flake. (d) PL spectrum of emitter 1. (inset) The corresponding $g^{(2)}(\tau)$ autocorrelation function. All scale bars are 5 μm. Reproduced from Ref.[162].

6.1.5. Effects of MeV irradiation on varying defect structure

To further investigate the effects of high-energy electron irradiation, a comparison was performed between hBN samples grown in the presence of carbon (i.e., BN doped to a C concentration of ~1×10^{19} cm^{-3}) and samples grown under standard conditions but using the ^{10}B isotope. The isotope is not important for the experiments, as there was no intention to study spin or phononic effects. However, this sample serves as a useful reference material to the high-purity hBN, since the atomic structures of the emitters and the roles of impurities are uncertain. PL spectra of emitters found in these flakes exhibit characteristics that are similar to the ones in the high-purity hBN. Figures 6.4 (a), (d) shows three PL spectra recorded from emitters in ^{10}B and carbon-doped hBN, respectively. Most of the emitters have zero phonon line energies in the range of 580−600 nm and a clear phonon sideband. The sharp edge around 565 nm is due to a bandpass filter used in our measurements. Figure 6.4 (b), (e) confirms the antibunched nature of the emitters. Only one example is shown for clarity; however, most emitters found in the samples showed antibunching. Figure 6.4 (c), (f) shows the stability curves that confirm the emission is photostable and does not exhibit blinking or bleaching (i.e., temporary or permanent intensity reduction to zero). Note that there was no annealing step involved in generating these emitters, and likewise, no emitters were found in the pristine ^{10}B and carbon-doped hBN samples.

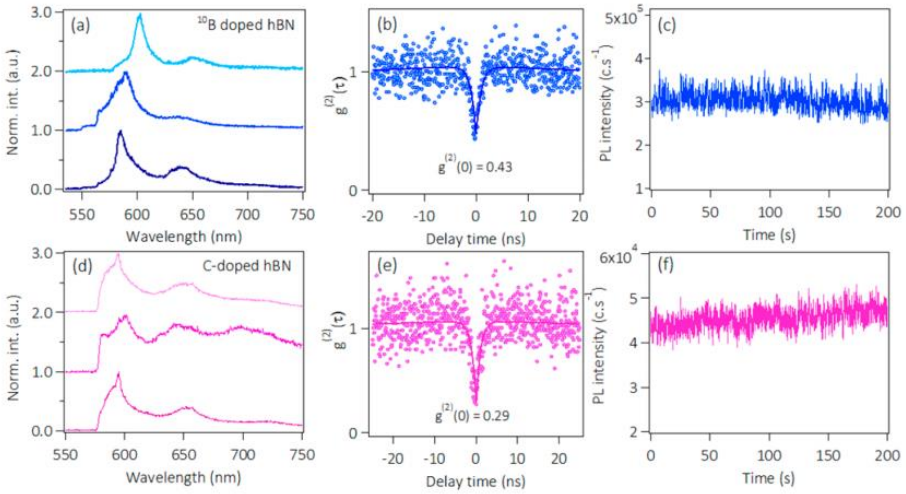

Figure 6.4. Optical characterisation of emitters in electron-irradiated ^{10}B and C-doped hBN samples. (a) Typical luminescence spectra of emitters in ^{10}B. (b) Second-order autocorrelation function of an emitter with $g^{(2)}(0) = 0.43$, indicating single-photon emission. (c) Corresponding stability curve of the aforementioned emitter. (d) Typical luminescence spectra of emitters in C-doped hBN. (e) An example of the second-order autocorrelation function of an emitter, with $g^{(2)}(0) = 0.29$. (f) Corresponding stability curve of the emitter. All optical characterisation was performed at room temperature with 532 nm continuous wave excitation. All spectra were collected at 0.2 mW for 10 s. The gradual intensity fluctuation (c, f) is due to sample drift. Reproduced from Ref.[162]

It has been suggested that carbon may play a role in these emitters. Our results do not support this assumption, as no significant, systematic differences was found between the quantity (see Table 6.1) and optical characteristics of emitters in the carbon-doped material and the other flakes investigated in this study.

Cryogenic PL measurements were performed on emitters in electron-irradiated flakes to see whether the ZPLs approach spectrometer-limited resolution and have the potential to be used for advanced quantum optics experiments[163,164]. These PL measurements were taken at 10 K using a 707 nm excitation source. Figure 6.5 (a), (b) shows two examples of ZPLs from the emitters, with a full width at half-maximum (FWHM) of 0.18 ± 0.05 nm and 0.35 ± 0.05 nm, respectively. Most of the studied emitters exhibit spectral fluctuations

on the time scale of seconds, as shown in Figure 6.4 (c), (d), respectively. These results are consistent with emitters studied in samples that were not processed by electron irradiation and in commercially available multilayers[163,165].

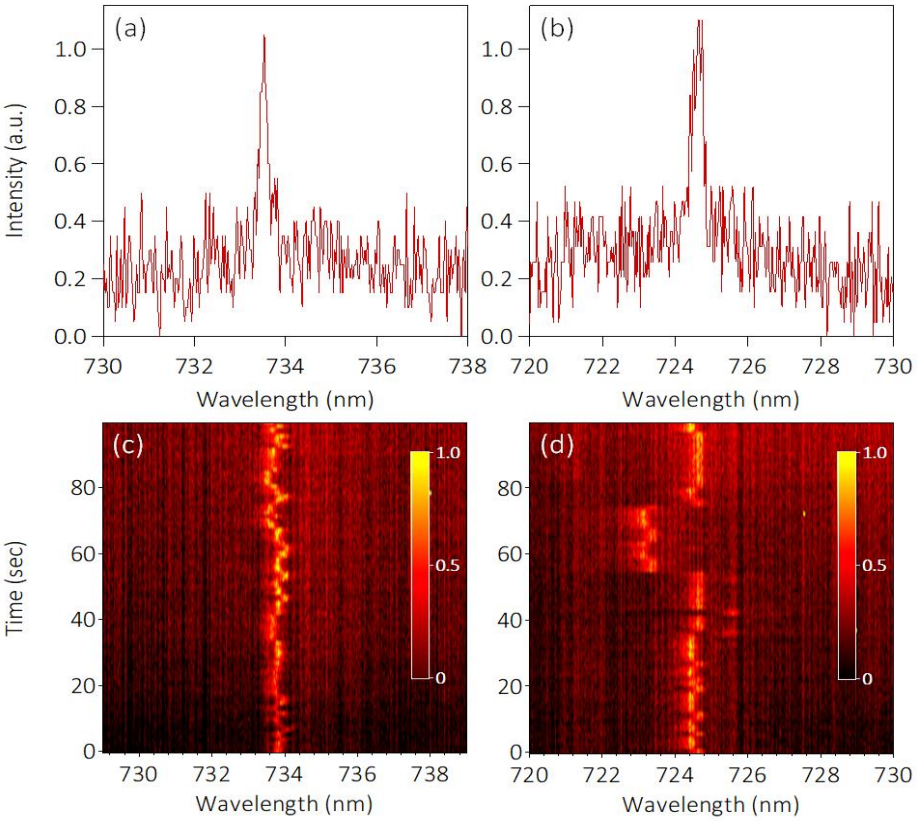

Figure 6.5. Low-temperature measurements of emitters found in electron-irradiated, high-purity, single-crystal multilayer flakes. (a, b) Typical PL spectra recorded from two SPEs. (c, d) Spectra from the same emitters measured as a function of time. The emitters exhibit spectral diffusion. All measurements were performed at 10 K. Reproduced from Ref.[162]

Finally, CVD-grown monolayers of hBN were studied. The monolayers were transferred from copper onto a silicon substrate (see experimental methods in Chapter 6.1.2). Figure 6.6 (a) shows an atomic force microscope (AFM) image with a step of ~0.79 nm corresponding to an hBN monolayer. The white spots on the monolayer are PMMA residue from the transfer process. PL scans

reveal a relatively high density of single and ensemble defects after electron irradiation (see Table 6.1). Figure 6.6 (b), (c) shows a typical example of a confocal map and a spectrum from a single emitter within the monolayers. The emitters have similar characteristics to those in large multilayered flakes in terms of their emission wavelengths, FWHM, and PSBs. Annealing for 1 h at 750 °C under 1 torr of Ar results in the formation of new emitters within the monolayers. Figure 6.6 (d, e) shows a confocal map and PL from single emitters observed in an annealed monolayer, respectively. The annealing process destroyed the previously characterised emitters while simultaneously creating new ones. In general, emitters in monolayer hBN are less stable, more susceptible to being destroyed/ deactivated by annealing, and exhibit more blinking and photobleaching under laser excitation than emitters in multilayer flakes of hBN, all likely due to a lack of encapsulation by the host material.

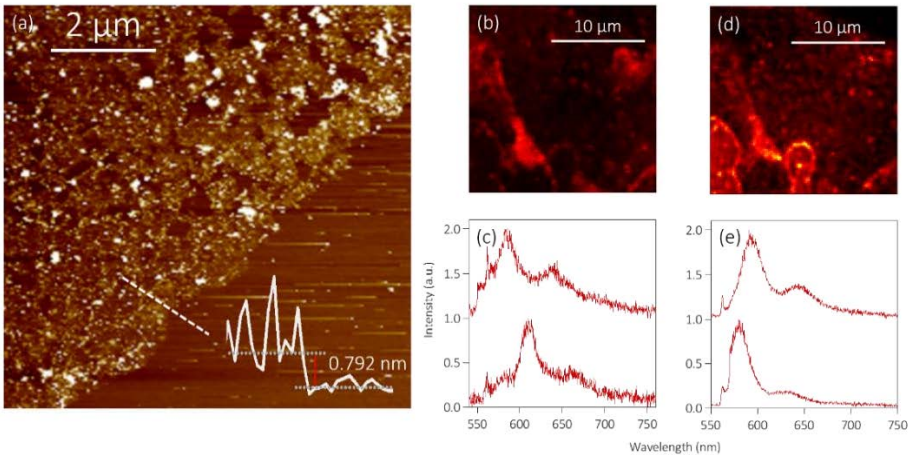

Figure 6.6. Effects of electron irradiation on hBN monolayers. (a) AFM line scan showing an average monolayer thickness of 0.79 ± 0.40 nm. (b) PL scan of an area where a hBN monolayer was deposited. (c) Typical PL spectra of emitters formed by electron irradiation. (d) PL scan of the same region of the monolayer after high-temperature annealing. (d) Typical PL spectra of emitters formed after annealing of the irradiated samples. Reproduced from Ref.[162]

Table 6.1 summarises the quantities of emitters found in all samples after MeV electron irradiation and in control samples that were not irradiated but were instead subjected to the annealing treatment (1 h at 750 °C under 1 torr of Ar). Clearly, electron irradiation is a promising method to create emitters without the need for annealing. The irradiation treatment consistently produced more emitters than the annealing process and has the potential to generate emitters away from hBN flakes edges and grain boundaries. The samples that were investigated include C-enriched hBN, and the results do not support the hypothesis that C plays a role in the atomic structure of the emitters[105]. Another important observation is that only one 'type' of emitter was observed in all of the samples, all of which were either large flakes of mechanically exfoliated multilayers or large monolayers of CVD-grown hBN. Conversely, emitters in small, liquid-exfoliated flakes of hBN (supplied by Graphene Supermarket) can be broadly classified into two groups, the second of which is characterised by longer ZPL wavelengths and weak/negligible phonon sidebands. The absence of such emitters from all samples investigated in the present study suggests that they have a different atomic structure. On a practical level, the promising high-energy electron irradiation technique presented here will likely accelerate understanding of the nature of single emitters in hBN and their deployment in devices.

Statistics of emitter formation after MeV electron Irradiation		
	MeV irradiated	**Annealed only**
High-purity hBN multilayers	~9 emitters per flake	1–2 emitters per flake
^{10}B-enriched hBN multilayers	~8 emitters per flake	1–2 emitters per flake
Carbon-enriched hBN multilayers	~5 emitters per flake	1–2 emitters per flake
CVD-grown hBN monolayers	~5 emitters per area	~3 emitters per area

Table 6.1. Overall emitter statistics across all four samples. All flakes (and areas) were chosen to have a similar size of ~20 µm, and at least five flakes of each type were scanned to generate the statistics.

6.1.6. Conclusions

To conclude, the effects of MeV electron irradiation on SPEs in hBN were studied. The results conclusively show that MeV irradiation can greatly enhance the formation of SPEs in hBN, without the necessity for a further annealing step. It was also showed that, upon irradiation, the emitters can form in the flat areas of the hBN flake. Finally, our work showed a similar distribution of emitters in carbon-rich hBN and high-purity hBN, therefore suggesting carbon may not be involved in the crystallographic structure of the defects. These results are promising to develop a reliable procedure for engineering SPEs in hBN and unveiling their crystallographic structure.

6.2. Nanoassembly of quantum emitters in hexagonal boron nitride and gold nanospheres

6.2.1. Introduction

The hybridisation of quantum emitters and photonic constituents is highly sought after to control the nature of quantum light and the realisation of integrated quantum photonic circuits[166–174]. Key requirements for these hybrid systems include robust SPEs which are bright and optically stable, as well as photonic resonators that can be readily engineered[39,40,110,111,175,176]. SPEs in layered hBN have great potential for applications such as secure communications and various quantum computing schemes thanks to their properties—as discussed previously in Chapter 2.3.4.

It is therefore interesting to further study the enhancement of these SPEs via the Purcell effect. Achieving such an enhancement, however, requires a maximal spectral overlap between the cavity resonance and the source emission as well as spatial positioning of the emitter in the maximum of the cavity electromagnetic field. Plasmonic nanoantennas are advantageous among a variety of optical resonators due to their broad spectral resonances, which make spectral matching between the optical mode and an emitter substantially less complicated[168,177–179]. The fundamental theory regarding plasmonic structures will be briefly explained further in Chapter 6.2.3. Their small mode volumes give rise to very high light confinement, resulting in correspondingly high Purcell factors. However, enhancement via these means can only be achieved at the nanoscale, requiring accurate nanoassembly methods. An AFM provides a promising solution to undertake this challenge by

virtue of its capability in manipulation of nanosized objects[166,176,180]. So far, manipulation of metallic nanoparticles towards SPEs using the AFM technique has been realised only for nanodiamonds that contain nitrogen vacancy (NV) centres. However, these emitters are broadband, with ~100 nm fullwidth at half-maximum (FWHM) and are not linearly polarised which diminishes their potential for practical applications. Other systems such as quantum dots (QDs) or single molecules offer narrower lines, but they photobleach under high excitation powers and therefore offer only moderate emission count-rates.

In this work, these issues are sidestepped by the coupling of a bright, narrowband SPE in hBN to plasmonic gold nano-spheres. Single and double-plasmonic particle arrangements were realised experimentally by placing gold nanospheres in close proximity to a precharacterised SPE in hBN using an AFM tip[181]. Coupling the SPEs to gold nanospheres modifies the spontaneous emission and enables an ultra-bright source of non-classical light. A reduced fluorescence lifetime accompanied by a photoluminescence (PL) enhancement is observed in power-dependent PL measurements. The new hybrid system constitutes one of the brightest SPEs available to date with more than 5×10^6 counts/s that operate reliably at room temperature. These results help to highlight the potential of the plasmonic enhancement of SPEs hosted by 2D layered materials for future applications in the photonic integrated chip technology.

6.2.2. Characterisation of hBN quantum emitters

The investigation is initialised with a thorough characterisation of the relevant optical and physical properties. A schematic of an optically-active defect—the antisite nitrogen vacancy ($N_B V_N$)—in a 2D hBN lattice is shown in Figure 6.7 (a).

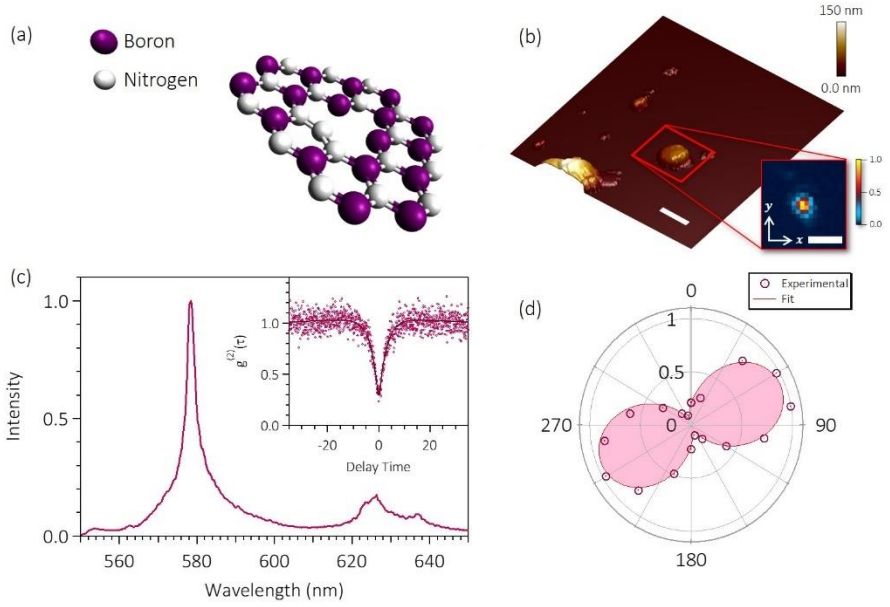

Figure 6.7. Optical characteristics of the luminescent hBN defect. (a) Schematic illustration of the nitrogen-antisite vacancy centre, N_BV_N. (b) AFM image showing the morphology of the hBN flake used for plasmonic coupling. The flake dimensions span approximately 560 nm in x and 440 nm in y, at their respective widest points. Inset: confocal PL image of the hBN SPE. The scale bar is 1 µm (c) Fluorescence spectrum of the hBN SPE. The emitter ZPL is at 578 nm with a FWHM of 2.33 ± 0.04 nm. Inset shows the second-order autocorrelation function with $g^{(2)}(0) = 0.24$, indicating single photon emission. (d) Polar graph of emission showing linearly polarised emission. The linear transition dipole is orientated at 67° with respect to the north pole of the flake with an orientation as observed in (a) All optical measurements are performed with a 532 nm laser at room temperature. Reproduced from Ref.[181]

This defect has been proposed as a likely candidate for SPEs in hBN, but remains a matter of debate in the literature (see Chapter 2.3.4). Emitters which are embedded in isolated flakes were chosen for this study. Figure 6.7 (b) shows an AFM image of a typical hBN flake with in-plane dimensions of approximately 560 nm in x and 440 nm in y, at their respective widest points. The height of the flake is similar to that of the nanosphere, with a vertical thickness of ~84 nm. This is shown below in Figure 6.8.

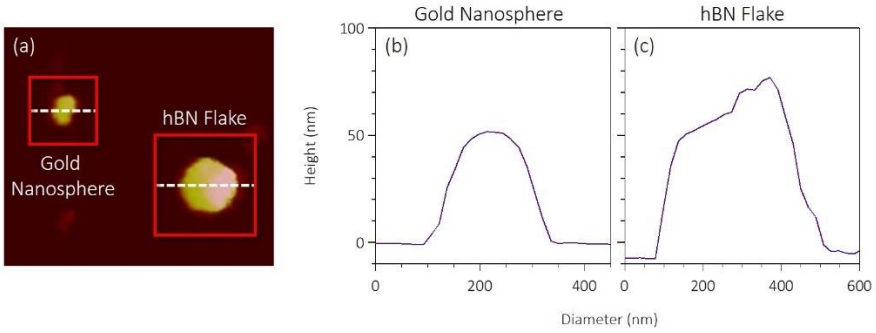

Figure 6.8. AFM characterisation of the hBN flake hosting the emitter and the gold nanosphere, it was to be coupled to. (a) AFM scan of both Au nanosphere and hBN flake. AFM line scans of both the (b) Au nanosphere, and (c) hBN flake, showing similar *z*-thickness between both nanostructures. Reproduced from Ref.[181].

The inset of Figure 6.7 (b) is a confocal PL image taken from the same flake revealing the bright emission corresponding to the N_BV_N defect. The optical characteristics of an emitter embedded in the aforementioned flake are shown in Figure 6.7 (c). A room temperature PL spectrum of the emitter reveals a sharp ZPL at 578 nm which is in the typical range for SPEs in hBN with a FWHM of (2.33 ± 0.04) nm. The PSB is also visible at 635 nm and is spectrally separated from the ZPL by over 40 nm from peak to peak. The Debye–Waller (DW) factor for this emitter is 0.75, as calculated from the ratio of ZPL emission to total emission. For the measurements throughout the manuscript, spectral filtering was performed to further isolate the ZPL and reduce transmission of the signal from other background sources with a 20 nm tuneable optical bandpass filter. The luminescence centre is shown to produce antibunched emission characterised by its second-order correlation function, exhibiting a $g^{(2)}(0)$ value of 0.24 [Figure 6.7 (c), inset)] The deviation from zero is attributed to the residual background and the detector jitter. The dip below 0.5 is a clear signature for single-photon emission. The linearly polarised emission transition dipole of the SPE was measured and fit to a cosine function, $cos^2(\theta)$, as shown in Figure 6.7 (d). The emission is linearly

polarised at an angle of 67° with respect to the y-axis. The y-axis is aligned at 0° and the x-axis is aligned at 90° [Figure 6.7 (b), inset]. The degree of polarisation, defined as $\frac{I_{max}-I_{min}}{I_{max}+I_{min}}$ (where I_{max} and I_{min} are maximum and minimum intensities, respectively), is 0.83. Such a high degree of polarisation is advantageous for applications in quantum technologies.

6.2.3. Integration with plasmonic nanostructures

The optical properties of SPSs can be drastically manipulated and enhanced through its integration with cavities[182–184]. Plasmonic cavities, in particular, have distinct advantages. Upon excitation of a metal nanostructure, the collective excitation of its surface electrons will induce the formation of either a surface plasmon polariton (SPP) or localised surface plasmon (LSP), of which confines optical modes. This confinement results in a higher local density of states within that field (LDOS), which acts as additional decay channels through which an electron can spontaneously decay through. This is the fundamental concept, behind the coupling of quantum emitters to plasmonic structures—using the emission from the SPE to resonantly drive the excitation of those plasmons, which will then result in a higher LDOS, and hence enhancing the emissive properties of the SPE, so long as the emitter itself is physically within the confines of the plasmons.

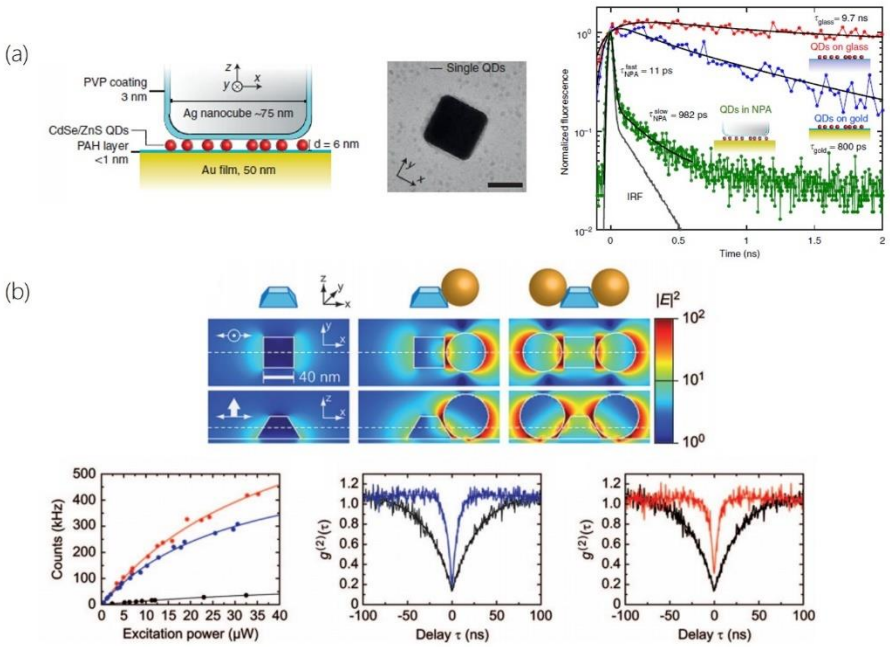

Figure 6.9. Examples of plasmonic enhancement in various configurations. (a) Particle-on-mirror configuration consisting of CdSe/ZnS QDs between a 75 nm Ag nanocube and 50 nm thick Au film. The schematic (left), TEM image (middle), and resultant lifetime reduction (right) from the configuration. (b) In-plane dimer configuration comprised of single NV colour centres in approx. 25–30 nm nanodiamonds, and two 50 nm Au nanospheres. The simulation of the configuration (top panel) shows from left to right, the uncoupled, single-particle, and double-particle arrangements. The results of the configuration (bottom panel), show saturated count rate enhancement (left), and second-order autocorrelation functions of the single (middle), and double (right) particle arrangements. Reproduced from Ref.[167,169,185]

Many studies have been performed on the coupling of various types of metal nanostructures (typically noble metals such as Au or Ag, as they provide superior absorption-cross sections for emission within the visible range), such as nanospheres and nanocubes, to emission from various sources[25,171,186–190]. Various configurations are noted, such as out-of-plane particle-on-mirror, and in-plane dimer configurations. Additionally, more complex plasmonic structures such as bullseyes and arrayed metasurfaces have also been shown to enhance emission[178,191]. Figure 6.9 shows examples of instances where plasmonic enhancement is successful—typically manifesting as a

reduction of emitter lifetime, accompanied by an enhancement in its saturated count rates.

6.2.4. Theoretical modelling of plasmonic enhancement

The theoretical fluorescence enhancement is then investigated, by positioning one and two gold nano-spheres in close proximity to the emitter using the finite difference time domain (FDTD) method. Refractive indices of the Au nanoparticles were taken from Ref.[192] The coordinate system with respect to the gold particle is shown in Figure 6.10 (a).

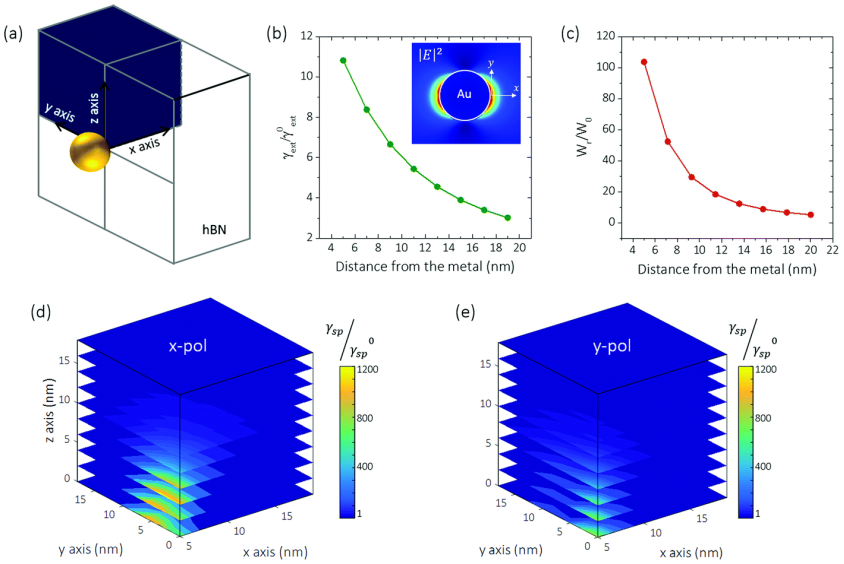

Figure 6.10. 2 FDTD simulations of the hybrid gold particle-hBN emitter system. (a) Schematic showing orientations of the axes with respect to the gold nanoparticle. (b) Excitation enhancement as a function of distance from a nanosphere surface. Inset: an FDTD simulation of the electric field intensity of a gold nanosphere excited by x-polarised light. (c) Radiated power enhancement as a function of distance between the nanosphere and the dipole emitter. 3D plot of the Purcell factor as a function of distance from the dipole emitter having (d) x-polarisation and (e) y-polarisation, respectively. The calculated region corresponds to the navy coloured region in (a). Reproduced from Ref.[181]

The fluorescence enhancement originates from both excitation enhancement ($\gamma_{exc}/\gamma_{exc}^0$) and spontaneous emission enhancement ($\gamma_{sp}/\gamma_{sp}^0$). A separate simulation of the local enhancement of the

excitation laser field was performed initially. A 532 nm plane wave with x-polarised light excites localised surface plasmons on a single gold nanosphere with a diameter of 50 nm. Note that 50 nm gold nanospheres are used both in simulation and experiments, and its absorption cross-section overlaps well with the emission spectrum of the hBN SPE, shown below with Figure 6.11. While the ZPL of the emitter does not couple on resonance with the Au NP as is the intention, it still emits within the tail of the absorption spectrum still allowing the emission to drive the plasmons on the surface.

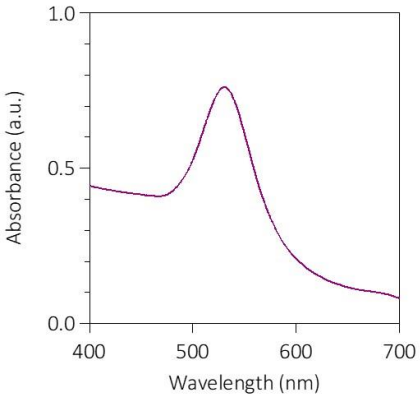

Figure 6.11. Absorption spectrum of 50 nm Au nanospheres. Reproduced from Ref.[181]

The local excitation enhancement by the gold nanosphere versus the distance from the particle is plotted in Figure 6.10 (b). Because localised plasmonic fields are most intense near the metal surface, as shown in the optical field intensity profile in the inset of Figure 6.10 (b), the local excitation enhancement decreases with increasing distance from the metal surface. Additionally, the radiative enhancement factor, defined as the power radiated into the free space in the presence of the metal sphere (W_r) divided by that in the absence of the sphere (W_0), is plotted in Figure 6.10 (c). Aside from the excitation enhancement, the radiative decay rate of the quantum emitter is also enhanced by the Purcell effect. The spontaneous

emission rate enhancement caused by a gold nanosphere (γ_{sp}) relative to the emission rate in the free space (γ_{sp}^{0}) is shown in Figure 6.10 (d) (y-polarisation) and Figure 6.10 (e) (x-polarisation). Here, the emitter dipole is assumed to have an emission peak of 580 nm, which matches the experimentally studied hBN quantum emitter. The hBN refractive index of $n_x = n_y = 1.84$ and $n_z = 1.72$ is used for the purpose of the simulation. Quantum emitters which are x-polarised and perpendicular to the metal surface show higher enhancement than those that are y-polarised. The largest theoretical Purcell factor reaches up to 1200, however, the value decreases rapidly as the distance between the emitter and the gold increases. Quantum emitters in hBN flakes are known to be in the vicinity of the flake edges, which is an advantage for plasmonic coupling. Nevertheless, determining the precise location of an emitter beyond the diffraction limit is challenging. Therefore, in this study, the goal was to manipulate one gold particle to the vicinity of the emitter first, followed by an additional gold particle in order to achieve a greater enhancement.

6.2.5. Nanoassembly with AFM

In addition to materials characterisation, the AFM has also been proven a powerful and precise tool for the nanomanipulation and assembly of integrated optical components. The operation of the AFM involves the scanning of an AFM probe across a sample surface. This AFM probe consists of a sharp tip located at the vertex of a flexible cantilever, which protrudes from a mounting plate. The tip rasters across the surface of a sample, and the resultant intermolecular interactions between the surface of the sample and the tip will then cause a deflection of the cantilever. A feedback mechanism from the detector will then adjust a piezoelectric scanner which maintains either a constant force or deflection (height) between the tip and the

sample surface. Figure 6.12 shows a schematic describing the basic working principle of an AFM.

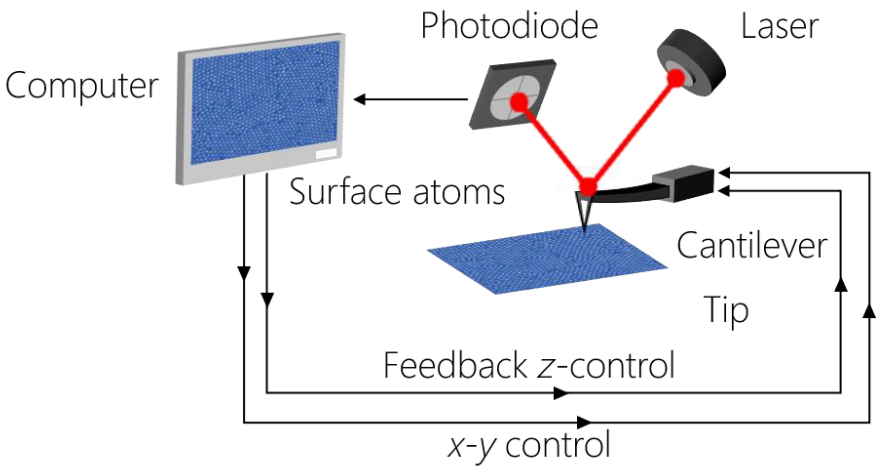

Figure 6.12. Schematic of the working principle of AFM. A tip connected to a flexible cantilever will move upon interaction with a sample surface as it performs a raster scan. A feedback system (laser) will record the effects of cantilever movement by a detector (photodiode) which will be translated to an image. The feedback system will adjust its eight accordingly from relayed information. The process repeats and an image will be produced.

To realise and delineate the absorption and emission enhancements modelled in Figure 6.11 experimentally, an AFM (Dimension 3100) was used to couple gold nanospheres to the hBN quantum emitter that was pre-characterised in Figure 6.9. Gold nanospheres were physically manipulated by a direct contact with the AFM tip and moved in small increments towards the hBN flake, as is illustrated in Figure 6.12.

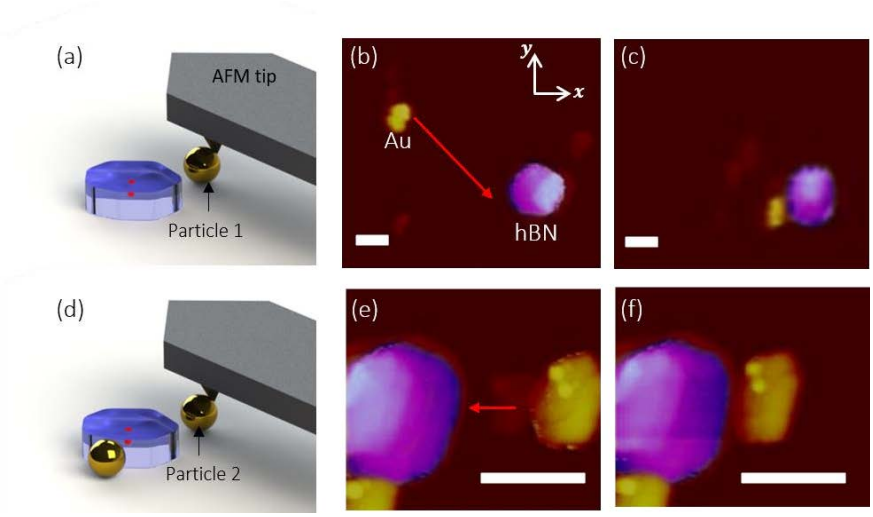

Figure 6.13. Nanomanipulation of gold spheres for plasmonic coupling using an AFM tip. (a) Schematic illustration of the movement of a gold sphere towards an SPE in hBN using an AFM tip. The movement of the gold sphere is induced by the physical contact between the tip and the particle. The luminescent defect (red) is embedded within the hBN flake (purple). (b) Initial positioning of the gold sphere in close proximity to the hBN flake hosting the SPE. The red arrow indicates the direction of movement. (c) The final arrangement of the gold sphere and the hBN nanoflake after positioning. The particle is in contact with the flake. (d) Schematic illustration of the movement of the second gold sphere to the same hBN flake. (c) The second sphere (on the right) and its movement direction shown by the red arrow. The orientation of the image has been shifted counter-clockwise [with reference from (b)–(c)] by several degrees in order to align the particle for movement towards the flake. (f) The final position of the second particle in contact with the flake. All scale bars are 250 nm. The hBN flake was false-coloured for clarity. Reproduced from Ref.[181]

Initially, a single gold nanosphere is moved into the position to couple a plasmonic cavity with the SPE embedded within the flake [Figure 6.13 (b) and (c)]. This particular arrangement is denoted as the 'single particle' configuration. A second gold sphere was then manipulated to the hBN flake in a similar fashion [Figure 6.13 (d–f)]. Similar to the 'single particle' configuration, the movement of the second particle into the position with the AFM can be seen in Figure 6.13 (d–f). The resulting arrangement was referred to as the 'double particle' configuration. The second nanosphere is moved to align with the

transition dipole angle as shown in Figure 6.9 (d) in order to maximise the plasmonic coupling effect as predicted with the simulation results in Figure 6.10. This transition dipole angle was deduced from the orientation of the flake relative to nearby reference markers. It was also noted that despite the second particle not completely aligning with the first particle, it is still positioned within the maximum emission field when cross-referenced from both the AFM image and the polarisation measurement

6.2.6. Characterisation of Purcell enhancement

Next was the detailed optical characterisation of each configuration (pristine SPE, "single" and "double" particle) using a lab-built confocal microscope and a HBT interferometer setup (see Appendix Figure A.1). Time-resolved PL from this hBN SPE shows a reduction in emission lifetime from $\tau_{pristine} = 4.92$ ns to $\tau_{single} = 2.68$ ns, for the single-particle arrangement, and consequently, a further emission decay to $\tau_{double} = 1.54$ ns for the double-particle arrangement. The data are plotted in Figure 6.13 (a) and (b), showing spontaneous emission rate enhancement factors of 1.84 and 3.19 for the single and double-particle arrangements, respectively. The decrease in emission lifetime is attributed to the confinement of the electric field, which results in an increase in the local density of states. Double-exponential functions are used to fit the lifetime data, where the first exponent accounts for the background and the instrument response time, and the second exponent corresponds to the emitter lifetime. Note that a distribution of lifetimes was not expected in this case, as reported by Akselrod et. al.[170], since only a single quantum emitter was probed rather than an ensemble.

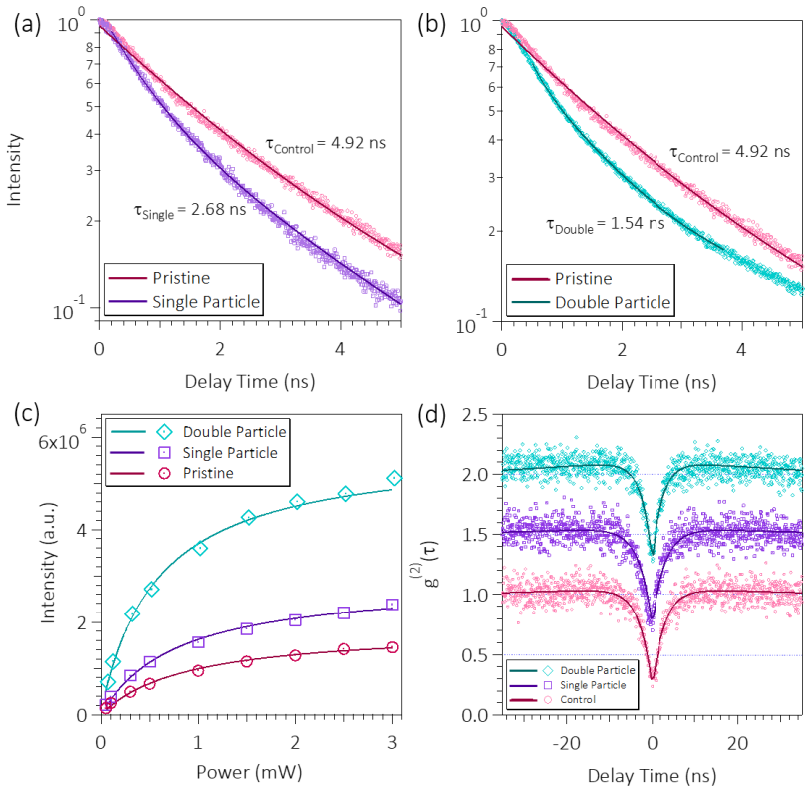

Figure 6.14. Characterisation of the optical response from plasmonic coupling. Data from a pristine emitter, a single particle arrangement, and a double particle arrangement are shown in pink, purple and teal, respectively. (a) A comparison between time-resolved PL measurements of pristine and single particle configurations, and (b) double particle arrangement. (c) A comparison of fluorescence saturation curves between the pristine, single particle, and double particle arrangements. (d) Second-order autocorrelation functions for the three configurations. All $g^{(2)}(0)$ values are below 0.5, confirming single photon emission. All measurements were recorded at room temperature. Reproduced from Ref.[181]

The measured lifetime is comprised of the radiative and non-radiative components: $1/\tau_{tot} = 1/\tau_r + 1/\tau_{nr}$. Therefore, to confirm that the lifetime reduction seen in Figure 6.14 (a) and (b) is caused primarily by an increase in the efficiency of radiative decay channels, the saturation intensities were determined from the PL versus laser power curves shown in Figure 6.14 (c). Background emission from stray light during the experiment is evident throughout the measurement, but is of negligible effect for this measurement, as saturated count rates are

several orders of magnitude higher than the measured background. The saturation measurements were then fitted with the following equation:

$$I = \frac{I_\infty P}{(P_{Sat} + P)} \quad \text{Eq 6.1}$$

where I_∞ is the saturated count rate and P_{Sat} is the saturation power. The saturated count rates are 2.89 × 10^6 counts/s and 5.79 × 10^6 counts/s for the single- and double-particle arrangements, respectively. This translates to overall enhancement factors of 1.55 and 3.10 relative to the uncoupled, pristine hBN emitter which exhibits a saturated intensity of 1.87 × 10^6 counts/s. A comparison of the measured decay rate enhancement with the saturated intensity enhancement reveals that the latter originates primarily from the enhancement of the radiative decay channel. Remarkably, the hybrid quantum plasmonic system generates almost ∼6 × 10^6 counts/s, representing one of the brightest room temperature SPEs in a layered material reported to date, associated with a modest Purcell enhancement of three. Other room temperature SPEs that exhibited more than a million counts/s under ambient conditions using an air objective include the silicon vacancy (SiV) defect in diamonds[83] and pristine hBN flakes that reach ∼3 × 10^6 counts/s[193].

To confirm that the quantum nature of the emitter is preserved, the second-order autocorrelation function, $g^{(2)}(\tau)$, was compared for the three configurations. Figure 6.13 (d) shows the plots of the $g^{(2)}(\tau)$, offset vertically by 0.5 for clarity. The $g^{(2)}(0)$ value across the three datasets is consistent with minimal changes within the uncertainty of the measurements, with values of $g^{(2)}(0) = 0.24$, $g^{(2)}(0) = 0.26$, $g^{(2)}(0) = 0.31$ for the pristine, single, and double particle arrangements, respectively. Similarly, this measurement also features background emission, again from stray light as well as a combination of detector

timing jitter and the instrument response function (IRF) of the system. Should the $g^{(2)}(\tau)$ function be convoluted, taking into account the IRF, as well as detector jitter, the $g^{(2)}(0)$ will have been a further reduced value than was measured, as values such as APD dead times will no longer contribute to the correlative data. In this case, due to the very short lifetimes and the finite time response of the system jitter, the reduction in lifetime is not evident in the $g^{(2)}(\tau)$ functions and hence were not applied during the measurement. For further analysis of the hybrid system, PL enhancement in the un-saturated regime can be approximated by the following term:

$$EF \quad \propto \quad \eta \times \gamma_{exc} \times QE \qquad \text{Eq 6.2}$$

where η is the collection efficiency, γ_{exc} is the excitation rate, and QE is the quantum efficiency of the emitter in the coupled system[170]. For the studied configurations, changes in collection efficiency were expected to be negligible with a high NA objective lens (NA = 0.9) for the pristine and the coupled emitter configurations[168]. Below the saturation threshold, the net enhancement has an excitation contribution caused by strong localisation of fields around the metal nanosphere which serves to increase the absorption of the excitation laser by the coupled system. This typically manifests an increase in the slope of the saturation curve[172]. It was noted that emitter count rates measured beneath saturation, at 300 μW, are higher than the saturated enhancement factors with enhancement factors of 1.69 for the single particle and 4.18 for the double particle arrangements. This difference was attributed to increasing excitation enhancement onset by an increased absorption cross-section upon the introduction of the nanospheres. It was also noted that the power, at which the system begins to saturate, decreases with the second nanosphere addition. Measurements show saturated power values of 0.88 mW, 0.78 mW, and 0.57 mW for the pristine, single particle, and double particle

arrangements, respectively, supporting the claim mentioned. On the other hand, above the saturation threshold, the emission is proportional to the radiative lifetime;

$$EF_{\infty} \quad \propto \quad \eta \times \gamma_r \times QE \qquad \text{Eq 6.3}$$

For the case of the double sphere, $\tau_{double} = 1.54\,ns$, $P_{Sat} \sim 5.79 \times 10^6$ counts/s and the setup efficiency (from objective lens to the detector) of our experimental setup is estimated at ~2%, yielding a high radiative quantum efficiency of ~40%.

6.2.7. Conclusions

In summary, the coupling of SPEs in layered hBN to plasmonic gold nanospheres were successfully demonstrated. The accurate nanoscale manipulation of the gold nanospheres by an AFM tip was used to realise two hybrid coupled systems comprised of a quantum emitter in hBN, and one and two gold nanoparticles. An emission enhancement associated with a lifetime reduction was observed, yielding an impressive overall count rate from a single emitter of more than 5×10^6 counts/s at room temperature. The presented technique can be applied to a range of hybrid plasmonic–photonic systems for studying other 2D materials, such as transition metal dichalcogenides[194,195], and exfoliated hBN monolayers. One particular goal is to engineer the emitters deterministically at the tip of a triangular shaped flake. This can in principle be achieved by growing high quality hBN that has a triangular structure and then locally forming the emitters using electron or ion beam irradiation. The two gold spheres can then be manipulated to create a horizontal gap cavity, and achieve an optimum enhancement. Such a procedure in emitter positioning, assembly and improvements in collection efficiency are expected to yield even higher count rates, which will be very attractive for practical devices.

Chapter 7

Contributed works

As Chapters 4 through to 6 recount the four first-author papers undertaken during the Ph.D. program, this chapter recounts the publications performed in collaboration with colleagues from other research groups. These projects, again, revolve around the two main objectives of this thesis—understanding the creation of solid-state quantum emitters, and how they interact with their surrounding environments upon integration. During this chapter, the primary authors of their corresponding publications can be identified with the (†) symbol.

7.1. Contributed works on the creation of hBN emitters

7.1.1. Revealing multiple classes of stable quantum emitters in hexagonal boron nitride with correlated optical and electron microscopy

Fariah Hayee†, Leo Yu, Jingyuan Linda Zhang, Christopher J. Ciccarino, Minh Nguyen, Ann F. Marshall, Igor Aharonovich, Jelena Vučković, Prineha Narang, Tony F. Heinz, Jennifer A. Dionne
Nature Materials 19, 534-539 (2020)

During this study, the direct correlation between quantum emission from hBN and localized strain was drawn, through a combination of PL, CL, and nanobeam electron diffraction measurements[196]. The study was performed on a sample size of 40 emitters, observing ZPLs in both PL, and CL ranging between 540 to 720 nm.

Figure 7.1 shows the correlated optical and electron-beam characterisation of hBN quantum emitters. A CL-TEM setup was used to identify emitters through high-angle annular dark-field (HAADF) imaging paired with panchromatic-CL measurements. Additionally coupled to this system is a HBT interferometer as well, to measure quantum emission. Spectra from single emitters were recorded from specific regions [Figure 7.1 (d)], and their emission characterised in PL, and CL were compared [Figure 7.1 (f)]. Additional studies of other emitting centres shows a total of four distinct types of defects, classified based on the properties of ZPL energy and range, strain, and finally CL-PL correlation. The results of these are shown in Table 7.1.

Class	**ZPL centroid (nm)**	**PL and physical characteristics**
1	580	• Matched PL-CL spectra • Large strain variation
2	615	• Shifted PL-CL spectra (100 meV) • Negligible strain variation
3	705	• Shifted PL-CL spectra (200meV) • Minimal strain variation
4	660	• No observable CL signature (either no quantum efficiency or >450 meV shift) • Non characterizable strain variation

Table 7.1. Summary of results from PL-CL study.

By analysing and correlating these properties, the study serves to provide further expand the understanding into what affects the properties of these emitters.

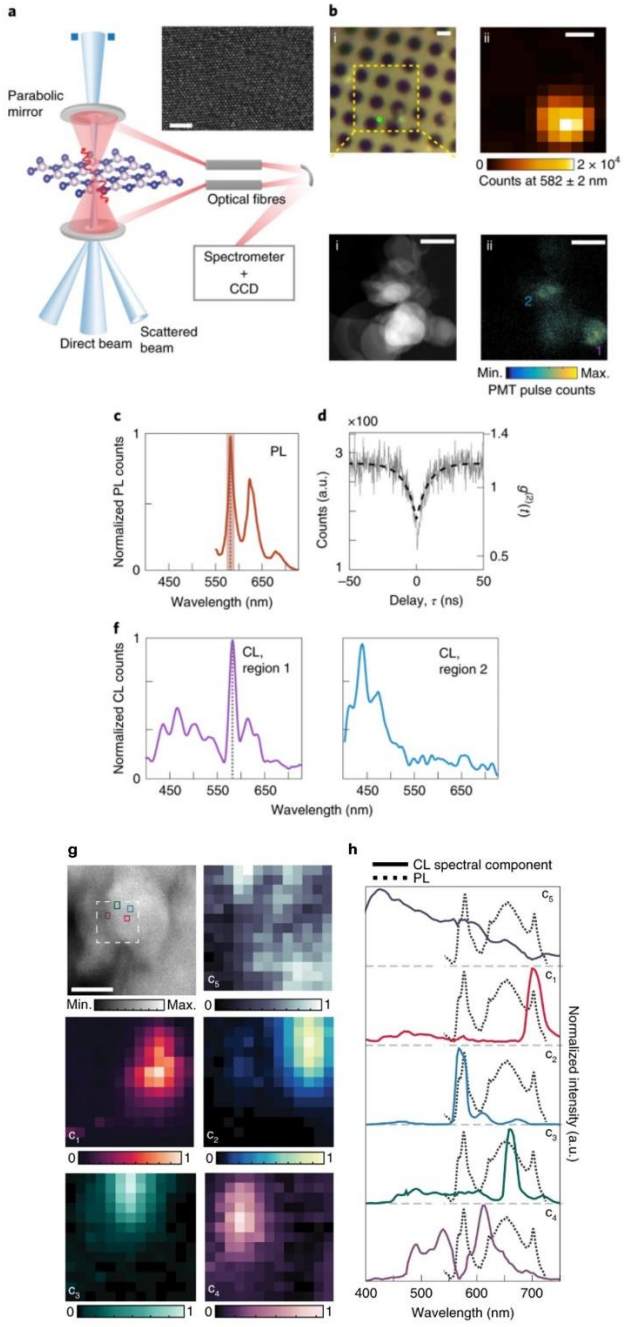

Figure 7.1. Summary of results. (a) Schematic illustration of the CL-TEM setup used for characterisation. (b) Various optical (i), PL (ii), and CL (iii, iv) of characterised flakes hosting quantum emitters, with specified regions, 1 and 2. (c) PL spectra, with region showing the filtered emission sent towards the detectors for (d) second-order autocorrelation measurements. (f) The same emitter

shown in (c), as excited in PL from region 1 and 2. (g) STEM-HAADF images of region 1, showing the regions of highest intensity indicated by the boxes, as well as their corresponding higher magnification image. (h) Corresponding spectra measured from those boxes. Reproduced from Ref.[196]

7.1.2. Single photon emission from plasma treated hexagonal boron nitride

Zai-Quan Xu†, Christopher Elbadawi, Toan Trong Tran, Mehran Kininia, Xiuling Li, Daobin Liu, Timothy B Hoffman, Minh Nguyen, Sejeong Kim, James H Edgar, Xiaojun Wu, Li Song, Sajid Ali, Mike Ford, Igor Aharonovich
Nanoscale, 10(17), 7957-7965, (2018)

Among the fabrication techniques employed to create hBN emitters, plasma treatment can be utilised with great effect to activate single defects in the material. This particular study investigates the effects of plasma treatment combined with thermal annealing as a method to produce single emitters of hBN, in a high density, and is the first instance of such[99]. A two-step process fabrication process involving thermal annealing and plasma irradiation of Ar and O_2 was performed on tape-exfoliated hBN single-crystal flakes.

First, the flakes were annealed at 850 °C, activating emitters, to show that the following plasma irradiation method is the dominant process responsible for emitter generation in high volume. Figure 7.2 (a) and (b) show confocal scans of an annealed target flake before and after plasma treatment, showing a clear increase in the amount of emitters generated. The optical properties of these emitters are characteristic of hBN emitters, showing sharp ZPLs, and single emitters with average lifetimes around 2.4 ns [Figure 7.2 (c), (d), and (e)]. Following this plasma treatment, an additional thermal annealing step was also performed in order to stabilise the emitters [Figure 7.2 (f)]. It was also noted that these emitters appeared only on the grain boundary.

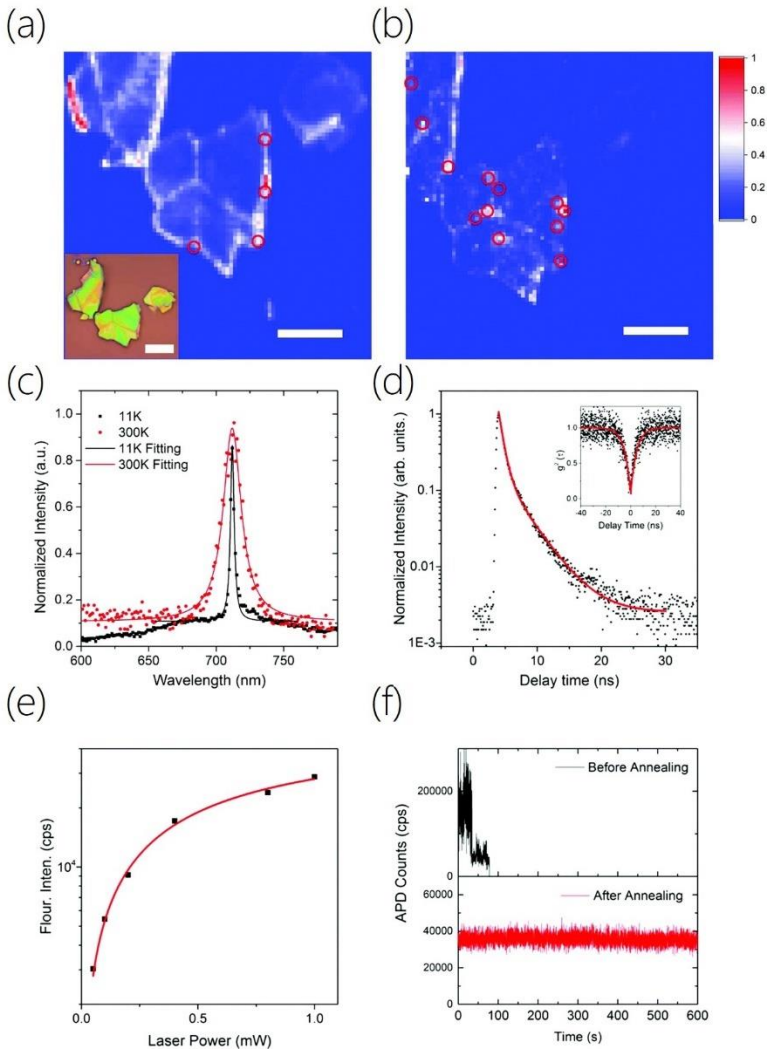

Figure 7.2. Characterisation of plasma-activated hBN single emitters. Confocal scans of annealed flakes (a) before, and (b) after plasma annealing. (c) Spectrum of an emitter at room temperature (red) and at cryogenic temperatures (black). (d) Lifetime measurement of a single emitter, with its $g^{(2)}(\tau)$ autocorrelation function inset. (e) Saturated countrate measurement of the same single emitter in (d). (f) Stability of the hBN emitters before (top) and after (red) annealing. Reproduced from Ref.[99]

The study serves to give further insights into the origins of the emitters, through the interactions between the oxygen plasma and hBN and variations of the annealing stages. From the results, it is hypothesised that the accelerated ions from the plasma process are capable of breaking N-B bonds, and thus creating N vacancies in the hBN lattice. Once generated, these vacancies are expected to be filled

with O atoms upon exposure to air—strongly suggesting that oxygen plays a role in the emitting defects.

7.1.3. Facile assembly of hexagonal boron nitride nanoparticles by cryogenic exfoliation

Ngoc My Hanh Duong†, Evgenii Glushkov, Andrey Chernev, Vytautas Navikas, Jean Comtet, Minh Anh Phan Nguyen, Milos Toth, Aleksandra Radenovic, Toan Trong Tran, and Igor Aharonovich
Nanoletters, 19(8), 5417-5422, (2019)

Combining the optical properties of hBN solid-state emitters with the extended applications of nanoparticles to realise applications in imaging, sensing, and drug-delivery was the main driving force behind this project. In this study, hBN nanoparticles were produced via a scalable cryogenic exfoliation technique resulting in the synthesis of particles below 10 nm[197]. Commercially purchased hBN powder underwent a cryogenic exfoliation technique involving its soaking in liquid nitrogen for one hour, before immediately dispersing into a room-temperature solvent (water:IPA in a 1:1 ratio) [Figure 7.3 (a)]. This results of the rapid change in temperature results in peeling-off of the hBN flakes and formation of small cracks in the intralayer, facilitating the breakdown of hBN powder into small nanoparticles [Figure 7.3 (b)]. The different sizes of the nanoparticles created could be separated from one another into three size class via differing membrane filters and centrifuge speeds. Figure 7.3 (c) shows the size distributions as a result of the separation process in AFM, with average size distributions of 119.5 ± 46.0, 20.5 ± 10.6, and 5.14 ± 1.40 nm for samples S1, S2, and S3, respectively.

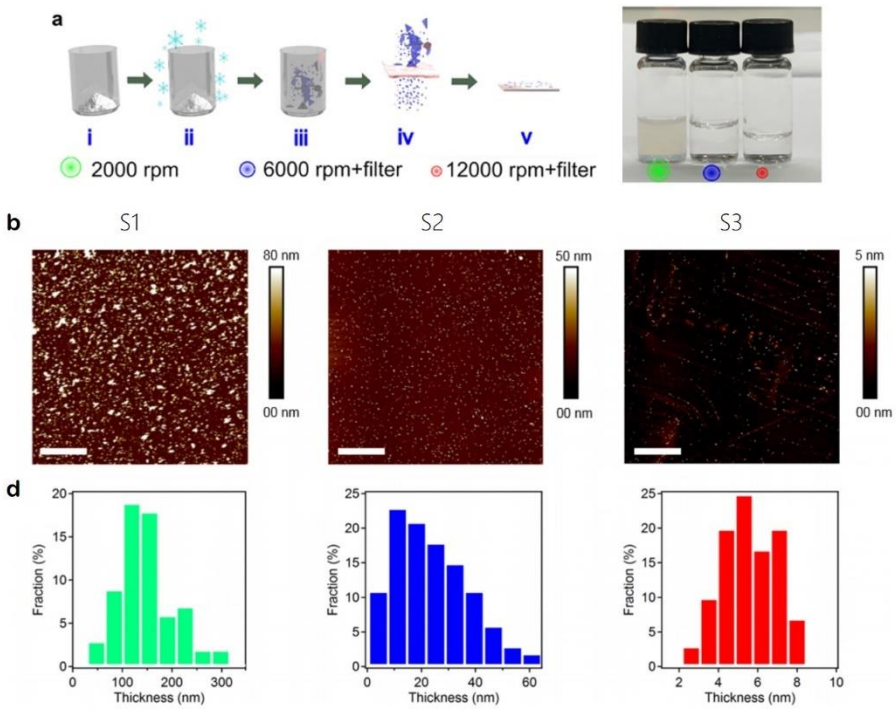

Figure 7.3. hBN nanoparticles. (a) Schematic showing the cryogenic exfoliation process for hBN powder into nanoparticles. (b) AFM images of the nanoparticles as separated into three classes based on size. They are labelled S1, S2, and S3. (c) Statistics regarding the size distribution of their respective class. Reproduced from Ref.[197]

The optical properties of these hBN flakes containing single emitters was then performed, showing the existence of single emitters across all three classes. Additionally, a study on its blinking characteristics as a function of particle size was also performed, recording on-off times through the use of wide-field imaging and single-molecule localisation microscopy (SMLM) (Figure 7.3). There was no observed correlation between particle size and blinking, as there was no significant difference between the three samples.

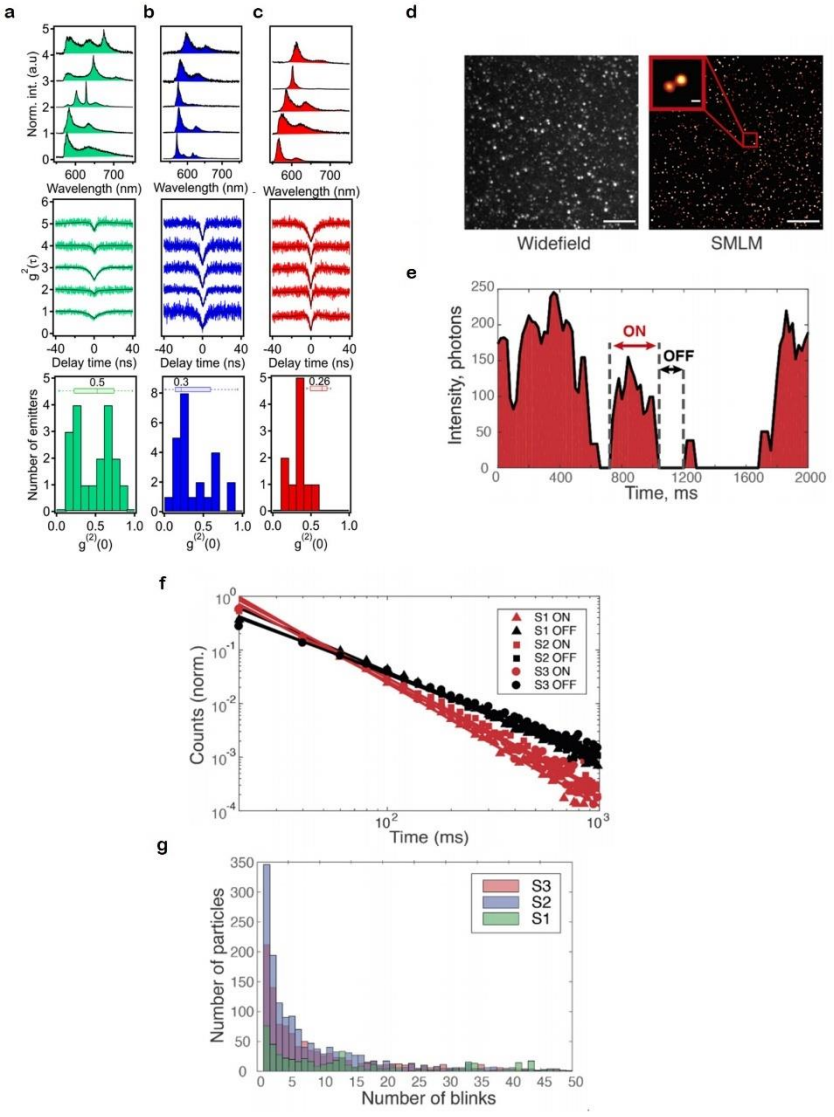

Figure 7.4. Optical characterisation of the hBN emitters. Optical properties of emitters as taken from the three classes (a) S1, (b) S2, and (c) S3. The characterisation comprises of spectra (top), $g^{(2)}(\tau)$ autocorrelation function (middle), and histograms of antibunching dip values as extracted from samples from their respective class (bottom). (d) Widefield fluorescence imaging and SMLM from sample S2. (e) Time trace of a localised emitter, showing an example of the detected ON and OFF times. (f) Normalised distribution of ON/OFF times for the localised emitters, calculated form the analysis of the time traces, shown in (e). (g) Histogram of the frequency of transitions from OFF to ON states and *vice versa* per emitter. Reproduced from Ref.

The results of this work demonstrate the fabrication of hBN nanoparticles as small as 3.0 ± 0.7 nm, capable of hosting point defects which act as photostable single photon emitters. SMLM studies

revealed the emitter photodynamics, showing their potential as fluorescent markers for bioimaging applications as well as a platform for super-resolution imaging and quantum sensing.

7.1.4. Grain dependant growth of bright quantum emitters in hexagonal boron nitride

Noah Mendelson†, Luis Morales, Chi Li, Ritika Ritika, Minh Anh Phan Nguyen, Jacqueline Loyola-Echeverria, Sejeong Kim, Stephan Götzinger, Milos Toth, Igor Aharonovich
Advanced Optical Materials, 9(1), 2001271, (2021)

Bottom-up approaches to 2D material fabrication has two primary advantages over top-down fabrication methods—namely, the ability to fabricate large scale thin films (cm scale) with a controlled thickness, and the ability to manipulate the photophysical properties of the incorporated SPEs during growth. During this study, the incorporation of quantum emitters during chemical vapour deposition growth on nickel substrates were investigated. Following this, the system was then integrated with a planar dielectric antenna[198].

A low-pressure CVD growth of hBN on polycrystalline Ni foils show a selective incorporation of hBN emitters grown specifically on (001) grains in the Ni, despite growth in all grain orientations. Figure 7.5 (a), (b), and (c) shows optical, SEM, and electron back-scatter detection (EBSD) images, respectively, displaying the polycrystalline growth of the hBN. Quantum emitters were observed from these samples, with the emitters only appearing within the (001) direction in the Ni grain. This is conveyed, respectively, in Figure 7.5 (d) and (e), showing a characteristic spectrum, an inset $g^{(2)}(\tau)$ autocorrelation function, and widefield fluorescence image with grain boundaries and directions labelled. The reason for this preferentiality is hypothesised to be due to the variations in diffusion and subsequent supply of atomic species during growth, varying depending on grain orientation of the Ni catalyst.

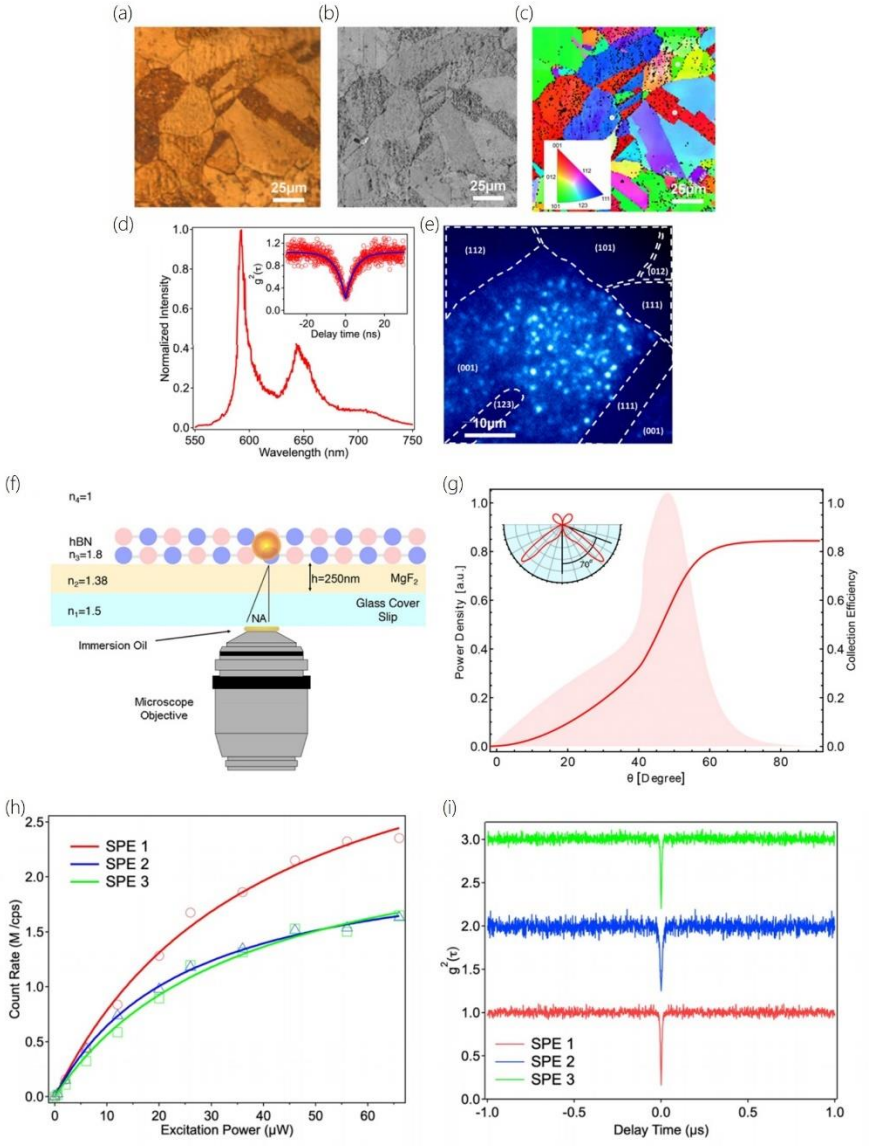

Figure 7.5. Characterisation of hBN thin films grown on Ni substrate. Specific area of the hBN as viewed on (a) optical microscope, (b) SEM, and (c) EBSD maps. (d) Spectra of emitter with inset autocorrelation function. (e) Wide-field image of hBN film with defined grains marked by broken white lines. (f) Schematic illustration of experimental setup used. (g) Simulated power density (light red region), and collection efficiency (red line) as a function of the collection angle for the antenna integrated hBN SPE. (h) Saturation curves for 3 separate hBN SPEs. (i) Corresponding $g^{(2)}(\tau)$ collections for the 3 emitters in (h). Reproduced from Ref.[198].

A planar dielectric antenna (PDA) was then integrated with the grown hBN to enhance collection efficiency from the source. Figure 7.5 (f) shows the schematic illustration of the PDA design used,

consisting of hBN atop a glass coverslip coated with a 250 nm layer of MgF_2. Figure 7.5 (g) shows simulated values of collection efficiency and relative power density from an in-plane linearly polarised dipole in hBN as integrated with the PDA. It was found that more than 84% of the fluorescence emission is channelled, when coupled with a high-NA (1.46) oil-immersion objective. Three separate emitters from the arrangement were measured showing saturated count rates of 3.92, 2.27, and 2.59 M counts/s, and their quantum emission preserved [Figure 7.5 (h) and (i), respectively].

In summary, hBN SPEs were grown on polycrystalline Ni foil and were demonstrated to be incorporated preferentially into hBN on Ni (001) grains. Additionally, the hybridisation of this system was performed to create a structure with a high collection efficiency. All of these serve to highlight the potential hBN has as a source device integration.

7.2. Contributed works on the manipulation of hBN emitters

7.2.1. Observation of Fourier transform limited lines in hexagonal boron nitride

Andreas Dietrich†, Markus. Bürk, Elena E Steiger, Lukas Antonuik, Trong Toan Tran, Minh Anh Phan Nguyen, Igor Aharonovich, Fedor Jelezko, Alexander Kubanek
Physical Review B, 98, 081414(R), 2018

As prime building blocks for integrated quantum photonics, SPEs are required to be free from spectral diffusion, dephasing, or competing phonon processes—approaching Fourier limited lines. In this fundamental study, single defect centres and their spectral properties were thoroughly examined through manipulation with resonant-excitation across 627 different defect centres[199].

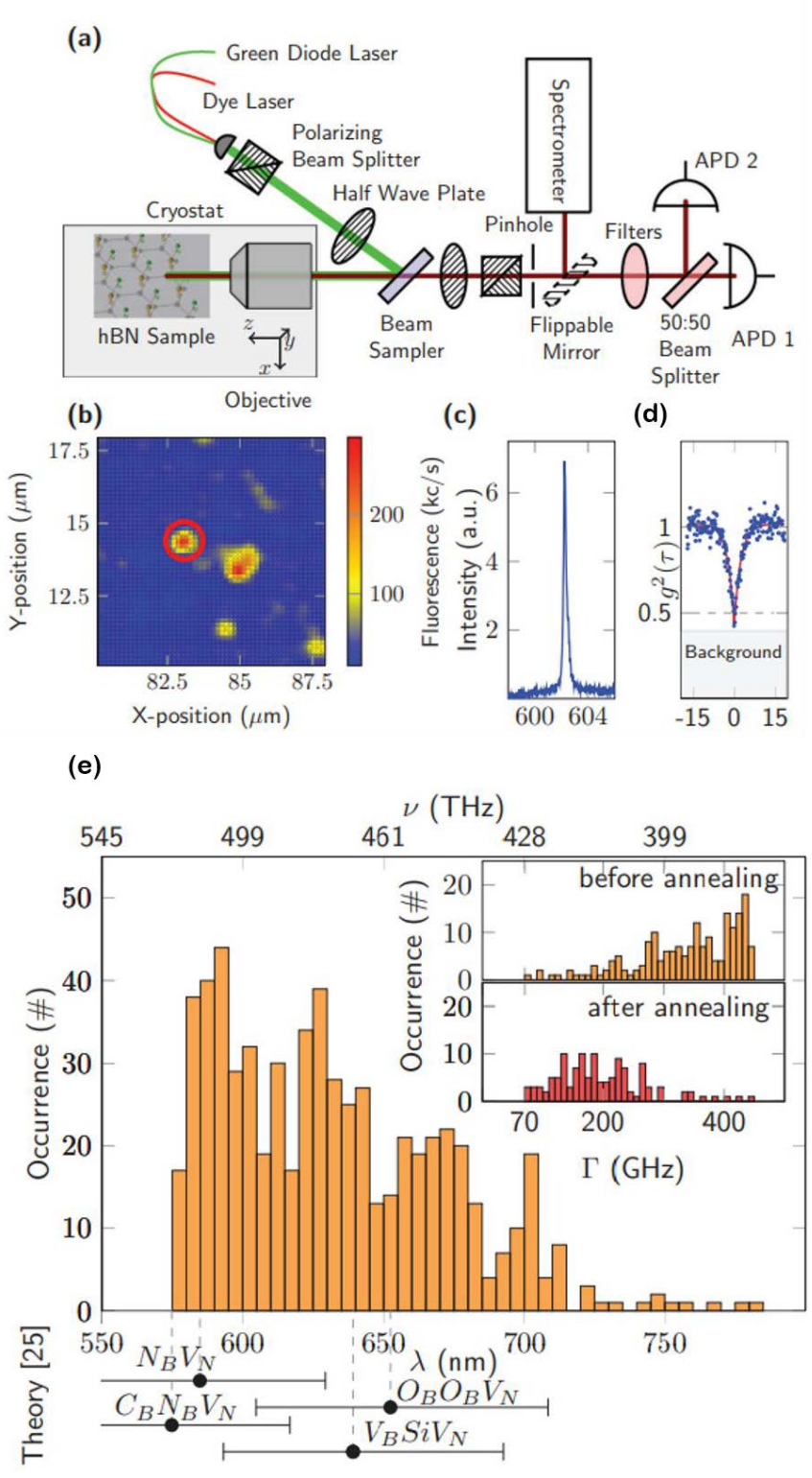

Figure 7.6. Methods and characterisation of hBN single defects linewidths. (a) Schematic of experimental setup used to characterise optical and quantum properties of hBN defects. A 0.9 NA air-objective was used with a 532 nm CW laser was used for off-resonant excitation, while a CW Matisse DS dye laser was used

for resonant excitation. (b) Confocal scan of an example emitter in hBN flakes with off-resonant excitation. (c) Off-resonant spectrum and $g^{(2)}(\tau)$ autocorrelation function of the emitter marked in (b). (e) Histogram of 627 individual ZPLs, with inset figures showing the distribution of linewidths before (orange) and after (red) annealing. DFT functional theory was used to calculate possible defect arrangements, with their most likely wavelengths highlighted below the x-axis. Reproduced from Ref.[199]

A schematic of the experimental setup used for optical characterisation is shown in Figure 7.6 (a)—a confocal microscope integrated with a continuous flow cryostat. hBN flakes mounted on a silver mirror were cooled to liquid-helium temperatures, where their spectra and quantum nature are probed, via a spectrometer and HBT interferometer respectively—the results of which shown in Figure 7.6 (b)–(d). A total of 627 emitters were recorded, with the histogram of their individual ZPLs shown in Figure 7.6 (e).

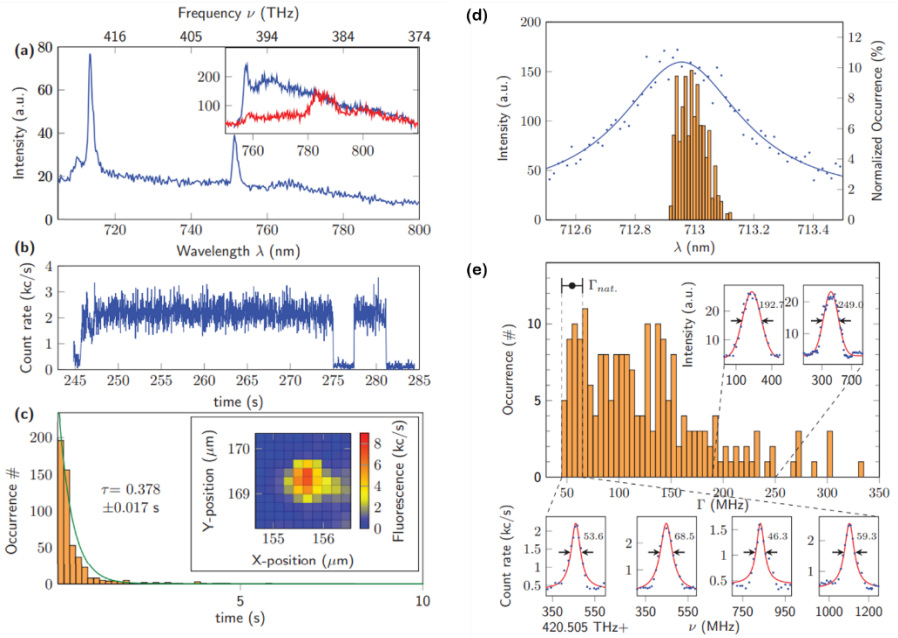

Figure 7.7. Characterisation of FT limited lines with an example emitter. (a) PL spectrum of the investigated emitter at an emission wavelength of 713 nm with an additional emitter at 755 nm. Inset shows PSB, with the aid of a 750 nm LP filter. (b) Blinking characteristics of the emitter when excited on-resonance. (c) Statistics of ON time of the fluorescence traces, disclosing a time constant of 0.37 s for spectral instabilities. Inset shows a 2D map of the emitter in resonant excitation, showing minimal fluctuations of the fluorescence signal. (d) PL spectrum (blue trace) showing an

inhomogeneous linewidth of ~293 GHz, with the histogram of the PLE lines revealing an inhomogeneous linewidth of ~67.5 GHz. (e) Examples of four emitters exhibiting linewidths within an error of the natural linewidth of 55 MHz.

Off-resonant excitation reveals an average linewidth of 213 GHz, post annealing across the entire sample of emitters. Following this, resonant excitation was performed with a tuneable CW dye laser, further reducing this linewidth. An emitter with a ZPL emission line at 713 nm was used as an example to show this reduction, with a narrow inhomogeneous linewidth of 293 GHz [its ZPL displayed in Figure 7.7 (a)]. The PL signal from its resonant excitation was collected from its PSB, with the phonon peak at ~785 nm, corresponding to a known phonon mode of hBN at 187 meV as reported from prior studies. The linewidth during resonant excitation was collected by performing PLE line scans at a faster rate than the characteristic diffusion time of the emitter, at $\tau = 0.378$ s [Figure 7.7 (c)]. The resultant normalised spectral width was shown to be 67.5 ± 9.5 GHz, which when further processed [including filtering out of all data showing blinking as displayed in Figure 7.7 (b)], resulted in a FT limited linewidth of $\Gamma_{nat} = 55.26 \pm 0.19$ MHz, given the emission lifetime of 2.88 ns. 39 other ZPL lines recorded are shown to lie within an error margin of the natural linewidth of 55 ± 10 MHz—with four examples of those in Figure 7.7(e).

In summary, FT limited, single-photon emission from defect centres in hBN were observed, free from significant spectral diffusion or spectral instability for upwards of 30 seconds. This platform of hBN demonstrates the compatibility of such systems to facilitate indistinguishable photons of up to GHz rates.

7.2.2. All-optical control and super-resolution imaging of quantum emitters in layered materials

Mehran Kianina, Carlo Bradac, Bernd Sontheimer, Fan Wang, Toan Trong Tran, Minh Anh Phan Nguyen, Sejeong Kim, Zai-Quan Xu, Dayong Jin, Andreas W. Schell, Charlene J. Lobo, Igor Aharonovich, Milos Toth
Nature Communications, 9, 874 (2018)

The thorough understanding of the level-structure of a quantum emitter is most crucial for employing such a source for integrated devices. Knowing the system's photodynamic processes allows for the control of its properties such as electron state population, and selectivity of certain transitions—which, when exploited, can expand its scope of application. During this study, a series of systematic experiments were designed to further uncover information regarding the complex level structure and photodynamics of hBN quantum emitters—specifically, the existence of a class of emitter with a fast-decaying intermediate and long-lived metastable state accessible from the first excited electronic state[200].

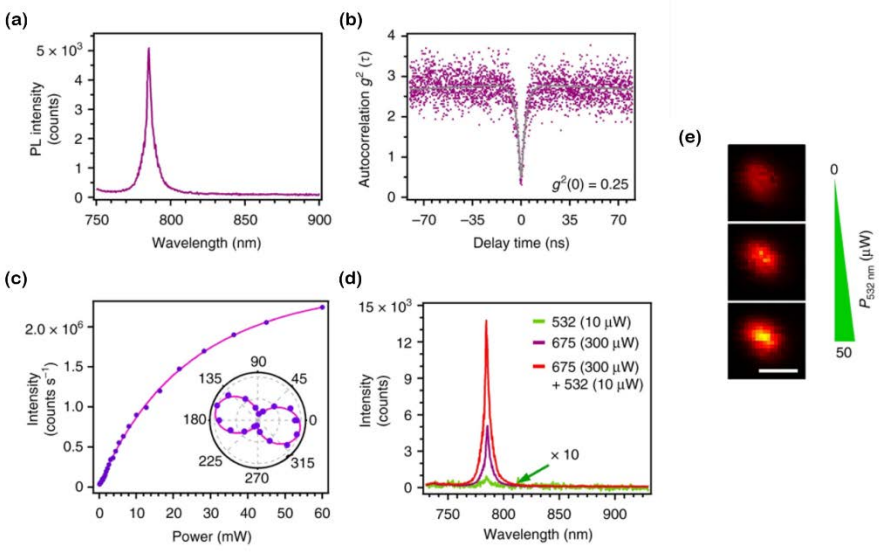

Figure 7.8. Optical characterisation of a hBN emitter. PL spectrum of a single defect under 675 nm excitation. (b) $g^{(2)}(\tau)$ second-order autocorrelation measurement, showing a dip at $g^{(2)}(0) = 0.25$. (c) Saturation curve of the emitter under excitation with a 708 nm laser. (d) PL spectra of the single defect under three excitation conditions: low-power (532 nm CW, green trace), high-power (675

nm CW, purple trace), and a combination of the two (red trace). (e) Non-linear increase of the emitter brightness upon linear increase of 532 nm excitation power, coincident with the 675 nm excitation laser. Reproduced from Ref.[200]

An emitter with a ZPL at 778 nm was characterised with a 675 nm CW laser and probed for quantum emission and saturation, as shown in Figure 7.8 (a), (b), and (c), respectively. Additional characterisation of its emission intensity from three excitation schemes (532 nm CW at 10 μW, 675 nm at 300 μW, and a combination of both) reveal a non-linear response [Figure 7.8 (d)]. Further investigation of the photophysics *via* long autocorrelation measurements, reveal the presence of additional intermediate/metastable state energy levels, allowing for the repumping of system back to the excited state and decaying radiatively. This in turn, explains the non-linear response observed in Figure 7.8 (d).

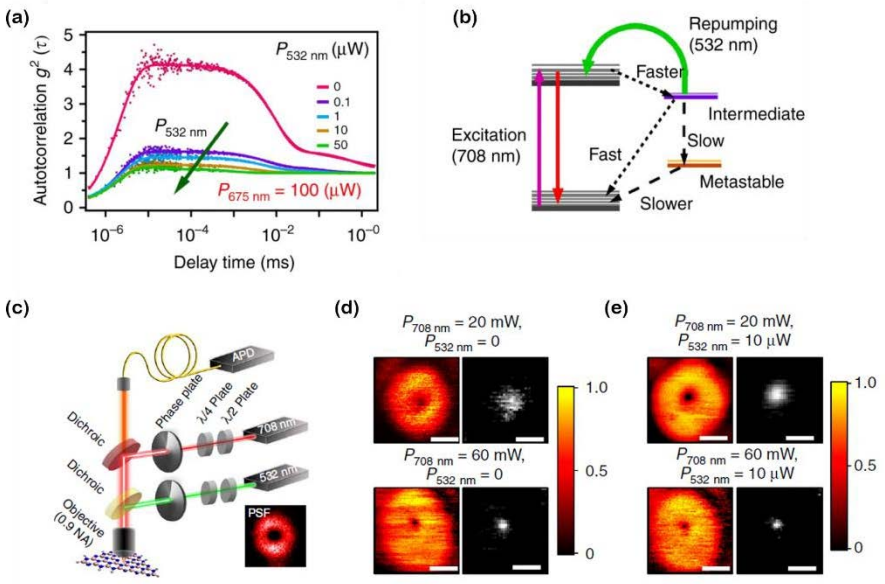

Figure 7.9. Photophysics of the single emitter introduced in Figure 7.8. along with its super-resolution imaging. (a) Long autocorrelation measurements under excitation with a 675 nm laser. (b) Schematic of the four-level electronic system, unique to this class of emitter. (c) Schematic diagram of the coincident GSD setup. Super-resolution images using the (d) single vortex-beam scheme, and (e) coincident vortex-beam scheme. Reproduced from Ref.[200]

Having established the novel photodynamics of this class of emitter, its properties were then manipulated to realise and demonstrate a new modality of far-field, sub-diffraction fluorescence nanoscopy. Two schemes using a modified version of negative ground-state depletion (GSD) was used to exploit spatially modulated light beams with bright and dark gradients to selectively image emitters at a resolution below the diffraction limit. Figure 7.9 (c) shows the schematic diagram of the excitation schemes; the first using a vortex-beam as the excitation source, while the other using a coincident pair of two vortex beams. GSD imaging allows for the 'switching off' of the emitters around the doughnut null, as the beam shelves the system into a long-lived dark state. The result of this scanning technique is a high-null-high emission pattern, allowing for a spatial resolution much lower than the calculated diffraction limit of the system. Additionally, it was found that the resolution would further decrease with increasing vortex-beam excitation power. In this scheme, a resolution of 87 ± 10 nm was achieved. The resolution was then reduced further with the addition of a lower-power 532 nm repumping vortex beam allowing for the quicker shelving of the system, resulting in a resolution of 63 ± 4 nm—well below the calculated resolution limit (~460 nm).

In summary, the optical manipulation of hBN emitters were achieved, selectively inducing the population of specific energy levels. There was a discovery of unique properties including non-linear behaviour and a four-level system consisting of an intermediate shelving state. This energy system was then exploited in an example of super-resolution imaging, showcasing the potential of this system for specialised applications in sub-diffraction nanoscopy.

7.2.3. Integrated on chip platform with quantum emitters in layered materials

Sejeong Kim, Ngoc My Hanh Duong, Minh Anh Phan Nguyen, Tsung-Ju Lu, Mehran Kianinia, Noah Mendelson, Alexander Solntsev, Carlo Bradac, Dirk R. Englund, Igor Aharonovich
Advanced Optical Materials, 7, 23 (2019)

Efficient integration of quantum light sources can be achieved with photonic resonators to realise waveguiding and enhancement. In this study, hBN quantum emitters are successfully coupled to dielectric waveguides using a pick-and-place approach[201].

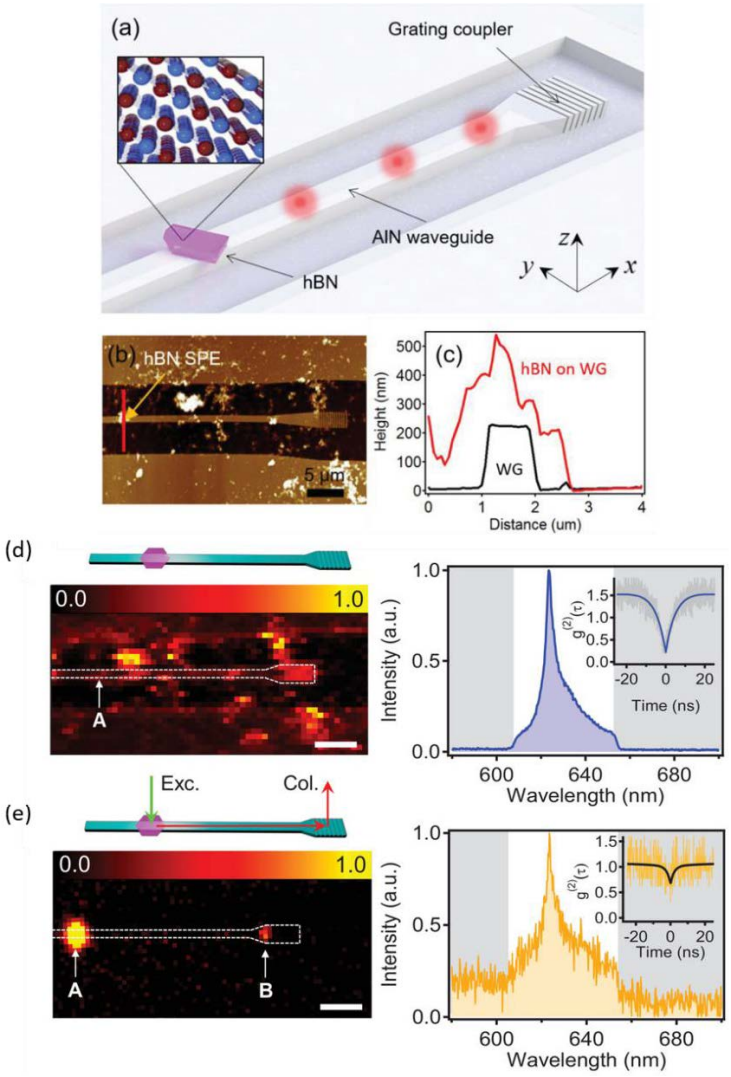

Figure 7.10. Coupling of hBN emitters to AlN waveguides. (a) Schematic illustration of the hBN flake hosting quantum emitters, integrated with an AlN waveguide. (b) AFM scan of the flake on

the waveguide. (c) Corresponding cross-sectional line-scans of the height of the waveguide (black trace) and the hBN flake on top of the waveguide (red trace). (d) Collection scheme, where the emitter is measured directly (labelled A). The filtered spectra and inset second-order autocorrelation function are to the right. (e) Collection scheme, where the emitter is measured from the grating coupler (labelled B), along with its corresponding filtered spectra and inset second-order autocorrelation function to the right. Reproduced from Ref.[201]

Figure 7.10 (a) depicts a schematic diagram integrated hBN/AlN waveguide. The hBN defect hosted within the flake sits on top of the waveguide, and its emission is coupled to the structure's transverse electric mode. Figure 7.10 (b) and (c) show AFM scans of the waveguide and hBN, and their respective height maps. Towards the end of the waveguide is a grating which acts as an antenna to facilitate either coupling, or—in this case—outcoupling of the guided light. Optical characterisation of the emitter was performed at both ends of the waveguide, measuring at the hBN flake itself, and at the grating outcoupler. The results show a successful coupling of the emission, however with a low coupling efficiency of ~7% and the quantum emission diminished due to the decrease in SNR.

Despite these, the results show an example of the successful integration of hBN emitters with dielectric nanophotonic structures. Its light can be spatially manipulated through waveguiding, transporting the light from one position to another, showing the potential for its use in integrated on-chip optical circuits.

Chapter 8

Conclusions and outlook

8.1. Summary of thesis

During this thesis, quantum emitters in three solid-state materials—GaN, diamond, and hBN—have been investigated for applications in QIP. In this respect, the presented works have been separated into two distinct parts, considered crucial for the journey towards mature nanophotonic devices. The former details the creation of single-photon emitting defects and the understanding of their origins, while the latter presents fundamental studies regarding the manipulation of their optical properties, leading then into its integration with additional nanophotonic constituents.

The high-yield and reliable creation of bright photostable quantum emitters is the first crucial step towards the fabrication of nanophotonic devices. Understanding the material properties and growth dynamics which create these emitters help to further the understanding behind the emitters origins—of which are still areas of debate and intrigue for many quantum emitter systems.

Of these systems is GaN, a semiconductor hosting SPEs with the unique property of flexibility in growth. The effects of growth conditions and microstructure were investigated, with the correlation between threading dislocations and spatial positions of the quantum emitters in mind. It was found that the correlation is non-trivial, showing a disparity between dislocation density and emitter density, but not no spatial correlation. The new-found hypothesis in this case

is that the quantum emitters in this material are related to extrinsic impurities introduced during growth.

hBN is another material system hosting SPEs with favourable optical properties—namely a high brightness, and pure linearly polarised quantum emission—making it a strong candidate for quantum applications. The effect of high-energy, electron irradiation on the creation of quantum emitters were characterised. MeV electrons were accelerated towards several different types of hBN flakes, with the intention to make vacancies by ejecting atoms from the lattice. The result of this is the high-yield creation of quantum emitters across the flakes, and crucially on the flat regions of the hBN flake—an area which prior methods were unable to achieve. Both of these studies serve to provide further insight into the origins of the emitters in their respective emitter system, through their methods of creation.

Following the understanding and fabrication of these quantum emitters, the next crucial step is then to manipulate their optical properties to enhance and modify its emission. This can be realised by changing the local densities of states surrounding the emitter, a modification achieved through the integration with nanophotonic cavities.

A fundamental study was performed on GeV colour centres in diamond, quantifying the effect of changing local densities of states has on its internal QE—a value not yet characterised experimentally. The study involved a modification of the thickness of the dielectric environment surrounding the host crystal (in this case was the polymer PMMA), resulting in a correspondingly different local density of states. By comparing emission lifetimes at different points of PMMA thickness, the internal QE of a system can be calculated. In this instance, ensembles were used to approximate an internal QE of ~22%.

Finally, another fundamental study was performed on hBN SPEs, with their coupling to a gold spherical nanocavities. Plasmonic cavities can produce nanoscale mode volumes of highly confined densities of states, resulting in very minute coupling arrangements, and large enhancement when coupled to the plasmonic field. Through exploiting their linear transition dipole emission orientation of hBN emitters, a larger majority of the light emitted can be coupled to an Au nanosphere, allowing for a more efficient configuration. AFM was used to push the Au nanospheres into close proximity within ~20 nm of the host flake, resulting in a characteristic reduction of emitter lifetime by a factor of 3.19, and an enhancement of saturated emission countrate by a factor of 3.09—resulting in an overall countrate of over 5.8 M counts. This was an important study which shows the large potential hBN possesses as a source for integrated devices. This was again reinforced with the seven studies described in Chapter 7. These studies aim to show how emission from quantum sources can be manipulated and enhanced through a modification of its surrounding environment.

8.2. Outlook and future directions

The studies presented throughout this thesis highlight the strengths and advantages which make solid-state quantum emitters a promising class of source for applications requiring quantum nanophotonic architecture. Naturally, these fundamental studies provide a foundation for further research, advancing their respective fields. Possible suggestions for potential future work and its outlook is detailed within this section for each respective project.

Despite numerous studies on quantum emitters in GaN, the field itself is still in its infancy, with the origins of its emission still largely

unknown. Additional fundamental studies on different techniques of growth and deterministic incorporation of extrinsic impurities would be beneficial to more accurately determining the source of its emission. Ultra-pure growth procedures combined with direct ion implantation could be a precise method of testing the effect of individual impurities for their correlation to emitter creation. One of the main milestones with GaN is—as with any solid-state system—to find the origins of the emitter. However after determining this, the next milestone will involve exploiting the elaborate and diverse growth procedures to create distinct structures on choice substrates for quantum applications. Localised emitter formation for integrated on-chip nanophotonic devices is well sought-after, and can potentially be made possible through the use of GaN and its emitters.

Similarly for quantum emitters in hBN, its unknown origins warrants further studies allowing for the deterministic creation of quantum emitters. Extended fundamental studies involving the controlled introduction of impurity atoms and monitoring the spectral signatures of the resultant emitters would greatly benefit the understanding of its origins. Additionally, having seen the capabilities of the material system when coupled to additional nanophotonic constituents, more exotic structures such as waveguides and resonators, both plasmonic and dielectric, would further advance the field and bring the realisation of integrated hBN sources one step closer. An example of this could be a reduction of its lifetime, approaching the dephasing time of the emitter through highly confined cavity modes, to acquire indistinguishable photons.

The study on GeV revealed its high QE compared to SiV and shows its promising properties for quantum devices. Having a high QE results in more efficient emission of high purity single-photons, critical for quantum nanophotonic applications. Upon cementing the solid

foundations for this quantum system, it would then be advantageous to begin integration and interfacing of this material system with additional nanophotonic architecture to further enhance and manipulate its emission. The potential amalgamation with nano-constituents such as waveguides (dielectric or plasmonic), various cavity designs, as well as contacts for electrical manipulation, is extensive and abundant as seen in many works involving nanodiamonds. All of these arrangements further the progress towards realising GeV colour centres for nanophotonic devices for quantum applications.

Appendix

This section details the technical procedures and schematics of the experimental and analytical methods necessary for the measurements of data presented in this thesis.

Second-order autocorrelation normalisation and background correction

The procedure for analytically normalising $g^{(2)}(\tau)$ autocorrelation data follows the works presented by Beveratos et. al[202]. The raw correlation data can be expressed in terms of coincidence count rate $c(\tau)$ counted during a time T within collection bins of width w, given by

$$C_N^{cw}(\tau) \quad = \quad c(\tau)/(N_1 N_2 w T)$$

where $N_{1,2}$ are the count rates at their respective detector. The normalised coincidence rate $C_N^{cw}(\tau)$ is then corrected for the background light B, and can then be expressed as

$$g^{(2)}(\tau) \quad = \quad [C_N^{cw}(\tau) - (1-\rho^2)]/\rho^2$$

where $\varrho = \mathrm{S}/(\mathrm{S} + \mathrm{B})$ is the relation expressing signal to background ratio, measured independently in each experimental run by measuring the count rate close to the emitter.

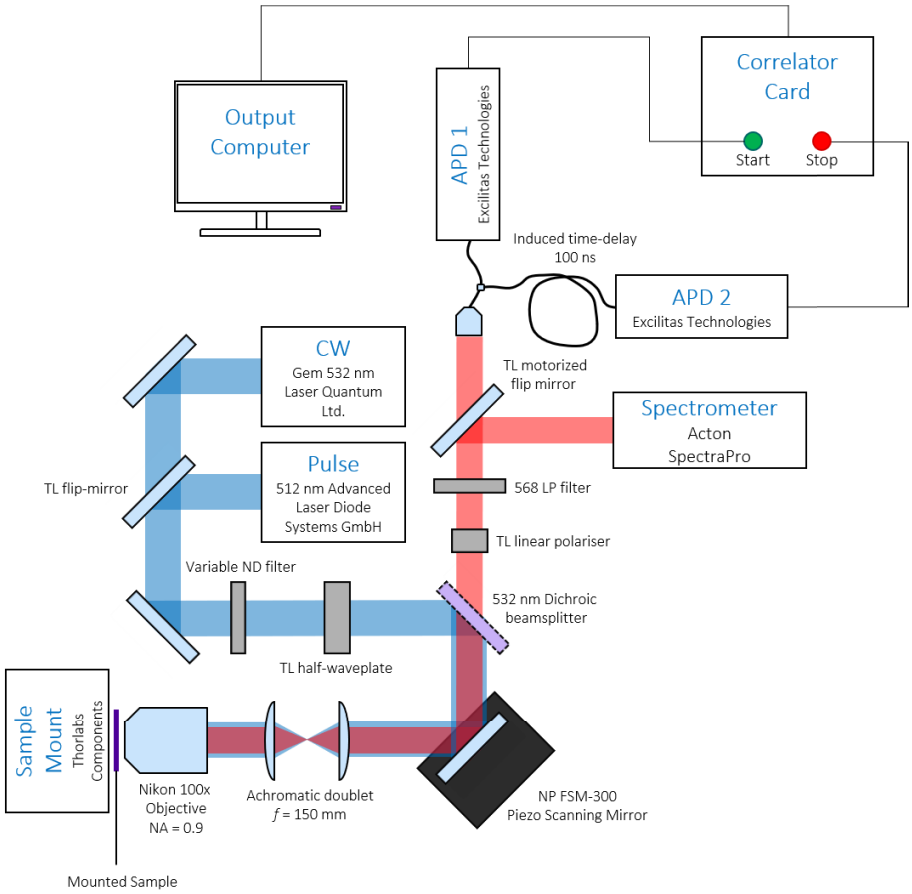

Figure. A.1. Schematic illustration of confocal microscope used for all optical characterisation of single-photon emitters. Legend: TL – Thorlabs, ND – Neutral density, LP – Long-pass, NP – Newport.

Bibliography

1. Tame, M. S., Bell, B. A., Di Franco, C., Wadsworth, W. J. & Rarity, J. G. Experimental realization of a one-way quantum computer algorithm solving Simon's problem. *Phys. Rev. Lett.* 113, 1–2 (2014).

2. Atatüre, M., Englund, D., Vamivakas, N., Lee, S. Y. & Wrachtrup, J. Material platforms for spin-based photonic quantum technologies. *Nat. Rev. Mater.* 3, 38–51 (2018).

3. Wang, D., Wu, J. & Yi, X. Optical quantum computing. *Proc. - Int. Conf. Nat. Comput.* 2016-Janua, 390–397 (2016).

4. Ladd, T. D. *et al.* Quantum computers. *Nature* 464, 45–53 (2010).

5. Alléaume, R. *et al.* Experimental open-air quantum key distribution with a single-photon source. *New J. Phys.* 6, 1–14 (2004).

6. O'Brien, J. L., Furusawa, A. & Vučković, J. Photonic quantum technologies. *Nat. Photonics* 3, 687–695 (2009).

7. Popescu, S., Linden, N. & Jozsa, R. Quantum Information and Computation. *J. Phys. A. Math. Gen.* 34, 6723–6723 (2001).

8. Feynman, R. P., Vernon, F. L. & Hellwarth, R. W. Geometrical Representation of the Schrödinger Equation for Solving Maser Problems. *J. Appl. Phys.* 28, 49–52 (1957).

9. Beveratos, A. *et al.* Single Photon Quantum Cryptography. *Phys. Rev. Lett.* 89, 4–7 (2002).

10. Hartmann, M. J. Quantum simulation with interacting photons. *J. Opt. (United Kingdom)* 18, (2016).

11. Fisher, A. J. Quantum computing in the solid state: The challenge of decoherence. *Philos. Trans. R. Soc. A Math. Phys. Eng. Sci.* 361, 1441–

1450 (2003).

12. Chunnilall, C. J., Degiovanni, I. Pietro, Kück, S., Müller, I. & Sinclair, A. G. Metrology of single-photon sources and detectors: a review. *Opt. Eng.* 53, 081910 (2014).

13. Von Helversen, M. *et al.* Quantum metrology of solid-state single-photon sources using photon-number-resolving detectors. *New J. Phys.* 21, (2019).

14. Aharonovich, I., Englund, D. & Toth, M. Solid-state single-photon emitters. *Nature Photonics* vol. 10 631–641 (2016).

15. Fedorych, O. *et al.* Room temperature single photon emission from an epitaxially grown quantum dot. *Appl. Phys. Lett.* 100, (2012).

16. Kako, S. *et al.* A gallium nitride single-photon source operating at 200K. *Nat. Mater.* 5, 887–892 (2006).

17. Schröder, T., Gädeke, F., Banholzer, M. J. & Benson, O. Ultrabright and efficient single-photon generation based on nitrogen-vacancy centres in nanodiamonds on a solid immersion lens. *New J. Phys.* 13, (2011).

18. Iwasaki, T. *et al.* Germanium-Vacancy Single Color Centers in Diamond. *Sci. Rep.* 5, (2015).

19. Müller, T. *et al.* Optical signatures of silicon-vacancy spins in diamond. *Nat. Commun.* 5, (2014).

20. Lohrmann, A. *et al.* Single-photon emitting diode in silicon carbide. *Nat. Commun.* 6, (2015).

21. Wang, J. *et al.* Bright room temperature single photon source at telecom range in cubic silicon carbide. *Nat. Commun.* 9, (2018).

22. Tran, T. T., Bray, K., Ford, M. J., Toth, M. & Aharonovich, I. Quantum emission from hexagonal boron nitride monolayers. *Nat. Nanotechnol.* (2016) doi:10.1038/nnano.2015.242.

23. Tran, T. T. *et al.* Robust multicolor single photon emission from point defects in hexagonal boron nitride. in *2017 Conference on Lasers and Electro-Optics, CLEO 2017 - Proceedings* vols 2017-Janua 1–2 (2017).

24. Wang, J. *et al.* Lateral overgrowth of thick GaN on patterned GaN substrate by sublimation technique. *Japanese J. Appl. Physics, Part 1 Regul. Pap. Short Notes Rev. Pap.* 37, 4475–4476 (1998).

25. Berhane, A. M. *et al.* Bright Room-Temperature Single-Photon Emission from Defects in Gallium Nitride. *Adv. Mater.* 29, 1605092 (2017).

26. Kaneda, F., Garay-Palmett, K., U'Ren, A. B. & Kwiat, P. G. Heralded single-photon source utilizing highly nondegenerate, spectrally factorable spontaneous parametric downconversion. *Opt. Express* 24, 10733 (2016).

27. Bock, M. *et al.* High-fidelity entanglement between a trapped ion and a telecom photon via quantum frequency conversion. *Nat. Commun.* 9, 1–7 (2018).

28. Higginbottom, D. B. *et al.* Pure single photons from a trapped atom source. *New J. Phys.* 18, (2016).

29. Loudon, R. *The Quantum Theory of Light. Oxford University Press* (Oxford University Press, 2000). doi:10.1119/1.1987930.

30. Gerry, C. C. & Night, P. L. *Introductory Quantum Optics. Cambridge University Press* (Cambridge University Press, 2005). doi:10.1109/MSP.2005.1458311.

31. Bennett, R., Barlow, T. M. & Beige, A. A physically motivated quantization of the electromagnetic field. *Eur. J. Phys.* 37, (2015).

32. Meystre, P. & Sargent, M. *Elements of Quantum Optics. Springer* (Springer, 2007).

33. Fox, M. *Quantum optics. Springer Handbook of Lasers and Optics* (2012). doi:10.1007/978-3-642-19409-2_18.

34. Lindon, J. C., Tranter, G. E. & Koppenaal, D. W. *Encyclopedia of Spectroscopy and Spectrometry. Elsevier* vol. 2 (Elsevier, 2000).

35. Zhou, Y. *et al.* Room temperature solid-state quantum emitters in the telecom range. *Sci. Adv.* 4, (2018).

36. Berhane, A. M. *et al.* Photophysics of GaN single-photon emitters in the visible spectral range. *Phys. Rev. B* 97, 1–8 (2018).

37. Nguyen, M. *et al.* Photodynamics and quantum efficiency of germanium vacancy color centers in diamond. *Adv. Photonics* 1, 1 (2019).

38. Aharonovich, I. & Neu, E. Diamond nanophotonics. *Adv. Opt. Mater.* 2, 911–928 (2014).

39. Tran, T. T. *et al.* Robust Multicolor Single Photon Emission from Point Defects in Hexagonal Boron Nitride. *ACS Nano* 10, 7331–7338 (2016).

40. Tran, T. T., Bray, K., Ford, M. J., Toth, M. & Aharonovich, I. Quantum Emission from Hexagonal Boron Nitride Monolayers. *Nat. Nanotechnol.* 11, 37–41 (2015).

41. Castelletto, S. & Boretti, A. Silicon carbide color centers for quantum applications. *JPhys Photonics* 2, (2020).

42. Castelletto, S. *et al.* A silicon carbide room-temperature single-photon source. *Nat. Mater.* 13, 151–156 (2014).

43. Holmes, M. J., Choi, K., Kako, S., Arita, M. & Arakawa, Y. Room-temperature triggered single photon emission from a III-nitride site-controlled nanowire quantum dot. *Nano Lett.* 14, 982–986 (2014).

44. Eisaman, M. D., Fan, J., Migdall, A. & Polyakov, S. V. Invited Review Article: Single-photon sources and detectors. *Rev. Sci. Instrum.* 82, 071101 (2011).

45. Siyushev, P. *et al.* Coherent properties of single rare-earth spin qubits. *Nat.*

Commun. 5, 1–6 (2014).

46. Liu, Z. H., Ng, G. I., Zhou, H., Arulkumaran, S. & Maung, Y. K. T. Reduced surface leakage current and trapping effects in AlGaN/GaN high electron mobility transistors on silicon with SiN/ Al2 O3 passivation. *Appl. Phys. Lett.* 98, 3506 (2011).

47. Krames, M. R. *et al.* Status and future of high-power light-emitting diodes for solid-state lighting. *IEEE/OSA J. Disp. Technol.* 3, 160–175 (2007).

48. Matocha, K., Chow, T. P. & Gutmann, R. J. High-voltage normally off GaN MOSFETs on sapphire substrates. *IEEE Trans. Electron Devices* 52, 6–10 (2005).

49. Jewett, S. A., Makowski, M. S., Andrews, B., Manfra, M. J. & Ivanisevic, A. Gallium nitride is biocompatible and non-toxic before and after functionalization with peptides. *Acta Biomater.* 8, 728–733 (2012).

50. Sanford, N. A. *et al.* Measurement of second order susceptibilities of GaN and AlGaN. *J. Appl. Phys.* 97, 053512 (2005).

51. Yu, E. T., Dang, X. Z., Asbeck, P. M., Lau, S. S. & Sullivan, G. J. Spontaneous and piezoelectric polarization effects in III–V nitride heterostructures. *J. Vac. Sci. Technol. B Microelectron. Nanom. Struct.* 17, 1742 (1999).

52. Nakamura, N., Ogi, H. & Hirao, M. Elastic, anelastic, and piezoelectric coefficients of GaN. *J. Appl. Phys.* 111, (2012).

53. Kente, T. & Mhlanga, S. D. Gallium nitride nanostructures: Synthesis, characterization and applications. *J. Cryst. Growth* 444, 55–72 (2016).

54. Lee, M. L., Wang, S. S., Yeh, Y. H., Liao, P. H. & Sheu, J. K. Light-emitting diodes with surface gallium nitride p–n homojunction structure formed by selective area regrowth. *Sci. Rep.* 9, 1–7 (2019).

55. Feng, D. H., Jia, T. Q. & Xu, Z. Z. Electronic structure and optical

properties of zinc-blende GaN quantum dots. *Chinese Phys.* 12, 1016–1020 (2003).

56. Shin, M. J. *et al.* A GaN nanoneedle inorganic/organic heterojunction structure for optoelectronic devices. *Mater. Lett.* 91, 191–194 (2013).

57. Nabi, G. *et al.* Synthesis, characterization, photoluminescence and field emission properties of novel durian-like gallium nitride microstructures. *Mater. Chem. Phys.* 133, 793–798 (2012).

58. Jeffries, A. M. *et al.* Gallium nitride grown by molecular beam epitaxy at low temperatures. *Thin Solid Films* 642, 25–30 (2017).

59. Zhong, Z., Qian, F., Wang, D. & Lieber, C. M. Synthesis of p-type gallium nitride nanowires for electronic and photonic nanodevices. *Nano Lett.* 3, 343–346 (2003).

60. Koester, R., Hwang, J. S., Durand, C., Le Si Dang, D. & Eymery, J. Self-assembled growth of catalyst-free GaN wires by metal-organic vapour phase epitaxy. *Nanotechnology* 21, (2010).

61. Lee, K. *et al.* Self-assembled growth and structural analysis of inclined GaN nanorods on nanoimprinted m-sapphire using catalyst-free metal-organic chemical vapor deposition. *AIP Adv.* 6, (2016).

62. Sammes, N. *Engineering Materials and Processes*. (2006).

63. Wang, X. & Yoshikawa, A. Molecular beam epitaxy growth of GaN, AlN and InN. *Prog. Cryst. Growth Charact. Mater.* 48–49, 42–103 (2004).

64. Kuo, H.-C. & Shen, S.-C. *Nitride Semiconductor Light-Emitting Diodes (LEDs): Materials, Technologies, and Applications*. (2018).

65. Bockowski, M. Review: Bulk growth of gallium nitride: challenges and difficulties. *Cryst. Res. Technol.* 42, 1162–1175 (2007).

66. Utsumi, W. *et al.* Congruent melting of gallium nitride at 6 GPa and its

application to single-crystal growth. *Nat. Mater.* 2, 735–738 (2003).

67. Koukitu, A. & Seki, H. Thermodynamic analysis on molecular beam epitaxy of GaN, InN and AlN. *Japanese J. Appl. Physics, Part 2 Lett.* 36, (1997).

68. Lieten, R. R. *et al.* Mg doping of GaN by molecular beam epitaxy. *J. Phys. D. Appl. Phys.* 44, (2011).

69. Pampili, P. & Parbrook, P. J. Doping of III-nitride materials. *Mater. Sci. Semicond. Process.* 62, 180–191 (2017).

70. Chèze, C. *et al.* Direct comparison of catalyst-free and catalyst-induced GaN nanowires. *Nano Res.* 3, 528–536 (2010).

71. Jasinski, J., Zakharov, D. N. & Berkeley, L. GaN grown in polar and non-polar directions. *Opto-Electronics Rev.* (2004).

72. Tomiya, S., Hino, T., Goto, S., Takeya, M. & Ikeda, M. Dislocation related issues in the degradation of GaN-based laser diodes. *IEEE J. Sel. Top. Quantum Electron.* 10, 1277–1286 (2004).

73. Moram, M. A., Oliver, R. A., Kappers, M. J. & Humphreys, C. J. The spatial distribution of threading dislocations in gallium nitride films. *Adv. Mater.* 21, 3941–3944 (2009).

74. Belabbes, A., De Carvalho, L. C., Schleife, A. & Bechstedt, F. Cubic inclusions in hexagonal AlN, GaN, and InN: Electronic states. *Phys. Rev. B - Condens. Matter Mater. Phys.* 84, 1–9 (2011).

75. Krueger, A. Diamond nanoparticles: Jewels for chemistry and physics. *Adv. Mater.* 20, 2445–2449 (2008).

76. Mochalin, V. N., Shenderova, O., Ho, D. & Gogotsi, Y. The properties and applications of nanodiamonds. *Nat. Nanotechnol.* 7, 11–23 (2012).

77. Wort, C. J. H. & Balmer, R. S. Diamond as an electronic material. *Mater. Today* 11, 22–28 (2008).

78. Thomas, M. E. & Tropf, W. J. *Optical properties of diamond. Johns Hopkins APL Technical Digest (Applied Physics Laboratory)* (Springer, 2001). doi:10.1201/9780429283260-7.

79. Zaitsev, A. Vibronic spectra of impurity-related optical centers in diamond. *Phys. Rev. B - Condens. Matter Mater. Phys.* 61, 12909–12922 (2000).

80. Bradac, C., Gao, W., Forneris, J., Trusheim, M. E. & Aharonovich, I. Quantum nanophotonics with group IV defects in diamond. *Nat. Commun.* 10, 1–13 (2019).

81. Evans, R. E., Sipahigil, A., Sukachev, D. D., Zibrov, A. S. & Lukin, M. D. Narrow-Linewidth Homogeneous Optical Emitters in Diamond Nanostructures via Silicon Ion Implantation. *Phys. Rev. Appl.* 5, 0440101–0440108 (2016).

82. Wang, C., Kurtsiefer, C., Weinfurter, H. & Burchard, B. Single photon emission from SiV centres in diamond produced by ion implantation. *J. Phys. B At. Mol. Opt. Phys.* 39, 37–41 (2006).

83. Neu, E. *et al.* Single photon emission from silicon-vacancy colour centres in chemical vapour deposition nano-diamonds on iridium. *New J. Phys.* 13, 025012,21 (2011).

84. Jahnke, K. D. *et al.* Electron-phonon processes of the silicon-vacancy centre in diamond. *New J. Phys.* 17, (2015).

85. Neu, E., Agio, M. & Becher, C. Photophysics of single silicon vacancy centers in diamond: implications for single photon emission. *Opt. Express* 20, 19956–19971 (2012).

86. Hepp, C. *et al.* Electronic structure of the silicon vacancy color center in diamond. *Phys. Rev. Lett.* 112, 0364051–0364055 (2014).

87. Ekimov, E. A., Kudryavtsev, O. S., Mordvinova, N. E., Lebedev, O. I. & Vlasov, I. I. High-Pressure Synthesis of Nanodiamonds from Adamantane:

Myth or Reality? *ChemNanoMat* 4, 269–273 (2018).

88. Sedov, V. *et al.* Growth of polycrystalline and single-crystal CVD diamonds with bright photoluminescence of Ge-V color centers using germane GeH4 as the dopant source. *Diam. Relat. Mater.* 90, 47–53 (2018).

89. Palyanov, Y. N., Kupriyanov, I. N., Borzdov, Y. M. & Surovtsev, N. V. Germanium: A new catalyst for diamond synthesis and a new optically active impurity in diamond. *Sci. Rep.* 5, (2015).

90. Bray, K. *et al.* Single Crystal Diamond Membranes and Photonic Resonators Containing Germanium Vacancy Color Centers. *ACS Photonics* (2018) doi:10.1021/acsphotonics.8b00930.

91. Zhou, Y. *et al.* Direct writing of single germanium vacancy center arrays in diamond. *New J. Phys.* 20, 2–7 (2018).

92. Bhaskar, M. K. *et al.* Quantum Nonlinear Optics with a Germanium-Vacancy Color Center in a Nanoscale Diamond Waveguide. *Phys. Rev. Lett.* 118, 1–6 (2017).

93. Gali, A. & Maze, J. R. Ab initio study of the split silicon-vacancy defect in diamond: Electronic structure and related properties. *Phys. Rev. B - Condens. Matter Mater. Phys.* 88, 1–7 (2013).

94. Rogers, L. J. *et al.* Electronic structure of the negatively charged silicon-vacancy center in diamond. *Phys. Rev. B - Condens. Matter Mater. Phys.* 89, (2014).

95. Ertug, B. Powder Preparation, Properties and Industrial Applications of Hexagonal Boron Nitride. in *Sintering Applications* (2013). doi:10.5772/53325.

96. Kimura, Y., Wakabayashi, T., Okada, K., Wada, T. & Nishikawa, H. Boron nitride as a lubricant additive. *Wear* 232, 199–206 (1999).

97. Engler, M. & Ruisinger, B. Anwendungen von Metallurgie bis Kosmetik.

25–29 (2016).

98. Lee, G. H. *et al.* Flexible and transparent MoS2 field-effect transistors on hexagonal boron nitride-graphene heterostructures. *ACS Nano* (2013) doi:10.1021/nn402954e.

99. Xu, Z.-Q. *et al.* Single photon emission from plasma treated 2D hexagonal boron nitride. *Nanoscale* 10, 7957–7965 (2018).

100. Choi, S. *et al.* Engineering and Localization of Quantum Emitters in Large Hexagonal Boron Nitride Layers. *ACS Appl. Mater. Interfaces* 8, 29642–29648 (2016).

101. Proscia, N. V. *et al.* Near-deterministic activation of room-temperature quantum emitters in hexagonal boron nitride. *Optica* 5, 1128 (2018).

102. Bourrellier, R. *et al.* Bright UV single photon emission at point defects in h-BN. *Nano Lett.* (2016) doi:10.1021/acs.nanolett.6b01368.

103. Camphausen, R. *et al.* Observation of near-infrared sub-Poissonian photon emission in hexagonal boron nitride at room temperature. *APL Photonics* 5, 1–6 (2020).

104. Chejanovsky, N. *et al.* Structural Attributes and Photodynamics of Visible Spectrum Quantum Emitters in Hexagonal Boron Nitride. *Nano Lett.* (2016) doi:10.1021/acs.nanolett.6b03268.

105. Tawfik, S. A. *et al.* First-principles investigation of quantum emission from hBN defects. *Nanoscale* 9, 13575–13582 (2017).

106. Tran, T. T. *et al.* Resonant Excitation of Quantum Emitters in Hexagonal Boron Nitride. *ACS Photonics* 5, 295–300 (2018).

107. Mendelson, N. *et al.* Identifying Carbon as the Source of Visible Single Photon Emission from Hexagonal Boron Nitride. *arXiv:2003.00949* (2020).

108. Gottscholl, A. *et al.* Initialization and read-out of intrinsic spin defects in a van der Waals crystal at room temperature. *Nat. Mater.* 19, 540–545 (2020).

109. Kianinia, M., White, S., Fröch, J. E., Bradac, C. & Aharonovich, I. Generation of Spin Defects in Hexagonal Boron Nitride. *ACS Photonics* 7, 2147–2152 (2020).

110. Shotan, Z. *et al.* Photoinduced Modification of Single-Photon Emitters in Hexagonal Boron Nitride. *ACS Photonics* 3, 2490–2496 (2016).

111. Jungwirth, N. R. *et al.* Temperature Dependence of Wavelength Selectable Zero-Phonon Emission from Single Defects in Hexagonal Boron Nitride. *Nano Lett.* 16, 6052–6057 (2016).

112. Aharonovich, I. *et al.* Two-level ultrabright single photon emission from diamond nanocrystals. *Nano Lett.* 9, 3191–3195 (2009).

113. Kianinia, M. *et al.* Robust Solid-State Quantum System Operating at 800 K. *ACS Photonics* 4, 768–773 (2017).

114. Exarhos, A. L., Hopper, D. A., Grote, R. R., Alkauskas, A. & Bassett, L. C. Optical Signatures of Quantum Emitters in Suspended Hexagonal Boron Nitride. *ACS Nano* 11, 3328–3336 (2017).

115. Hecht, E. *Optics*. (Addison Wesley, 2002).

116. Novotny, L. & Hecht, B. *Principles of Nano-optics*. (Cambridge University Press, 2006).

117. Corle, T. & Kino, G. *Confocal Scanning Optical Microscopy and Related Imaging Systems*. (1996).

118. Solomon, M. J. & Kogan, M. Confocal Optical Microscopy. *Encycl. Condens. Matter Phys.* 427, 229–235 (2005).

119. Vasista, A. B., Sharma, D. K. & Kumar, G. V. P. Fourier Plane Optical Microscopy and Spectroscopy. *Digit. Encycl. Appl. Phys.* 1–14 (2019) doi:10.1002/3527600434.eap817.

120. Hadfield, R. H. Single-photon detectors for optical quantum information applications. *Nat. Photonics* 3, 696–705 (2009).

121. Becker, W. *Advanced Time-Correlated Single Photon Counting Techniques.* (Springer, 2005).

122. Lounis, B. & Orrit, M. Single-photon sources. *Reports Prog. Phys.* 68, 1129–1179 (2005).

123. Scully, M. & Zubairy, M. S. *Quantum Optics.* (Cambridge University Press, 1997).

124. Beveratos, A., Poizat, J.-P. & Grangier, P. Bunching and antibunching from single NV color centers in diamond. in *Quantum communication, computing, and measurement 3* (ed. Springer) 261–267 (Springer, 2002).

125. Beveratos, A. Handbook of crystal growth. in *Quantum communication, computing, and measurement 3* 261–267 (Springer, 2002).

126. Nguyen, M. *et al.* Effects of microstructure and growth conditions on quantum emitters in gallium nitride. *APL Mater.* 7, (2019).

127. Heikman, S., Keller, S., Mates, T., DenBaars, S. P. & Mishra, U. K. Growth and characteristics of Fe-doped GaN. in *Journal of Crystal Growth* vol. 248 513–517 (2003).

128. Kozodoy, P. *et al.* Heavy doping effects in Mg-doped GaN. *J. Appl. Phys.* 87, 1832–1835 (2000).

129. Masui, H., Nakamura, S., DenBaars, S. P. & Mishra, U. K. Nonpolar and semipolar III-nitride light-emitting diodes: Achievements and challenges. *IEEE Trans. Electron Devices* 57, 88–100 (2010).

130. Li, G. *et al.* GaN-based light-emitting diodes on various substrates: A critical review. *Reports on Progress in Physics* vol. 79 (2016).

131. Stringfellow, G. B. Fundamental Aspects of MOVPE. in *Metalorganic Vapor Phase Epitaxy (MOVPE)* 19–69 (2019). doi:10.1002/9781119313021.ch2.

132. Xin, H. P. & Tu, C. W. GaInNAs/GaAs multiple quantum wells grown by

gas-source molecular beam epitaxy. *Appl. Phys. Lett.* 72, 2442–2444 (1998).

133. Massabuau, F. C. P. *et al.* Morphological, structural, and emission characterization of trench defects in InGaN/GaN quantum well structures. *Appl. Phys. Lett.* 101, (2012).

134. Choi, S. *et al.* Single photon emission from ZnO nanoparticles. *Appl. Phys. Lett.* 104, (2014).

135. Johnston, C. F., Moram, M. A., Kappers, M. J. & Humphreys, C. J. Defect reduction in (11 2- 2) semipolar GaN grown on m -plane sapphire using ScN interlayers. *Appl. Phys. Lett.* 94, 1–4 (2009).

136. Zhu, T. & Oliver, R. A. Unintentional doping in GaN. *Physical Chemistry Chemical Physics* vol. 14 9558–9573 (2012).

137. Jardin, C., Canut, B. & Ramos, S. M. M. The luminescence of sapphire subjected to the irradiation of energetic hydrogen and helium ions. *J. Phys. D. Appl. Phys.* 29, 2066–2070 (1996).

138. Rhode, S. K. *et al.* Mg doping affects dislocation core structures in GaN. *Phys. Rev. Lett.* 111, (2013).

139. Yamamoto, N. *et al.* Cathodoluminescence characterization of dislocations in gallium nitride using a transmission electron microscope. *J. Appl. Phys.* 94, 4315–4319 (2003).

140. Buckley, S., Rivoire, K. & Vučković, J. Engineered quantum dot single-photon sources. *Reports Prog. Phys.* 75, (2012).

141. Acosta, V. M. *et al.* Dynamic stabilization of the optical resonances of single nitrogen-vacancy centers in diamond. *Phys. Rev. Lett.* 108, 6–11 (2012).

142. Brokmann, X., Coolen, L., Dahan, M. & Hermier, J. P. Measurement of the radiative and nonradiative decay rates of single CdSe nanocrystals through a controlled modification of their spontaneous emission. *Phys. Rev. Lett.* 93, 1–4 (2004).

143. Lukosz, W. & Kunz, R. E. Fluorescence Lifetime of Magnetic and Electric Dipoles. *Opt. Commun.* 20, 195–199 (1977).

144. Siampour, H. *et al.* On-chip excitation of single germanium vacancies in nanodiamonds embedded in plasmonic waveguides. *Light Sci. Appl.* 7, (2018).

145. Doherty, M. W. *et al.* The nitrogen-vacancy colour centre in diamond. *Physics Reports* vol. 528 1–45 (2013).

146. Vlasov, I. I. *et al.* Molecular-sized fluorescent nanodiamonds. *Nat. Nanotechnol.* 9, 54–58 (2014).

147. Bradac, C. *et al.* Observation and control of blinking nitrogen-vacancy centres in discrete nanodiamonds. *Nat. Nanotechnol.* 5, 345–349 (2010).

148. Li, L. *et al.* Efficient photon collection from a nitrogen vacancy center in a circular bullseye grating. *Nano Lett.* 15, 1493–1497 (2015).

149. Castelletto, S., Aharonovich, I., Gibson, B. C., Johnson, B. C. & Prawer, S. Imaging and quantum-efficiency measurement of chromium emitters in diamond. *Phys. Rev. Lett.* 105, 2174031–2174034 (2010).

150. Chejanovsky, N. *et al.* Quantum light in curved low dimensional hexagonal boron nitride systems. *arXiv* (2017).

151. Tran, T. T. *et al.* Quantum Emission from Defects in Single-Crystalline Hexagonal Boron Nitride. *Phys. Rev. Appl.* 5, (2016).

152. Choi, S. *et al.* Engineering and Localization of Quantum Emitters in Large Hexagonal Boron Nitride Layers. *ACS Appl. Mater. Interfaces* 8, 29642–29648 (2016).

153. Ziegler, J. *et al.* Single-Photon Emitters in Boron Nitride Nanococoons. *Nano Lett.* 18, 2683–2688 (2018).

154. Abdi, M., Chou, J.-P., Gali, A. & Plenio, M. B. Color Centers in Hexagonal Boron Nitride Monolayers: A Group Theory and Ab Initio Analysis. *ACS*

Photonics (2018) doi:10.1021/acsphotonics.7b01442.

155. Zhang, C. *et al.* Dependence of high density nitrogen-vacancy center ensemble coherence on electron irradiation doses and annealing time. *J. Phys. D. Appl. Phys.* 50, 505104 (2017).

156. Proscia, N. V *et al.* Near-deterministic activation of room temperature quantum emitters in hexagonal boron nitride. *arXiv:1712.01352* (2018).

157. Museur, L., Feldbach, E. & Kanaev, A. Defect-related photoluminescence of hexagonal boron nitride. *Phys. Rev. B* 78, 155204 (2008).

158. Shotan, Z. *et al.* Photoinduced Modification of Single-Photon Emitters in Hexagonal Boron Nitride. *ACS Photonics* 3, 2490–2496 (2016).

159. Exarhos, A. L., Hopper, D. A., Grote, R. R., Alkauskas, A. & Bassett, L. C. Optical Signatures of Quantum Emitters in Suspended Hexagonal Boron Nitride. *ACS Nano* 11, 3328–3336 (2017).

160. Atatüre, M., Englund, D., Vamivakas, N., Lee, S.-Y. & Wrachtrup, J. Material platforms for spin-based photonic quantum technologies. *Nat. Rev. Mater.* (2018) doi:10.1038/s41578-018-0008-9.

161. Takasaki Advanced Radiation Research Institute. https://www.qst.go.jp/site/taka-english/2500.html.

162. Ngoc My Duong, H. *et al.* Effects of High-Energy Electron Irradiation on Quantum Emitters in Hexagonal Boron Nitride. *ACS Appl. Mater. Interfaces* 10, 24886–24891 (2018).

163. Sontheimer, B. *et al.* Photodynamics of quantum emitters in hexagonal boron nitride revealed by low-temperature spectroscopy. *Phys. Rev. B* 96, 121202.

164. Sipahigil, A. *et al.* An integrated diamond nanophotonics platform for quantum-optical networks. *Science (80-.).* 354, 847–850 (2016).

165. Jungwirth, N. R. *et al.* Temperature Dependence of Wavelength Selectable

Zero-Phonon Emission from Single Defects in Hexagonal Boron Nitride. *Nano Lett* 16, 6052–6057 (2016).

166. Benson, O. Assembly of hybrid photonic architectures from nanophotonic constituents. *Nature* 480, 193–199 (2011).

167. Schietinger, S., Barth, M., Aichele, T. & Benson, O. Plasmon-Enhanced Single Photon Emission from a Nanoassembled Metal−Diamond Hybrid Structure at Room Temperature. *Nano Lett.* 9, 1694–1698 (2009).

168. Koenderink, A. F. Single-Photon Nanoantennas. *ACS Photonics* 4, 710–722.

169. Hoang, T. B., Akselrod, G. M. & Mikkelsen, M. H. Ultrafast Room-Temperature Single Photon Emission from Quantum Dots Coupled to Plasmonic Nanocavities. *Nano Lett.* 16, 270–275 (2016).

170. Akselrod, G. M. *et al.* Probing the mechanisms of large Purcell enhancement in plasmonic nanoantennas. *Nat. Photonics* 8, 835–840 (2014).

171. Tam, F., Goodrich, G. P., Johnson, B. R. & Halas, N. J. Plasmonic enhancement of molecular fluorescence. *Nano Lett.* 7, 496–501 (2007).

172. Matsuzaki, K. *et al.* Strong plasmonic enhancement of biexciton emission: controlled coupling of a single quantum dot to a gold nanocone antenna. *Sci. Rep.* 7, 42307 (2014).

173. Andersen, S. K. H., Kumar, S. & Bozhevolnyi, S. I. Coupling of nitrogen-vacancy centers in a nanodiamond to a silver nanocube. *Opt. Mater. Express* 6, 3394 (2016).

174. Choy, J. T. *et al.* Enhanced single-photon emission from a diamond–silver aperture. *Nat. Photonics* 5, 738–743 (2011).

175. Chejanovsky, N. *et al.* Structural Attributes and Photodynamics of Visible Spectrum Quantum Emitters in Hexagonal Boron Nitride. *Nano Lett.* 16, 7037–7045 (2016).

176. Schell, A. W. *et al.* Scanning single quantum emitter fluorescence lifetime imaging: Quantitative analysis of the local density of photonic states. *Nano Lett.* 14, 2623–2627 (2014).

177. Kim, S., Gong, S. H., Cho, J. H. & Cho, Y. H. Unidirectional Emission of a Site-Controlled Single Quantum Dot from a Pyramidal Structure. *Nano Lett.* 16, 6117–6123 (2016).

178. Tran, T. T. *et al.* Deterministic Coupling of Quantum Emitters in 2D Materials to Plasmonic Nanocavity Arrays. *Nano Lett.* 17, 2634–2639 (2017).

179. Wang, D. *et al.* Band-edge engineering for controlled multi-modal nanolasing in plasmonic superlattices. *Nat. Nanotechnol.* advance on, (2017).

180. Huck, A., Kumar, S., Shakoor, A. & Andersen, U. L. Controlled coupling of a single nitrogen-vacancy center to a silver nanowire. *Phys. Rev. Lett.* 106, 096801 (2011).

181. Nguyen, M. *et al.* Nanoassembly of quantum emitters in hexagonal boron nitride and gold nanospheres. *Nanoscale* 10, 2267–2274 (2018).

182. Choy, J. T. *et al.* Spontaneous emission and collection efficiency enhancement of single emitters in diamond via plasmonic cavities and gratings. *Appl. Phys. Lett.* 103, (2013).

183. Kim, S. *et al.* Photonic crystal cavities from hexagonal boron nitride. *Nat. Commun.* 9, 1–8 (2018).

184. Aharonovich, I. & Neu, E. Diamond nanophotonics. *Adv. Opt. Mater.* 2, 911–928 (2014).

185. Hoang, T. B. *et al.* Ultrafast spontaneous emission source using plasmonic nanoantennas. *Nat. Commun.* 6, 7788 (2015).

186. Khramtsov, I. A. & Fedyanin, D. Y. Bright single-photon emitting diodes

based on the silicon-vacancy center in ALN/diamond heterostructures. *Nanomaterials* 10, (2020).

187. Berhane, A. M. *et al.* Bright Room-Temperature Single-Photon Emission from Defects in Gallium Nitride. *Adv. Mater.* 29, 1605092.

188. Ansaloni, L. M. S. & de Sousa, E. M. B. Boron Nitride Nanostructured: Synthesis, Characterization and Potential Use in Cosmetics. *Mater. Sci. Appl.* (2013) doi:10.4236/msa.2013.41004.

189. Li, N., Zhao, P. & Astruc, D. Anisotropic gold nanoparticles: Synthesis, properties, applications, and toxicity. *Angewandte Chemie - International Edition* vol. 53 1756–1789 (2014).

190. Ehrentraut, D. & Fukuda, T. Ammonothermal crystal growth of gallium nitride A brief discussion of critical issues. in *Journal of Crystal Growth* (2010). doi:10.1016/j.jcrysgro.2010.04.004.

191. Andersen, S. K. H. *et al.* Hybrid Plasmonic Bullseye Antennas for Efficient Photon Collection. *ACS Photonics* 5, 692–698 (2018).

192. P. B. Johnson and R. W. Christy. Optical Constant of the Nobel Metals. *Phys. Rev. B* 6, 4370–4379 (1972).

193. Curto, A. G. *et al.* Unidirectional Emission of a Quantum Dot Coupled to a Nanoantenna. *Science (80-.).* 329, 930–933 (2010).

194. Butun, S., Tongay, S. & Aydin, K. Enhanced Light Emission from Large-Area Monolayer MoS2 Using Plasmonic Nanodisc Arrays. *Nano Lett.* 15, 2700–2704 (2015).

195. Cai, T. *et al.* Coupling emission from single localized defects in 2D semiconductor to surface plasmon polaritons. *arXiv.*

196. Hayee, F. *et al.* Revealing multiple classes of stable quantum emitters in hexagonal boron nitride with correlated optical and electron microscopy. *Nat. Mater.* 19, 534–539 (2020).

197. Duong, N. M. H. *et al.* Facile Production of Hexagonal Boron Nitride Nanoparticles by Cryogenic Exfoliation. *Nano Lett.* 19, 5417–5422 (2019).

198. Mendelson, N. *et al.* Grain Dependent Growth of Bright Quantum Emitters in Hexagonal Boron Nitride. *arXiv:2005.10699* 1–10 (2007).

199. Dietrich, A. *et al.* Observation of Fourier transform limited lines in hexagonal boron nitride. *Phys. Rev. B* 98, 2–6 (2018).

200. Kianinia, M. *et al.* All-optical control and super-resolution imaging of quantum emitters in layered materials. *Nat. Commun.* 9, (2018).

201. Kim, S. *et al.* Integrated on Chip Platform with Quantum Emitters in Layered Materials. *Adv. Opt. Mater.* 7, 1–6 (2019).

202. Beveratos, A. *et al.* Room temperature stable single-photon source. *Eur. Phys. J. D* 18, 191–196 (2002).